A CLUSTER STUDY OF THE NUCLEI ^{212}Po AND ^{218}Rn

IBRAHIM Taofiq Toyin

Dissertation presented for the Degree of Doctor of Philosophy

at the Stellenbosch University

Supervisor: Dr S. M. Wyngaardt

Co-Supervisor: Professor S. M. Perez

December 2009

Declaration

By submitting this dissertation electronically, I declare that the entirety of the work contained therein is my own, original work, that I am the owner of the copyright thereof (unless to the extent explicitly otherwise stated) and that I have not previously in its entirety or in part submitted it for obtaining any qualification

.....
Date

Abstract

A binary cluster model is used to investigate the properties of the ground state band of ^{212}Po, modelled as a ^{208}Pb-alpha core-cluster system. The results obtained using a microscopic core-cluster potential are compared to those obtained with a purely phenomenological potential. The two potentials were found to exhibit similar surface behaviour and thus give similar predictions for the ground state alpha decay half-life. They however generate very different energy spectra, with the results from the phenomenological potential clearly superior. We optimize the phenomenological potential parameters, and propose an additional short range interaction to improve the underbinding generally found for the $J^\pi = 0^+$ ground state. We then investigate two possible scenarios for generating the negative parity states in ^{212}Po. We find that both are necessary in order to produce low-lying negative parity states which are able to decay via electric dipole transitions to the positive parity states of the ground state band. Finally we present a novel calculation of the properties of the low-lying positive and negative parity states of ^{218}Rn described as a doubly closed ^{208}Pb core plus a ^{10}Be cluster.

Samevatting

'n Binêre bondel model word gebruik om die eienskappe van die grondtoestands energie band van ^{212}Po, te modeleer as 'n ^{208}Pb-alpha kern-bondel sisteem te ondersoek. Die resultate verkry vanaf 'n mikroskopiese kern-bondel potentiaal word vergelyk met die wat verkry is met 'n suiwer fenomenologiese potentiaal. Die twee potentiale is verkry om dieselfde oppervlakte toestande voor te stel en gee sodoende dieselfde voorspellings vir die grondtoestand alpha verval halfleeftyd. Alhoewel dit baie verskillende energie spektra genereer, toon die resultate van die fenomenologiese potentiaal dat dit duidelik beter is. Ons optimiseer hierdie fenomenologiese parameters en stel 'n addisionele kort ry-afstands interaksie voor om die algemene ondergebondenheid wat oor die algemeen by die $J^{\pi} = 0^{+}$ grondtoestand voorkom, te verbeter. Ons ondersoek ook hierdie twee moontlike scenarios om die negatiewe pariteitstoestande in ^{212}Po te genereer. Ons vind dat beide scenarios noodsaaklik is om laagliggende pariteitstoestande te produseer, sodat verval deur elektriese dipool oorgange na die positiewe pariteitstoestande van die grondtoestandsband moontlik is. Laagliggende positiewe en negatiewe pariteitstoestande, van die ^{218}Rn wat beskryf word as 'n dubbelgeslote ^{208}Pb kern en 'n ^{10}Be bondel.

Acknowledgements

This study would not have been possible if not for the support of many good people. First and foremost my sincere gratitude goes to my supervisor Dr Shaun M. Wyngaardt for his unwavering support and for all the indispensable discussions. I am also grateful to Professor S. M. Perez for his readiness to co-supervise my work and for providing me with invaluable guidance and suggestions.

My heartfelt thanks to Dr Z. Z. Vilakazi who is instrumental to my studentship at the University of Cape Town but could not continue with the academic supervision due to the greater call to serve the Nation and the South African Nuclear Physics Community in particular. I am also grateful for his help to secure the much needed fund and for his constant interest in my research.

I want to express my gratitude to Dr R. Bark for accepting to be my co-supervisor when our idea was to extend the existing data on the Polonium isotope and for the guidance provided on the practical aspect of the Experimental Nuclear Physics which has helped broaden my horizon. The innumerable and illuminating discussions I had with him have also helped me to reason beyond this study.

I gratefully acknowledge the support of the iThemba LABS and all members of the Nuclear Physics group. Particularly, I would like to thank Drs J. J. Lawrie and R. T. Newman for their effort to ensure my financial stability and for giving due attention to our proposed experiment on the Polonium isotope.

It is my pleasure to acknowledge the effort of Miss Allison Hoffmann who painstakingly translate the abstract to Afrikaans without which the thesis will remain incomplete.

I thank the Physics Department of the University of Cape Town where I started the Doctorate programme for their support, most especially Prof. D. G. Aschman, Prof. R. W. Fearick, Drs R. Nchodu, M. Azwinndini, Miss Lesley Jennings and my colleagues. I hereby mention my sincere gratitude to Abdulrafiu Raji, Biliamin Oborien, Rabiu Ademola, Dr Sherrif Salisu, Dr Odo Ayodele and their respective families for been there for me and my family. May Allah Subhana Wata'ala reward you all. Without you life might have been difficult for us in Cape Town.

I really appreciate the support provided by the Physics Department, Stellenbosch University for the smooth transfer of my programme and in particular the warm welcome I received from Prof. F. G. Scholtz, Prof. G. Hillhouse, Dr B. Van der Ventel, Mrs A. Lackey, Me C. Ruperti, Mr F. Timmey, Mr S. February, Me H. Randall and Mr Ulli Deuschland who helped me with a very good bicycle which keeps me fit and mobile. Many thanks to my colleagues in the Physics Department and all members of Nigerian Student Association of Stellenbosch University (ANSSU) for their support.

Without the financial support of the National Research Foundation of South Africa (NRF), the iThemba LABS, the National Institute of Theoretical Physics (NiTheP) and the German Deutscher Akademischer Austauschdienst (DAAD) this work would not have been possible. I would forever be grateful for all their financial support.

Many thanks to the Physics Department, University of Ilorin for giving me the opportunity to seek for more knowledge outside the Department. I am particularly grateful to Dr K. J. Oyewumi and his family for their continued support.

I especially thank all my friends Noah Rasaq, Basheer Kuranga, Musbau Aileru and his family, Musa Usman, Imran Saka, Afolabi Hammeed, Arazeem A. Ali, Suleiman Garba, Sunday Adebayo, Femi and Dotun Abioye, Aina Bola, Azeez Adams, and my elder brothers Fatai Onikoko (aka Baba Ayo), Garba Salman, Drs Ajao Moyosore and Saka Ambali for their moral support and concern for my progress.

Thanks to Murtala, Abdul-Azeez Kehinde, Kadry, Salamat Bolanle Abdulrasaq, Rukkayat, Suliat for holding the fort in my absence. I really appreciate all your support and concerns.

I am greatly indebted to my uncle and his family, and my parents Alhaji and Alhaja S. A. Ibrahim, for their constant love and support over the years.

Finally I would like to express my sincere thanks to my wife Fatimah Oluwabukola for her continuous support, love and encouragement, and my children, Hawwa Atinuke Oluwakemi and Sheik Ahmad Olaitan, for their patience in the difficult times.

Dedicated to my family

Contents

List of Tables

List of Figures

Chapter 1

Introduction

1.1 Clustering In Nuclei

A fundamental aim of research in the physical sciences is to describe the observed properties of a system in terms of the microscopic motion of its constituent particles. For a nucleus consisting of the order of a hundred nucleons interacting through complex nuclear forces such a programme is too ambitious necessitating a simplified description in terms of nuclear models. In the independent particle model, for example, nucleons are taken to move independent of each other in a common binding potential. This simple model has been found to reproduce some properties of the nucleus such as the enhanced stability associated with proton and/or neutron magic numbers, and the angular momenta and magnetic dipole moments (the Schmidt lines) of the ground states of doubly magic nuclei plus or minus one nucleon. Away from closed shells, however, the properties of nuclei are better described in the standard shell model where the correlations in the nucleon motion are recovered by introducing the nucleon-nucleon (NN) interactions as in the work of Brown and Wildenthal on sd-shell nuclei [1]. Other models such as the vibrational and rotational models build in the nucleon correlations at the outset with the nucleons moving collectively as part of a nuclear fluid [2]. In these models the nuclear shape oscillations about a spherical mean, as well as the rotational motion of a permanently deformed nucleus, have been used to gain an understanding of nuclear properties such as the harmonic spectra of vibrational nuclei, and the characteristic $J(J+1)$ spectra and enhanced quadrupole transition strengths of the ground state bands of deformed even-even nuclei. These collective behaviours of the nucleus can be regarded as the result of correlations involving a large number of nucleon degrees of freedom.

In its simplest form a cluster model describes the nucleus as a binary system in which the energetically favoured correlated nucleon motions result in a cluster made up of a few nucleons orbiting a core containing the remaining nucleons [3, 4]. Such a model has been employed by

several investigators to successfully describe the structure of light nuclei [5, 6, 7]. We note that the cluster model mimics some of the properties of the other models described above, depending on the size of the assumed cluster. For instance, the independent particle model is recovered in the extreme case where the cluster is taken to be a single nucleon, whereas for larger clusters the cluster nucleons clearly move collectively.

The above discussions illustrate how correlated nucleon motion plays a pivotal role in the structure and dynamics of a nucleus. Among the possible nucleon correlations two and four-body correlations [3] have been identified as the most important ones.

The two-body correlation is especially important in the development of the independent pair approximation to nuclear many body problem [8]. Pairing correlations involving identical nucleons have been found useful for classifying many-nucleon states of semi-magic nuclei in the shell model [9, 10], and is also fundamental to the application of Bardeen-Cooper-Schriffer (BCS) theory of superconductivity to nuclear physics [3, 11]. The role of neutron-proton pair correlation, on the other hand, is particularly important in the deuteron transfer reaction and the structure of odd-odd nuclei [3]. Experimental techniques for investigating these correlations include the variation of two nucleon separation energy with respect to the neutron number in the tin isotopes, and two neutron transfer reaction cross section [11].

The investigation of correlations involving a number of nucleons greater than two is a natural development and the alpha particle, with spin-parity $J^{\pi} = 0^{+}$ and strong binding energy, plays a central role in this development. This supposes that the four body correlations involving two protons and two neutrons may be sufficiently strong as to form a stable or localized substructure with the same quantum numbers as the free alpha particle [3]. Experimentally, the existence of alpha clustering, especially in light nuclei, is well established by the strong selective excitations in alpha transfer reactions, rotationally spaced energy levels, enhanced electromagnetic moments and transition strengths, and appreciable alpha widths for resonant states above threshold [12]. These observations indicate that the cluster hypothesis is not just some theoretical construct without physical significance, and the microscopic approaches such as the Wheelers resonating group method, the generator coordinate method [13], the Harvey double centre oscillator model, and the Bloch-Brink cluster model are a few of the methods employed to investigate clustering in light nuclei [7].

The hypothesis of spatially localized substructures in the nuclear medium can also be used to address the alpha and exotic decay of heavy nuclei [14, 15]. This follows from the fact that a nuclear state which decays primarily into two composite particles has a natural description as a two-cluster configuration involving these particles, with the actual details being determined

by the internal composition and interaction of the two clusters [14, 16]. Alpha decay, and the description of a nucleus as an alpha-daughter system, has been a subject of research since the earliest studies in Nuclear Physics. The quantum mechanical description of alpha decay formulated by Gamow, and independently by Condon and Gurney [17], requires an accurate knowledge of the preformation probability of the alpha-daughter system as well as the alpha-daughter interaction (which generates the corresponding Coulomb barrier). These remain important problems in the description of the dynamics of a decaying system.

An early microscopic study of the alpha decay process by Thomas employed the R-matrix theory [18]. This was further extended by Mang [17] who included refined shell model wavefunctions to obtain results essentially similar to the Gamow formulation but with the preformation amplitude obtained microscopically. The decay width was defined as [17];

$$\Gamma = \sum_{jl} P_l(\varepsilon)\gamma^2_{Jjl} \tag{1.1}$$

$$\gamma^2_{Jjl} = \frac{\hbar^2 R}{2M}|g^J_{jl}(R)|^2 \tag{1.2}$$

where

- $P_l(\varepsilon)$ represents the energy dependent decay penetrability,
- γ_{Jjl} is the reduced width,
- J and j are the angular momenta of the parent and daughter nuclei,
- l is the angular momentum of the alpha relative to the daughter nucleus,
- M is the reduced mass,
- R is the relative distance between the alpha particle and the daughter nucleus,
- $g(R)$ is the formation probability defined as the overlap of the initial parent state and the antisymmetrized product of the final states.

The success of any microscopic description depends largely on the exact knowledge of the factor $g(R)$ [17]. Shell model calculations of the factor have shown the need to properly account for Pauli effects, and for the inclusion of configuration mixing to induce the clustering of two protons and two neutrons to form an alpha cluster at the nuclear surface [19, 20].

A more recent approach which combines both shell and alpha cluster configurations [21] results in an enhanced amount of alpha-daughter preformation in ^{212}Po, with the preformation

probability placed at ~ 0.025 [22] compared to the previous shell model prediction of $\sim 10^{-5}$ [17, 22]. An analysis using a folding potential model for the alpha-daughter interaction has placed the alpha-daughter preformation probability in the same nucleus at ~ 0.035 [23, 24]. In their microscopic approach, Delion *et al.* [25] used a realistic single particle basis within the BCS formalism to obtain the nuclear wavefunctions and hence the preformation amplitude. The latter was then used to obtain the alpha decay widths for a number of nuclei in good agreement with experimental results. In the phenomenological binary cluster model of Buck, Merchant and Perez (BMP) the preformation probability is usually taken to be of the order of unity [26], and a comparison of the model results with experiment shows a relatively small variation of the probability from one nucleus to another [12]. These widely differing values of the alpha-daughter preformation probability are a reflection of our poor understanding of this important quantity, which therefore remains an issue to be addressed more properly. In a related topic, Blendowske and Walliser [27] describe the dependence of the preformation probability of an exotic cluster on its mass and the (poorly understood) preformation factor of the alpha particle.

The form of the alpha-nucleus interaction potential on the other hand is also a fundamental issue that has not been conclusively resolved and a number of phenomenological models obtained from fits to experimental data has been found useful over years [12, 21].

A simple approximation to the nuclear potential is the square well potential. An early analysis [28] of the nucleon motion in medium and heavy nuclei, for example, suggests a finite square well potential rather than the average single particle oscillator potential commonly employed in light nuclei. Although not physically realistic [26], a semiclassical cluster model study of alpha decay using a square well as the local core-cluster interaction gave results which agreed with the Geiger-Nuttal law [29]. The agreement was achieved by using a fixed depth for the square well potential and a radius fitted to the individual decay energy. Further studies with a potential of Cosh geometry, considered to approximate a realistic potential more accurately, was also found to have good predictive power for the alpha decay phenomenon [26, 30]. This potential is given by

$$V(r) = \frac{-V_o\left[1 + \cosh\left(\frac{R}{a}\right)\right]}{\cosh\left(\frac{r}{a}\right) + \cosh\left(\frac{R}{a}\right)} \tag{1.3}$$

where V_o, R and a are the potential depth, nuclear radius and the diffuseness respectively. The radial distance r is the core-cluster separation distance. The depth and diffuseness were held constant and the radius R was again fitted to the alpha decay energy. It was however realized that the Cosh potential, using parameter values which reproduced the alpha decays of heavy nuclei, gave poor results for the level structures of the alpha plus closed core nuclei like ^{20}Ne, ^{44}Ti, and ^{212}Po [26].

Recently a phenomenological potential model which consistently reproduces the alpha and exotic decay half-lives and the level properties of nuclei in the rare earth and the actinide region is of the form

$$V(r) = -V_o \left[\frac{x}{1 + \exp\left(\frac{r-R}{a}\right)} + \frac{1-x}{\left[1 + \exp\left(\frac{r-R}{3a}\right)\right]^3} \right] \tag{1.4}$$

where x is a mixing parameter and the remaining parameters retain the same definition as in Eqn (1.3). This interaction is of particular interest in this study with special attention on the alpha plus doubly closed ^{208}Pb core.

The binary cluster model with these phenomenological potentials does not only give results in good agreement with the measured alpha decay half-lives of heavy nuclei but also provides us with some insight into the systematics of the alpha decay phenomenon [31]. Examples of the characteristic effects inferred by BMP include higher preformation probability of alpha clustering in the even-even nuclei compare to the odd-even nuclei, and a stronger effect of the neutron shell closures, which necessitate a change of global quantum number $\Delta G = 2$ at these closures, when compared to the proton shell closures.

On a more microscopic basis the core-cluster interaction may be constructed from a nucleon-nucleon interaction. Prior to the development of the Saxon-Wood plus Saxon-Wood cubed (SW+SW^3) potential form of Eqn (1.4) such a microscopic interaction had been employed in various forms to describe bound cluster states in light nuclei [6] and the exotic decays in heavy nuclei [30]. Recently the microscopic double folding potential model has been extended to describe the alpha decay half-lives and the structure of heavy nuclei [23, 32, 33]. An application of the interaction to ^{94}Mo and ^{212}Po in particular suggests a good amount of alpha clustering in these nuclei [34]. In these studies, however, the normalization factor of the microscopically derived potential and hence the effective potential strength were arbitrarily adjusted to reproduce the experimental results.

Alpha transfer reactions, in addition to the alpha decay phenomenon, has been shown to provide further experimental evidence for the existence of preformed alpha cluster structure. However there is a number of experimental observations showing the possiblity of having other cluster structures in the same nucleus. These include light cluster transfer and/or knock-out reactions involving deuteron ^{2}H, triton ^{3}H and helium ^{3}He [35], exotic decays of heavy nuclei which involves the emission of neutron rich clusters heavier than the alpha particle [36, 37, 38], and heavy cluster structure such as the $^{12}\mathrm{C} - ^{12}\mathrm{C}$ cluster structure observed in resonance studies of ^{24}Mg [7, 39].

Thus, there is the possibility of competing cluster structures in a given nucleus. For example ^{212}Po has a ground state band which can be described by ^{208}Pb-^{4}He model, but it may also sustain an excited superdeformed band corresponding to a much heavier cluster such as ^{80}Ge, and a correspondingly lighter closed-shell core ^{132}Te [40, 41].

In order to account for a particular configuration the cluster model assumes that the most probable core-cluster combination depends on such factors as the core-cluster interaction and the stability of the nuclei involved [28, 42]. We note therefore that, although other forms of cluster configurations may exist, alpha clustering seems to be the most probable out of a number of possible transient structures formed by the correlated motions of the underlying valence nucleons [26]. In the case of mid-shell nuclei, however, a mixture of the various core-cluster systems have been successfully used to describe these nuclei in a systematic application of the binary cluster model [43].

Using the experimentally observed exotic decays the energy levels and the electromagnetic properties of the positive parity ground state band of a number of heavy trans-lead nuclei have been studied extensively within the binary cluster model [37]. These studies have recently been extended to describe the negative parity bands of these actinide nuclei by coupling the relative motion of the core-cluster system to an excited core nucleus [44] .

Other notable works relevant to this study include the work done by [45] in which the alpha and heavy cluster decay rates have been used to study the structure of unstable nuclei through a combination of the advantages of the superfluid model for nucleon clustering and the classical model of resonance tunneling in many-particle systems. A similar study based on the unitary correlation model of Villars, which addresses the three body problem, has also been used to investigate the structure and transitions of the ground state of some exotic nuclei [46]. A technique employing Antisymmetrized Molecular Dynamics (AMD) has also been used extensively to study the cluster formation and the structure of exotic nuclei [47].

More complex structures comprising three or more clusters have also been proposed as an extension of the cluster model to three alpha systems and/or two alpha plus a core nucleus. For some even-even medium mass nuclei, this approach has been shown to enjoy a similar success as in the other cluster models [48].

1.2 Aim of the Study

The above review is by no means exhaustive given the volume of work on alpha and exotic decay, and on clustering phenomena. The various models which address the nucleon correlation effects and their varying degree of success have been discussed in the Introduction. An important ingredient of these models is the choice of the interaction between the relevant degrees of freedom. In this thesis we focus on the binary cluster model. We consider a microscopic and a phenomenological potential form of the core-cluster interaction and discuss their relative merits with special reference to the alpha decay and positive parity level structure of ^{212}Po.

A further aim is to investigate the possibility of core excitation and to extend recent works on negative parity states in trans-lead nuclei to this nucleus.

Finally we aim to carry out a novel analysis of the positive and negative parity states of ^{218}Rn, and to determine an optimum potential suitable for a simultaneous description of the decay properties and of the band structures of both ^{212}Po and ^{218}Rn.

1.3 Motivation

Because of the relatively high binding energy of the components, nuclei which can be partitioned into a doubly-closed alpha particle plus a doubly-closed core are of particular interest from a binary cluster model point of view. ^{212}Po is one such nucleus, but differs markedly from the others (e.g. ^{20}Ne and ^{44}Ti) in the level structure and decay properties of its ground state band. It is important therefore to examine whether it can be described in a similar manner to its lighter counterparts by finding, for example, a common potential prescription for all these nuclei.

It is also important to extend recent works [44] on negative parity bands in ^{238}U to lighter trans-lead nuclei such as ^{212}Po and to predict the properties of the negative parity bands in these nuclei.

1.4 Plan of the Thesis

We present the general formalism of the microscopic M3Y potential and discuss its suitability as an interaction potential for the cluster model in chapter two. The phenomenological binary cluster model and the theoretical formalism necessary to compare the model predictions with observations are discussed in chapter three. We present our results on ^{212}Po in chapter four. Low-lying negative parity bands of ^{212}Po are discussed in chapter five with emphasis on the possibility of band mixing. Model calculations for ^{218}Rn are presented in chapter six and our conclusions

follow in chapter seven. The Appendix contains details of the formalism and numerical methods of interest which are best separated from the main text.

Chapter 2

Microscopic Potential

2.1 Introduction

In chapter 1 we allude to the difficulties associated with a complete microscopic description of the structure of heavy nuclei. The core-cluster model which provides an appealing simplification is however dependent on the choice of core-cluster potential. It is therefore desirable to relate the core-cluster interaction potential to the fundamental nucleon-nucleon (NN) interaction in such a way that the many-body effects are systematically incorporated. The resulting microscopic potential model is then expected to provide a more satisfactory and unified understanding of the nucleus-nucleus interactions.

A simple procedure to obtain such a microscopic core-cluster potential is to identify the empirical local potential of the binary cluster model with the real part of the microscopic optical potential [49] for heavy-ion collisions. Such an identification has been shown to be physically acceptable provided the relevant parameters are defined appropriately [34].

The microscopic heavy-ion scattering potential of interest is the double folding potential in which an effective NN interaction is folded over matter densities of the interacting nuclei. The potential is especially successful in describing heavy-ion scattering data and it has generally been found to give a physically motivated and unified description of processes involving composite systems [50].

The solution of the relative motion Schrödinger Wave Equation (SWE) with the microscopic core-cluster interaction is expected to be tractable. The energy structure and other physical properties of a nucleus can then be specified from the solution of the SWE.

Thus the mathematical difficulties associated with a complete microscopic solution would be removed with the final results being more realistic than those obtained with a pure phenomenological potential.

2.2 Nucleon-Nucleon Interaction

The NN interaction derived from fits to NN experimental data, and from properties of the deuteron is generally taken to be of the form[1] [9];

$$\begin{aligned} V(r;\boldsymbol{\sigma_1};\boldsymbol{\sigma_2};\boldsymbol{\tau_1};\boldsymbol{\tau_2}) = V_o(r) + V_\sigma(r)\boldsymbol{\sigma_1}\cdot\boldsymbol{\sigma_2} + V_\tau(r)\boldsymbol{\tau_1}\cdot\boldsymbol{\tau_2} + V_{\sigma\tau}(r)(\boldsymbol{\sigma_1}\cdot\boldsymbol{\sigma_2})(\boldsymbol{\tau_1}\cdot\boldsymbol{\tau_2}) \\ + V_{LS}(r)\boldsymbol{L}\cdot\boldsymbol{S} + V_{LS\tau}(r)(\boldsymbol{L}\cdot\boldsymbol{S})(\boldsymbol{\tau_1}\cdot\boldsymbol{\tau_2}) + V_T(r)\hat{S}_{12} \\ + V_{T\tau}(r)\hat{S}_{12}(\boldsymbol{\tau_1}\cdot\boldsymbol{\tau_2}) + V_Q(r)\hat{Q}_{12} + V_{Q\tau}(r)\hat{Q}_{12}(\boldsymbol{\tau_1}\cdot\boldsymbol{\tau_2}) \end{aligned} \tag{2.1}$$

where $\boldsymbol{\sigma}$ and $\boldsymbol{\tau}$ are the Pauli spin and isospin matrices, $\boldsymbol{L}$ and $\boldsymbol{S}$ the orbital and spin angular momentum, and T denotes a tensor component respectively.

The central part of the NN potential of Eqn (2.1) includes the radial ($V_o(r)$), spin dependent ($V_\sigma(r)\boldsymbol{\sigma_1}\cdot\boldsymbol{\sigma_2}$), isospin dependent ($V_\tau(r)\boldsymbol{\tau_1}\cdot\boldsymbol{\tau_2}$) and spin-isospin ($V_{\sigma\tau}(r)(\boldsymbol{\sigma_1}\cdot\boldsymbol{\sigma_2})(\boldsymbol{\tau_1}\cdot\boldsymbol{\tau_2})$) dependent components respectively. The non-central components are the spin-orbit terms ($V_{LS}(r)\boldsymbol{L}\cdot\boldsymbol{S}$) and ($V_{LS\tau}(r)(\boldsymbol{L}\cdot\boldsymbol{S})(\boldsymbol{\tau_1}\cdot\boldsymbol{\tau_2})$), and the tensor components given by ($V_T(r)\hat{S}_{12}$) and ($V_{T\tau}(r)\hat{S}_{12}(\boldsymbol{\tau_1}\cdot\boldsymbol{\tau_2})$) respectively. The quadratic spin-orbit components ($V_Q(r)\hat{Q}_{12}$) and ($V_{Q\tau}(r)\hat{Q}_{12}(\boldsymbol{\tau_1}\cdot\boldsymbol{\tau_2})$) give a further momentum dependence of the potential. The tensor ($\hat{S}_{12}$) and the quadratic spin-orbit ($\hat{Q}_{12}$) operators are defined as

$$\hat{S}_{12} = \frac{3}{r^2}(\boldsymbol{\sigma_1}\cdot\boldsymbol{r})(\boldsymbol{\sigma_2}\cdot\boldsymbol{r}) - \boldsymbol{\sigma_1}\cdot\boldsymbol{\sigma_2} \tag{2.2}$$

and

$$\hat{Q}_{12} = \frac{1}{2}\Big[(\boldsymbol{\sigma_1}\cdot\boldsymbol{L})(\boldsymbol{\sigma_2}\cdot\boldsymbol{L}) + (\boldsymbol{\sigma_2}\cdot\boldsymbol{L})(\boldsymbol{\sigma_1}\cdot\boldsymbol{L})\Big]. \tag{2.3}$$

The unknown radial dependence of the components may be obtained, in principle, from Quantum Chromodynamics (QCD). They are usually expressed in terms of Yukawa potentials or some other functional fits to experimental data. Thus the available NN potentials are phenomenological in nature and a complete microscopic NN potential derived from QCD is yet to be achieved.

The NN force may simply be divided into the strongly repulsive short range ($r < 1$ fm), the attractive intermediate range ($1 < r < 2$ fm), and the long range ($r > 2$ fm) components as in Figure (2.1). The short range is believed to be mediated by QCD effects, multi-pion and heavy meson exchanges. The intermediate range involves two pions and heavy meson exchanges, and the long range part is described by one-pion exchange. Common examples of the NN potential include Hamada-Johnston, Reid hard and soft core, Sprung-de Tourreils supersoft potentials etc.

[1] Bold symbols have been used to represent vectors throughout i.e. $\boldsymbol{r} = r\hat{r}$

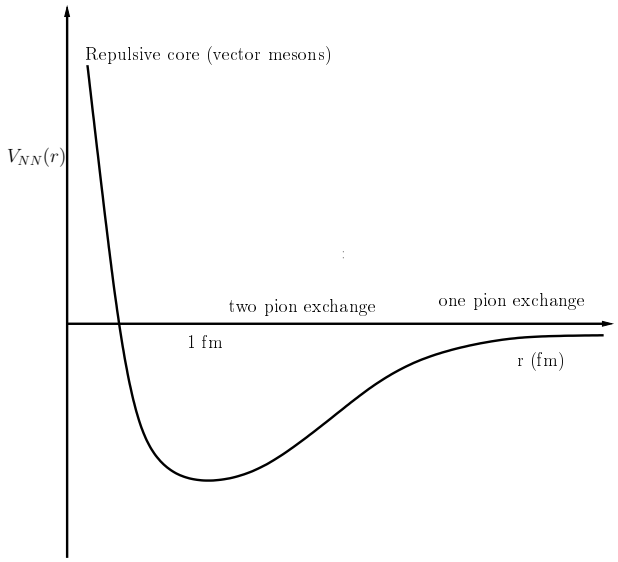

Figure 2.1: A schematic representation of the Nucleon-Nucleon interaction [51].

There are also the non-local formalisms which include Yamaguchi-Tabakin-Mongan, Kuo-Brown, Green potentials [2, 52] etc. Each of these potentials is found, however, to satisfy specific NN properties.

2.3 The Double-Folding Model: M3Y Interaction

The double folding nucleus-nucleus interaction potential is defined as an averaged NN interaction folded over matter distributions of the two nuclei in much the same way as the Coulomb potential between two charge distributions is obtained by averaging the point charge interactions over the charge distributions [53].

Consider the bound core-cluster system as a projectile-target system in their ground states such that the system is described by the SWE of the form

$$[\hat{H} - E]\Psi = 0 \tag{2.4}$$

where the operator $\hat{H}$ represents the total Hamiltonian of the system defined as[2]

$$\hat{H}(\boldsymbol{r}; \boldsymbol{r}_1 \cdots \boldsymbol{r}_A; \boldsymbol{r}'_1 \cdots \boldsymbol{r}'_B) = \hat{H}_A(\boldsymbol{r}_1 \cdots \boldsymbol{r}_A) + \hat{H}_B(\boldsymbol{r}'_1 \cdots \boldsymbol{r}'_B) + \hat{T}_o + \sum_{ij} v(\boldsymbol{r}_{ij}) \tag{2.5}$$

where the operators $\hat{H}_A$ and $\hat{H}_B$ are the intrinsic Hamiltonians of the target and the projectile, $\hat{T}_o$ is the relative kinetic energy of the projectile with respect to the target, and the interaction

[2]We have suppressed the spin and isospin coordinates.

potential between the projectile and target nucleons i and j is given by $v(\boldsymbol{r}_{ij})$.
Supposing the antisymmetrized orthonormal and complete solutions of $\hat{H}_A$ and $\hat{H}_B$ are given by,

$$\begin{aligned}\hat{H}_A(\boldsymbol{r}_1\cdots\boldsymbol{r}_A)\psi_{A\alpha}(\boldsymbol{r}_1\cdots\boldsymbol{r}_A) &= \varepsilon_\alpha\psi_{A\alpha}(\boldsymbol{r}_1\cdots\boldsymbol{r}_A)\\ \hat{H}_B(\boldsymbol{r}'_1\cdots\boldsymbol{r}'_B)\psi_{B\beta}(\boldsymbol{r}'_1\cdots\boldsymbol{r}'_B) &= \varepsilon_\beta\psi_{B\beta}(\boldsymbol{r}'_1\cdots\boldsymbol{r}'_B)\end{aligned} \tag{2.6}$$

where ε_α and ε_β are the eigenenergies of the states $\psi_{A\alpha}$ and $\psi_{B\beta}$ respectively. Ignoring the antisymmetrization effect for the moment in the $A+B$ system we may expand the wavefunction Ψ in terms of the internal eigenstates of the composite nuclei [53];

$$\Psi(\boldsymbol{r};\boldsymbol{r}_1\cdots\boldsymbol{r}_A;\boldsymbol{r}'_1\cdots\boldsymbol{r}'_B) = \sum_{\alpha\beta}\psi_{A\alpha}(\boldsymbol{r}_1\cdots\boldsymbol{r}_A)\psi_{B\beta}(\boldsymbol{r}'_1\cdots\boldsymbol{r}'_B)\chi_{\alpha\beta}(\boldsymbol{r}) \tag{2.7}$$

where $\chi_{\alpha\beta}(\boldsymbol{r})$ is the relative motion wavefunction of the systems each with internal states α and β, and $\boldsymbol{r}$ is the relative coordinate between their centres of mass. The elastic channel with $\alpha=\beta=0$, corresponds to a situation of spinless core and cluster. Using the Feschbach formalism with a ground state projection operator $\hat{P}$ given by,

$$\hat{P} = |\psi_{A0}\psi_{B0}\rangle\langle\psi_{A0}\psi_{B0}| \tag{2.8}$$

and its complement $\hat{Q} = 1-\hat{P}$. The eigenvalue problem of Eqn (2.4) reduces to [9, 54];

$$\Big[E-\hat{P}\hat{H}\hat{P}-\hat{P}\hat{H}\hat{Q}\frac{1}{E-\hat{Q}\hat{H}\hat{Q}}\hat{Q}\hat{H}\hat{P}\Big]\hat{P}\Psi = 0. \tag{2.9}$$

Multiplying Eqn (2.9) from the left by $\langle\psi_{A0}\psi_{B0}|$ followed by an integration over the coordinates of the nucleons in A and B we have

$$\Big[E-\langle\psi_{A0}\psi_{B0}|\hat{H}|\psi_{A0}\psi_{B0}\rangle-\langle\psi_{A0}\psi_{B0}|\hat{H}\hat{Q}\frac{1}{E-\hat{Q}\hat{H}\hat{Q}}\hat{Q}\hat{H}|\psi_{A0}\psi_{B0}\rangle\Big]\chi_{00} = 0, \tag{2.10}$$

where χ_{00} is now the relative motion wavefunction with both nuclei in their respective ground states $\alpha=0$ and $\beta=0$. Using the ground state $\varepsilon_0=0$ we have [9];

$$\begin{aligned}\hat{H}_A(\boldsymbol{r}_1\cdots\boldsymbol{r}_A)\psi_{A0}(\boldsymbol{r}_1\cdots\boldsymbol{r}_A) &= \varepsilon_0\psi_{A0}(\boldsymbol{r}_1\cdots\boldsymbol{r}_A) = 0\\ \hat{H}_B(\boldsymbol{r}'_1\cdots\boldsymbol{r}'_B)\psi_{B0}(\boldsymbol{r}'_1\cdots\boldsymbol{r}'_B) &= \varepsilon_0\psi_{B0}(\boldsymbol{r}'_1\cdots\boldsymbol{r}'_B) = 0,\end{aligned} \tag{2.11}$$

hence Eqn (2.10) reduces to

$$\Big[E-\hat{T}_o-\langle\psi_{A0}\psi_{B0}|\hat{V}|\psi_{A0}\psi_{B0}\rangle-\langle\psi_{A0}\psi_{B0}|\hat{V}\hat{Q}\frac{1}{E-\hat{Q}\hat{H}\hat{Q}}\hat{Q}\hat{V}|\psi_{A0}\psi_{B0}\rangle\Big]\chi_{00} = 0 \tag{2.12}$$

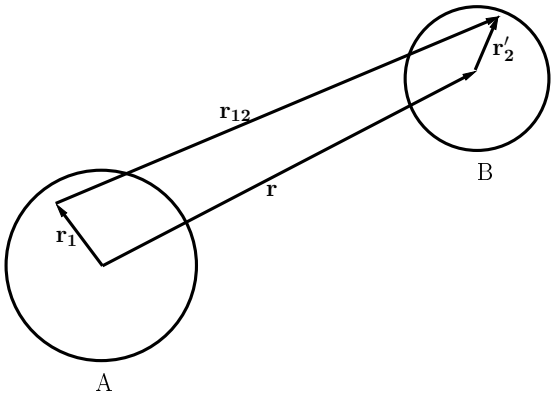

Figure 2.2: The composite system showing the folding potential coordinates [53].

where the operator $\hat{V} = \sum_{ij} v(\boldsymbol{r}_{ij})$. Thus we have reduced the eigenvalue problem of Eqn (2.4) to a SWE

$$\Big[E - \hat{T}_o - U(\boldsymbol{r})\Big]\chi_{00} = 0 \tag{2.13}$$

describing the relative motion. The optical potential $U(\boldsymbol{r})$ is thus given by

$$U(\boldsymbol{r}) = \langle \psi_{A0}\psi_{B0}|\hat{V}|\psi_{A0}\psi_{B0}\rangle - \langle \psi_{A0}\psi_{B0}|\hat{V}\hat{Q}\frac{1}{E - \hat{Q}\hat{H}\hat{Q}}\hat{Q}\hat{V}|\psi_{A0}\psi_{B0}\rangle \tag{2.14}$$

where the first term describes the interacting nuclei in their ground states. The second term is complex, non-local, energy and angular momentum dependent [53]. The first term simplifies[3] to the required folding potential V_F of interest which, explicitly, is given by [53];

$$V_F(\boldsymbol{r}) = \iint \rho_A(\boldsymbol{r_1})\rho_B(\boldsymbol{r'_2})v(\boldsymbol{r}_{12} = \boldsymbol{r} + \boldsymbol{r'_2} - \boldsymbol{r_1})d\boldsymbol{r_1}d\boldsymbol{r'_2} \tag{2.15}$$

where $\boldsymbol{r_1}$ and $\boldsymbol{r'_2}$ represent the coordinates of nucleon 1 in the target and nucleon 2 in the projectile, $\boldsymbol{r}_{12}$ is their separation distance as illustrated in Figure (2.2), $\rho_A(\boldsymbol{r_1})$ and $\rho_B(\boldsymbol{r'_2})$ are the matter densities of the target and projectile respectively, and $v(\boldsymbol{r}_{12})$ is the NN interaction between nucleons 1 and 2.

The antisymmetrization effect may now be included by replacing $\hat{V}$ with $(1 - \hat{P}_{12})\hat{V}$ in the first term of Eqn (2.14), where $\hat{P}_{12}$ interchanges all the coordinates of particles 1 and 2. Thus

[3] See Appendix A1.1

the folding potential V_F becomes [53];

$$V_F = \langle \psi_{A0}\psi_{B0}|(1-\hat{P}_{12})\hat{V}|\psi_{A0}\psi_{B0}\rangle \tag{2.16}$$

$$= \langle \psi_{A0}\psi_{B0}|\hat{V}|\psi_{A0}\psi_{B0}\rangle - \langle \psi_{A0}\psi_{B0}|\hat{V}|\psi_{B0}\psi_{A0}\rangle \tag{2.17}$$

where the potential V_F splits into the direct and exchange components respectively. We note however that the replacement of $\hat{V}$ with $(1-\hat{P}_{12})\hat{V}$ in Eqn (2.16) is equivalent to replacing the NN interaction $v(\boldsymbol{r}_{12})$ with $(1-\hat{P}_{12})v(\boldsymbol{r}_{12})$ in Eqn (2.15). Therefore the folding potential simplifies to

$$\begin{aligned} V_F(\boldsymbol{r}) &= \iint \rho_A(\boldsymbol{r_1})\rho_B(\boldsymbol{r'_2})(1-\hat{P}_{12})v(\boldsymbol{r}_{12})d\boldsymbol{r_1}d\boldsymbol{r'_2} \\ &= \iint \rho_A(\boldsymbol{r_1})\rho_B(\boldsymbol{r'_2})(v(\boldsymbol{r}_{12})-\hat{P}_{12}v(\boldsymbol{r}_{12}))d\boldsymbol{r_1}d\boldsymbol{r'_2} \\ &= \iint \rho_A(\boldsymbol{r_1})\rho_B(\boldsymbol{r'_2})(v(\boldsymbol{r}_{12})+\hat{J}(E)\delta(\boldsymbol{r}_{12}))d\boldsymbol{r_1}d\boldsymbol{r'_2} \end{aligned} \tag{2.18}$$

where $-\hat{P}_{12}v(\boldsymbol{r}_{12})$ has been approximated with a zero range pseudopotential $\hat{J}(E)\delta(\boldsymbol{r}_{12})$ [53, 54] in Eqn (2.18).

2.3.1 Nuclear Density of the Subsystems

The nuclear densities $\rho_1(r_1)$ and $\rho_2(r_2)$ represent the distribution of the centres of mass of the nucleons in the ground state of each nucleus. The nucleon density distribution is defined as the sum of the probability distributions over all occupied states weighted by the occupation number ω_i [55];

$$\rho(r) = \sum_i \omega_i \phi_i^*(r)\phi_i(r) \tag{2.19}$$

where $\phi_i(r)$ is the wavefunction of the particle at position r in the i^{th} state.

The density distribution of Eqn (2.19) may be obtained from experimentally measured charge densities unfolded with nucleon charge densities [53, 55]. Sometimes characteristic functional forms fitted to the experimental data are used to determine the matter densities. For example two and three parameter Fermi functions are commonly used for heavy nuclei and a Gaussian function for the light nuclei [32, 56]. The distribution may also be calculated using an accurate Hartree-Fock technique as in [57] or Shell model single particle potential method (SPP) [55]. These methods have been shown to reproduce results in good agreement with experiment.

2.3.2 Effective Nucleon-Nucleon Interaction

The free space NN interaction is considered to be too strong to be used directly in Eqn (2.18). This is mainly due to the strong repulsive core. The need to correct for the medium effects where each nucleon is embedded further suggest the need to replace the free NN interaction with an effective interaction $v_{eff}(\boldsymbol{r}_{12})$ [54].

The effective interaction is obtained by transforming a given free NN interaction $v(\boldsymbol{r}_{12})$ in a two step program so that the short range two nucleon correlation is systematically incorporated [53]. For a low energy ($E < 65$ MeV) process [58], the first step involves the transformation of a suitable bare NN interaction $v(\boldsymbol{r}_{12})$ into the matrix elements of a G-operator [58, 59] described by

$$\hat{G} = \hat{v} + \frac{\hat{Q}\hat{v}\hat{G}}{\varepsilon} \tag{2.20}$$

where the operator $\hat{v}$ is the appropriate free NN interaction and $\hat{Q}$ is a projector required to ensure the Pauli exclusion principle. The energy denominator ε is the difference between the energy of the correlated two nucleons interacting with a two-body potential $\hat{v}$ in the nuclear medium, and the sum of their single particle energies. The matrix elements of $\hat{G}$ in an unperturbed basis state (ψ) is related to the matrix element of the bare NN interaction by [51];

$$\langle\psi|\hat{G}|\psi\rangle = \langle\psi|\hat{v}|\phi\rangle \tag{2.21}$$

with ϕ being the two nucleon correlated wavefunction. The G-matrix of Eqn (2.20) is in fact a more realistic formal expression of the Bethe-Goldstone equation (see Appendix A1.3), which is finite for a singular interaction $\hat{v}$ [59].

The next step involves the transformation of the G-matrix elements into an effective NN interaction $\hat{v}_{eff}$. In practice, a local NN effective operator in each NN channel (Singlet-Even, Triplet-Even, Singlet-Odd and Triplet-Odd)[4] is first represented in the form of Eqn (2.1). A local ansatz is then assumed for each component and the parameters of the local potential adjusted until the momentum space matrix element of $\hat{v}_{eff}$ are matched to those of the G-operator [58].

The effective interaction of interest is the one obtained from a fit of the G-matrix elements in an oscillator basis to the sum of three Yukawa terms (M3Y) with ranges 0.25 fm, 0.4 fm and 1.414 fm. The ranges were chosen to simulate multiple pion exchanges, to improve the accuracy of the fit and to ensure the one pion exchange (OPEP) character of the tail [60]. A widely used form of the M3Y effective interaction $v_{eff}(\boldsymbol{r}_{12})$ derived from Reid soft-core NN potential is given

[4] See Appendix A1.2

by

$$\begin{aligned} v_{eff}(\boldsymbol{r}_{12}) &\simeq V_o(r_{12}) \\ &\simeq \Big[7999\frac{\exp(-4r_{12})}{4r_{12}} - 2134\frac{\exp(-2.5r_{12})}{2.5r_{12}}\Big] \end{aligned} \tag{2.22}$$

with an exchange component (v_{eff}^{ex}) of the form

$$\begin{aligned} v_{eff}^{ex}(\boldsymbol{r}_{12}) &\simeq \hat{J}_{oo}(E)\delta(r_{12}) \\ &\simeq -276(1 - 0.005E/A)\delta(r_{12}). \end{aligned} \tag{2.23}$$

The approximations in Eqns (2.22) and (2.23) have been used to indicate a fit to the spin and isospin independent part of the central component of the effective NN operator and the ratio E/A is the bombarding energy per nucleon. Numerical computation of the M3Y potential is best done in the momentum space representation which is given in Appendix A1.4.

Chapter 3

Phenomenological Core-cluster Potential

3.1 Introduction

In this chapter we describe the development of a phenomenological core-cluster potential for a cluster model description of nuclei. We also discuss the theoretical framework which will enable us to make model predictions for comparison with experimental observations. Here we pay particular attention to energy spectra, to lifetimes for the decay of a parent state into the cluster and core, and to electromagnetic transition probabilities.

An important further test of the assumed core-cluster potential would involve an analysis of the elastic scattering of the cluster by the core. A potential which reproduces the structure information mentioned above should also provide a reasonable description of the real part of the optical potential describing the low energy core-cluster elastic scattering. Some ambiguities arise however because of the complex nature of the optical potential, and in this thesis we concentrate on the structure properties of the core-cluster systems, with particular emphasis on the alpha plus ^{208}Pb closed core system.

One may generate the core-cluster potential using the underlying nucleon-nucleon interaction as detailed in chapter two. One may also proceed phenomenologically by choosing a likely form of the potential and optimizing its parameter values. We next describe the development of one such functional form, the Saxon-Wood plus Saxon-Wood cubed (SW+SW^3) form, which has been successfully used to reproduce much experimental data across the chart of nuclide.

3.1.1 Applications to Light Nuclei

The properties of bound and resonant states in light nuclei have been obtained using a cluster model with a local folding potential of the form

$$V_N(\boldsymbol{r}) = \frac{-2\pi\hbar^2}{M}\overline{f}\int \rho_B(\boldsymbol{r_1}-\boldsymbol{r})\rho_A(\boldsymbol{r_1})d\boldsymbol{r_1} \tag{3.1}$$

where ρ_A and ρ_B are the core and cluster densities respectively, M is the nucleon mass and $\overline{f}$ is an adjustable real strength parameter [6]. Equation (3.1) corresponds to a simplified form of the folding potential[5] in the previous chapter with a zero range effective interaction, i.e. $v_{eff}(\boldsymbol{r_{12}})$ proportional to $\delta(\boldsymbol{r_{12}})$. Exchange effects and short range correlations are neglected [50]. Although the Pauli principle is partly accounted for by ensuring that the nucleon states of the cluster lie above those of the core, any remaining effects are assumed negligible. Another fundamental assumption is that the in-medium cluster and core nuclei retain their free space properties.

Despite these shortcomings, important properties such as the level ordering and spacings of the ground state and excited bands in light nuclei were obtained in good agreement with observed results [6]. For example Figure (3.1) gives the ground state rotational band of ^{20}Ne obtained by treating the nucleus as an alpha cluster plus ^{16}O core. Similar success was recorded for the properties of ^{16}O considered as an alpha cluster plus a ^{12}C core [6].

A more phenomenological approach is to choose some likely form of the core-cluster potential and optimize its parameters so as to reproduce observed nuclear properties. One such candidate is the Saxon-Wood (SW) form which, for the nucleon-nucleus potential, has an underlying microscopic foundation. For instance, putting $\rho_B(\boldsymbol{r_1}-\boldsymbol{r}) \simeq \delta(\boldsymbol{r_1}-\boldsymbol{r})$ in Eqn (3.1) yields

$$V_N(r) = -V_o\rho_A(r) = \left[\frac{-V_o}{1+\exp\left(\frac{r-R}{a}\right)}\right] \tag{3.2}$$

where we have used a two-parameter Fermi function for the density $\rho_A(r)$ so that the strength $V_o = \frac{-2\pi\hbar^2\overline{f}\rho_o}{M}$, and ρ_o is obtained from a normalization of the density $\rho_A(r)$. The appearance of the three parameters, namely, the depth V_o, the radius R, and the diffuseness a is a common feature of a number of phenomenological potentials.

The SW potential of Eqn (3.2) has been widely used in the independent single particle shell model. It takes the shape of the nuclear density and a physically reasonable geometry is one with $R \sim 1.2\mathrm{A}^{1/3}$ fm, where A is the mass number, and $a \sim 0.65$ fm [10].

It has however been shown that the standard SW potential in Eqn (3.2) results in an inverted or degenerate level scheme for the alpha cluster states in light nuclei, and that the depth V_o must

[5] $V_N(\boldsymbol{r}) = \int d\boldsymbol{r_1}\rho_A(\boldsymbol{r_1})\int d\boldsymbol{r_2'}\rho_B(\boldsymbol{r_2'})\delta(\boldsymbol{r_2'}-(\boldsymbol{r_1}-\boldsymbol{r})) = \int d\boldsymbol{r_1}\rho_A(\boldsymbol{r_1})\rho_B(\boldsymbol{r_1}-\boldsymbol{r})$.

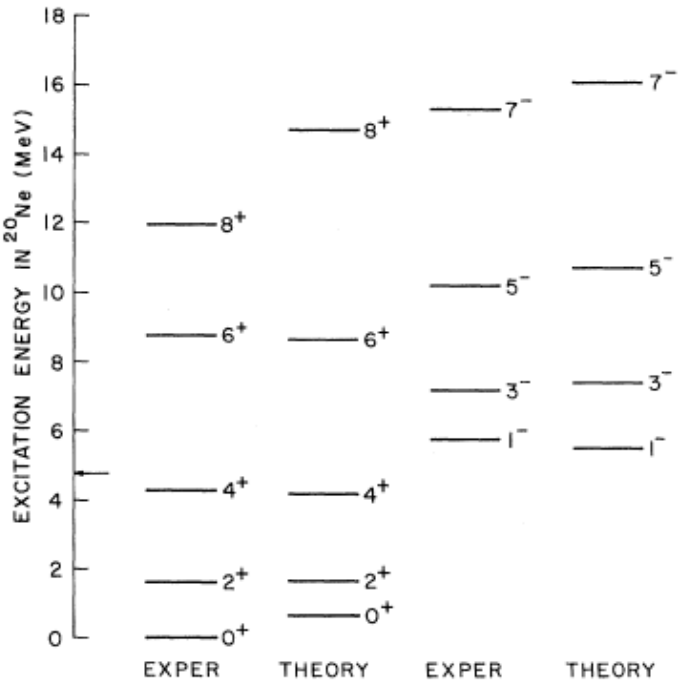

Figure 3.1: A comparison of the experimental and the calculated positive parity ground state $K = 0^+$ ($\overline{f} = 1.237$ fm) and the negative parity $K = 0^-$ ($\overline{f} = 1.325$ fm) bands of ^{20}Ne [6].

be adjusted for each state to obtain the level ordering in agreement with experiment as shown in Figure (3.2) for ^{20}Ne [6].

This is clearly undesirable [61] and shows a deficiency of the SW functional form for the description of these cluster states. Furthermore the SW potential also failed to describe the observed anomalous large back angle scattering (ALAS) of alpha particles by closed shell nuclei [62]. The enhancement of the differential cross sections at backward angles was, however, well described by a SW^2 Michel potential [63].

The Michel potential has further been shown to give a good description of the properties of ^{20}Ne and ^{44}Ti [63, 64], when used in alpha-cluster model analyses of these nuclei.

Another successful parameterization of the nuclear potential used in studies of clustering in light nuclei is the three parameter Cosh potential (see Eqn (1.4)). This potential was first used to study the cluster structure of ^{19}F [61] where it was considered as a plausible symmetrized form of the SW potential. It was observed that a high degree of clustering at the nuclear surface could account for the large B($E2$) values of light nuclei. The Cosh potential, together with an additional tensor interaction, has also been shown to give a good description of the structure of ^{24}Mg [39] treated as two ^{12}C clusters. It has further been used to describe the alpha cluster states in the beginning of the *fp*-shell region [65] where several nuclei, including ^{40}Ca, are considered.

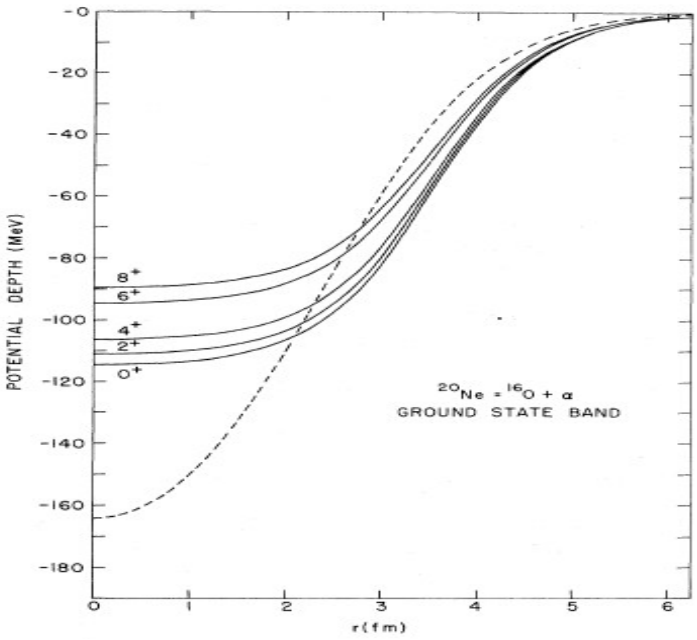

Figure 3.2: The SW potential with $R = 3.53$ fm, $a = 0.6$ fm and varying depth V_o (solid lines) compared with the folded potential (dashed line) of Eqn (3.1) with $\overline{f} = 1.237$ fm for ^{20}Ne treated as $\alpha + ^{16}$ O system [6].

It may therefore be considered as a good candidate for investigation of the cluster states in heavy nuclei.

3.1.2 Applications to Heavy Nuclei

The widespread phenomenon of alpha radioactivity in heavy nuclei provides some evidence for alpha clustering in these nuclei. Particular examples of likely candidates for such clustering include ^{212}Po, ^{136}Te and ^{94}Mo all of which could be considered as alpha plus doubly closed shell nuclei.

A common feature of many forms of the core-cluster potentials which successfully describe alpha clustering in light nuclei is that they fail to reproduce the properties of heavier nuclei in a consistent manner. Thus for example the application of a Cosh potential to alpha decay over a wide range of heavy nuclei generates the decay half-lives to within a factor of 2 - 3 of the observed values [26, 66]. However it fails to simultaneously reproduce the observed spectra of the above list of alpha plus doubly closed shell nuclei resulting, for example, in the inverted spectrum of ^{212}Po given in Table (3.1).

J^{π}	E_{expt}(MeV)	E_{cal}(MeV)
0^{+}	0.000	0.000
2^{+}	0.727	-0.300
4^{+}	1.132	-1.020
6^{+}	1.355	-2.220
8^{+}	1.476	-3.970
10^{+}	1.834	-6.366
12^{+}	2.702	-9.510
14^{+}	2.885	-13.560
16^{+}	-	-18.680
18^{+}	2.921	-25.140
20^{+}	-	-33.357
22^{+}	-	-43.962

Table 3.1: The alpha cluster states of ^{212}Po obtained with Cosh potential parameter values V_o = 162.3 MeV, R = 7.380 fm, a = 0.4 fm, G = 22 [66]. The calculated ground state decay half-life is 0.13 μs compared with the experimental value of 0.30 μs. The 16^{+}, 20^{+} and 22^{+} states have not been detected experimentally.

A suitable phenomenological form of the potential which provides a simultaneous description of these properties was found [12, 37] in a mixed SW+SW^3 form given by

$$V_N(r) = -V_o\left[\frac{x}{1+\exp\left(\frac{r-R}{a}\right)} + \frac{1-x}{\left[1+\exp\left(\frac{r-R}{3a}\right)\right]^3}\right]. \tag{3.3}$$

More generally it has been found that the SW+SW^3 potential can also describe exotic clustering when the depth V_o is defined as $V_o = v_o A_2$, with $v_o \sim 55$ MeV and A_2 the cluster mass number [37]. For alpha clustering $V_o \sim 220$ MeV, and typical values of the geometrical parameters are $x = 0.30$, $R = 1.2A^{1/3}$ fm, where A is the sum of the core and cluster mass numbers A_1 and A_2 respectively, and $a \sim 0.65$ fm [12].

There are obvious similarities between the SW+SW^3 and the successful SW^2 Michel potential, with the former also reproducing the ALAS phenomenon [49] in alpha scattering from ^{16}O and ^{40}Ca, as well as the low-energy alpha scattering from ^{208}Pb [67]. The SW+SW^3 functional form thus provides a suitable phenomenological starting point for a core-cluster potential.

3.2 Formalism of the Binary Cluster Model

In the binary cluster model the core and cluster are taken to interact via some central potential $V(r)$. A bound state wavefunction $\chi_{nLM}(r)$ of the relative motion separates into radial and angular components

$$\chi_{nLM}(r) = \frac{\psi_{nL}(r)}{r} Y_{LM}(\theta, \phi) \tag{3.4}$$

where the radial wavefunction $\psi_{nL}(r)$ is a solution of the radial Schrödinger Wave Equation (SWE)

$$\left[\frac{-\hbar^2}{2\mu}\frac{d^2}{dr^2} + V_N(r) + V_C(r) + V_L(r)\right]\psi_{nL}(r) = E_{nL}\psi_{nL}(r) \tag{3.5}$$

with $\mu = A_1A_2/(A_1 + A_2)$ being the reduced mass of the system, n the number of nodes of the radial wavefunction. The angular component is given by the spherical harmonics $Y_{LM}(\theta, \phi)$, where L and M are the orbital angular momentum and its z-projection respectively. The effective core-cluster interaction potential $V(r)$ is therefore the sum of the nuclear potential $V_N(r)$, the Coulomb potential $V_C(r)$ and the centrifugal potential $V_L(r)$ given by,

$$V(r) = V_N(r) + V_C(r) + V_L(r) \tag{3.6}$$

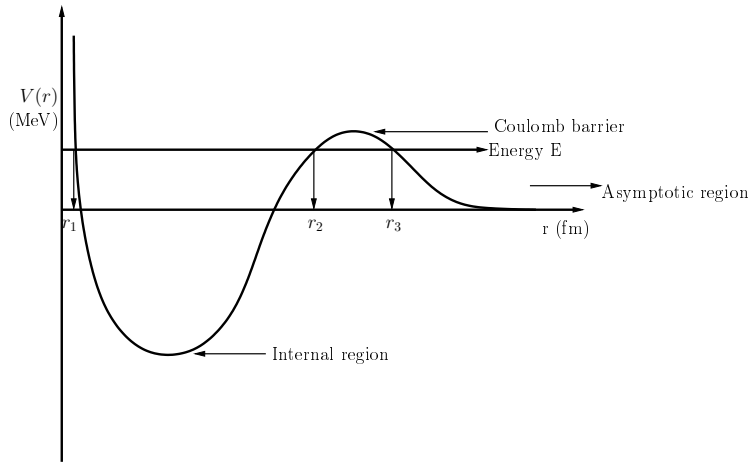

Figure 3.3: A schematic plot of the effective potential $V(r)$ against the core-cluster separation distance r. The turning points r_1,r_2 and r_3 where $E = V(r)$ are shown for a typical quasibound state.

where $V_N(r)$ may for example take the phenomenological form of Eqn (3.3) or the microscopic form of Eqn (2.18). The Coulomb potential $V_C(r)$ is taken as that for a point charge Z_2 interacting with a uniformly charged spherical core of charge Z_1 and radius R_C given by

$$V_C(r) = \begin{cases} \dfrac{Z_1 Z_2 e^2}{r} & \text{for } \; r \geq R_C \\ \dfrac{Z_1 Z_2 e^2}{2R_C}\left[3 - \left|\dfrac{r}{R_C}\right|^2\right] & \text{for } r \leq R_C. \end{cases} \tag{3.7}$$

The Coulomb radius R_C is often assumed to equal the nuclear potential radius R in order to minimize the number of free parameters [26]. The centrifugal potential $V_L(r)$ associated with the orbital angular momentum L is given by

$$V_L(r) = \frac{L(L+1)\hbar^2}{2\mu r^2}. \tag{3.8}$$

The Langer form of Eqn (3.8), with $L(L+1)$ replaced by $(L+\frac{1}{2})^2$ to ensure contribution for the $L = 0$ state, is used in all our calculations involving the Bohr-Sommerfeld quantization rule discussed in the following section.

The effective core-cluster interaction potential of Eqn (3.6) is shown in Figure (3.3) for a typical quasibound state.

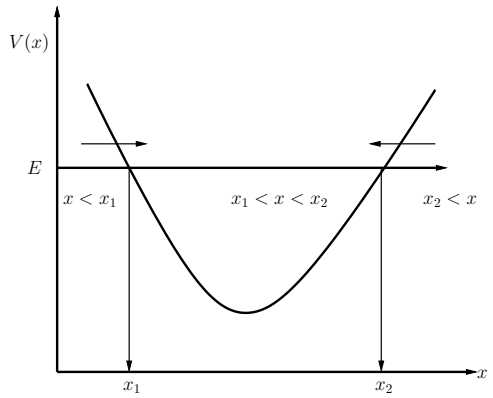

Figure 3.4: A one dimensional potential $V(x)$ showing the different regions and the turning points x_1 and x_2. The arrows indicate the connection rule.

3.2.1 Bohr-Sommerfeld Quantization Rule and Energy Spectra

The solution of the radial SWE may be obtained by considering the semi-classical Wentzel-Kramers-Brillouin (WKB) approximation for the one dimensional motion of a single particle with SWE

$$\left[\frac{-\hbar^2}{2\mu}\frac{d^2}{dx^2} + V(x)\right]\psi(x) = E\psi(x) \tag{3.9}$$

where the potential $V(x)$ and energy E may be represented as in Figure (3.4).

The regions $x < x_1$ and $x > x_2$ are the classically forbidden regions in which the potential $V(x) > E$ while $x_1 < x < x_2$ is the allowed region with $E > V(x)$.

The WKB approximation has been shown to be valid if the wavelength λ_o of the particle varies slightly over distances of the order of its size [68, 69];

$$\left|\frac{d\lambda_o}{dx}\right| \ll 1 \tag{3.10}$$

with the de Broglie wavelength $\lambda_o(x)$ given by

$$\lambda_o(x) = \frac{2\pi\hbar}{p(x)} = \frac{2\pi\hbar}{\sqrt{2\mu(E - V(x))}}. \tag{3.11}$$

The general solutions for the one dimensional SWE are given by [68];

$$\psi(x) = \frac{A_+}{\sqrt{p(x)}}\exp\left[\frac{i}{\hbar}\int^x p(x')dx'\right] + \frac{A_-}{\sqrt{p(x)}}\exp\left[-\frac{i}{\hbar}\int^x p(x')dx'\right] \tag{3.12}$$

for the classically allowed region $E > V(x)$ and

$$\psi(x) = \frac{B_+}{\sqrt{|p(x)|}} \exp\left[\frac{1}{\hbar}\int^{x} |p(x')|dx'\right] + \frac{B_-}{\sqrt{|p(x)|}} \exp\left[-\frac{1}{\hbar}\int_{x} |p(x')|dx'\right] \tag{3.13}$$

for the forbidden regions $E < V(x)$ with $A_\pm$ and $B_\pm$ being arbitrary constants and the subscripts $\pm$ indicate the respective directions. The approximation, however, fails at the classical turning points x_1 and x_2 where the particle may have a zero momentum with $V(x) = E$.

The turning point problem is usually fixed by the WKB connection formulae in which the solutions for both the classically allowed and forbidden regions are connected by some approximation taken at each turning point. For example the solutions at both sides of x_1 may be connected as follows [68, 69];

$$\frac{C}{2\sqrt{|p(x)|}} \exp\left[\frac{1}{\hbar}\int_{x_1}^{x} |p(x')|dx'\right] \longrightarrow \frac{C}{\sqrt{|p(x)|}} \sin\left[\frac{1}{\hbar}\int_{x_1}^{x} p(x')dx' + \frac{\pi}{4}\right] \tag{3.14}$$

and similarly at x_2

$$\frac{D}{\sqrt{|p(x)|}} \sin\left[\frac{1}{\hbar}\int_{x}^{x_2} p(x')dx' + \frac{\pi}{4}\right] \longleftarrow \frac{D}{2\sqrt{|p(x)|}} \exp\left[\frac{1}{\hbar}\int_{x}^{x_2} |p(x')|dx'\right] \tag{3.15}$$

where C and D are arbitrary constants. The arrows imply that the solution at the tail continues into the solution at the arrow head for regions on the opposite sides of a turning point but not vice-versa.

Combining the oscillatory solutions in the classically allowed region in Eqns (3.14) and (3.15) between x_1 and x_2 gives the well known Bohr-Sommerfeld (BS) quantization integral for the one dimensional system [68, 69];

$$\int_{x_1}^{x_2} \sqrt{\frac{2\mu}{\hbar^2}\big[E - V(x)\big]}dx = (2n+1)\frac{\pi}{2} \tag{3.16}$$

where μ is the particle mass and n the number of nodes. The similarity between Eqn (3.5) and Eqn (3.9) then allows a generalization to three dimensional systems. For the three dimensional case we thus find

$$\int_{r_1}^{r_2} \sqrt{\frac{2\mu}{\hbar^2}\big[E - V(r)\big]}dr = (2n+1)\frac{\pi}{2}. \tag{3.17}$$

A quasibound cluster therefore moves back and forth in the internal region between the turning points r_1 and r_2 (see Figure 3.3) before tunneling through the Coulomb barrier into the asymptotic region.

The eigenvalues obtained from Eqn (3.17) have been found to provide a good approximation to the eigenvalues from exact numerical solution of the SWE as shown in Appendix B1.3. Thus for computational convenience we shall implement our extensive parameter optimizations using the BS relation of Eqn (3.17) and supplement our calculations with wavefunctions from the numerical solution of the SWE where necessary.

3.2.2 Cluster States and Quantum Numbers

The Pauli principle requires that the cluster nucleons be placed above the Fermi surface of the core nucleus. This is approximately satisfied through the Wildermuth condition which states that

$$G = 2n + L = \sum_{i=1}(2n_i + l_i) - \overline{g} \tag{3.18}$$

where G is the global quantum number of the core-cluster relative motion, n the number of nodes of the radial wavefunction and L the orbital angular momentum. The quantum numbers n_i and l_i are the corresponding quantities for the cluster nucleons, and $\overline{g}$ is the number of quanta taken up by the cluster internal motion.

The core-cluster relative motion therefore generates bands of states, each band characterized by a common value of G. For G even the states in the band have even angular momentum $L = 0$ (2) G which correspond to the low-lying positive parity states of even-even nuclei, whereas $L = 1$ (2) $G + 1$ corresponds to a negative parity band [12]. For a given band specified by its value of G, Eqn (3.17) may be rewritten as

$$\int_{r_1}^{r_2} \sqrt{\frac{2\mu}{\hbar^2}\big[E_L - V(r)\big]}dr = (G - L + 1)\frac{\pi}{2}. \tag{3.19}$$

For example, in a simple alpha cluster model of ^{212}Po each cluster proton contributes $5\hbar\omega$ and each neutron contributes $6\hbar\omega$. Subtracting the quanta for the cluster internal motion (zero for alpha cluster) gives a total of

$$G = (2 \times 6) + (2 \times 5) - 0 = 22$$

for the lowest positive parity band.

However, this estimate of G is only valid for systems in which the core and cluster nucleons move in oscillator potentials with a common oscillator length. Other approximate definitions for G have also been given by Buck *et al.* [41]. Thus if the potential $V(r)$ is known, and the band global quantum number G specified, the energy E_L corresponding to each possible value of the angular momentum L and hence the energy levels of the band can be calculated using Eqn (3.19).

3.2.3 Decay Half-life and Tunneling

The decay half-life of an element is defined as the time taken to halve the number of radioactive nuclei in a given sample of the element. It is given by

$$T_{1/2} = \frac{\ln 2}{\Lambda}. \tag{3.20}$$

For the break-up of a nucleus into a core and cluster the decay constant Λ is defined as the product of the assault frequency f, the penetrability $\overline{T}$ of the cluster through the potential barrier [6] and the core-cluster preformation probability P in the parent nucleus, that is

$$\Lambda = f\overline{T}P. \tag{3.21}$$

The frequency f is given by [12];

$$f = \frac{\hbar}{2\mu \int_{r_1}^{r_2} dr/k(r)} = \frac{\hbar N}{4\mu} \tag{3.22}$$

where the wavenumber $k(r)$ is

$$k(r) = \frac{|p(r)|}{\hbar} = \sqrt{\frac{2\mu}{\hbar^2}|E - V(r)|} \tag{3.23}$$

and the normalization factor N is given by [70];

$$N \int_{r_1}^{r_2} dr[k(r)]^{-1} = 2. \tag{3.24}$$

For a constant wavenumber $k(r) = k'$, Eqn (3.22) reduces to

$$f = \frac{\hbar k'}{2\mu(r_2 - r_1)} = \frac{\upsilon}{2(r_2 - r_1)} \tag{3.25}$$

with particle velocity $\upsilon = \hbar k'/\mu$.
The penetrability $\overline{T}$ is defined as the ratio of the transmitted flux to the incident flux densities [71];

$$\overline{T} = \frac{\upsilon_{tr}|\psi_{tr}|^2}{\upsilon_{in}|\psi_{in}|^2} \tag{3.26}$$

where υ_{in} and ψ_{in} are the particle velocity and wavefunction incident on the barrier while υ_{tr} and ψ_{tr} are the corresponding transmitted quantities.

The one dimensional WKB connection formulae at the turning points of a reasonably wide

[6] $\overline{T}$ is used to differentiate the penetrability from the kinetic energy operator.

potential barrier generalized to three dimensions can further be used to show that the transmission probability reduces to [69];

$$\overline{T} = \exp\Big[-2\int_{r_2}^{r_3} k(r)dr\Big] \tag{3.27}$$

using $\upsilon_{in} = \upsilon_{tr}$ [71]. The associated physical process is the so called tunneling effect.
Putting Eqns (3.22) and (3.27) in Eqn(3.21) gives

$$\Lambda = P\frac{\hbar N}{4\mu}\exp\Big[-2\int_{r_2}^{r_3} k(r)dr\Big], \tag{3.28}$$

and hence the decay width Γ

$$\begin{aligned}\Gamma &= \hbar\Lambda \\ &= PN\frac{\hbar^2}{4\mu}\exp\Big[-2\int_{r_2}^{r_3} k(r)dr\Big] \\ &= P\frac{\hbar^2}{2\mu}\frac{\exp\Big[-2\int_{r_2}^{r_3} k(r)dr\Big]}{\int_{r_1}^{r_2} dr[k(r)]^{-1}}.\end{aligned} \tag{3.29}$$

Once all the input parameters are known or optimised as desired, the decay half-life may be obtained from

$$T_{1/2} = \frac{\hbar\ln 2}{\Gamma}. \tag{3.30}$$

Given the energy E (Q-value) and the potential $V(r)$ governing the decay, see Figure (3.3), the only quantity that remains to be defined for a complete description of the decay half-life is the probability P of having a preformed cluster-core system in the initial state. For alpha clustering in the ^{212}Po ground state much effort has been devoted to calculations of the preformation probability from a shell model based microscopic point of view [17, 22]. As indicated in the Introduction the values obtained increase markedly with sophistication of the model, ranging from an order of 10^{-5} in the work of Mang [17] to 0.025 in that of Lovas *et al.* [21] who used combined shell and cluster model configurations.

At its simplest the cluster model assumes that the states of a given band are described by the relative motion of a core and cluster in their respective ground states, so that the probability $P = 1$, and this assumption is tested by comparing model derived quantities with their observed values.

3.2.4 Electromagnetic Transitions

Residual nuclei are most often left in excited states following nuclear reactions. The subsequent emission of a quantum of radiation with specific angular momentum via de-excitation to lower states and/or the inverse process of absorption are referred to as the electromagnetic transition processes.

The transition probability is defined as the probability of emission per unit time of a quantum of radiation with angular momentum (ℓ, m) from an initial state (J_i, M_i) to a final state (J_f, M_f) and is given by [9];

$$\Lambda(\ell; J_i \longrightarrow J_f) = \frac{8\pi(\ell+1)k^{2\ell+1}}{\ell\hbar\big[(2\ell+1)!!\big]^2} B(\ell; J_i \longrightarrow J_f) \tag{3.31}$$

for both the electric $E(\ell)$ and magnetic $M(\ell)$ transitions, with changes of parities given by

$$E(\ell; J_i \longrightarrow J_f) = (-1)^{\ell},$$

and

$$M(\ell; J_i \longrightarrow J_f) = (-1)^{\ell+1}. \tag{3.32}$$

The conservation of angular momentum must be satisfied through

$$\mathbf{J}_i = \mathbf{J}_f + \boldsymbol{\ell} \tag{3.33}$$

and the selection rules for allowed transitions are thus given by

$$|J_i - J_f| \leq \ell \leq J_i + J_f$$

and

$$M_i = M_f + m \tag{3.34}$$

for each multipole of radiation.
In Eqn (3.31) the wave number $k = E_\gamma/\hbar c$ where the radiation energy $E_\gamma (= E_i - E_f)$. The reduced transition probability $B(\ell; J_i \longrightarrow J_f)$ is the squared matrix element of the correponding multipole operator $(\hat{O}_{\ell m})$ for a particular transition;

$$B(\ell; J_i \longrightarrow J_f) = \sum_{m M_f} |\langle J_f M_f | \hat{O}_{\ell m} | J_i M_i \rangle|^2 \tag{3.35}$$

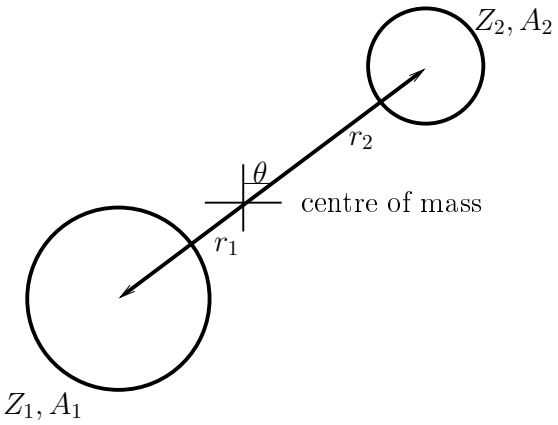

Figure 3.5: A schematic representation of the core-cluster relative motion coordinates [62].

where the summation is taken over all possible orientations m and M_f of the final spin states. The multipole operator of order ℓ, m for the electric transitions of interest here is given by;

$$\hat{O}_{\ell m}(E\ell) = \sum_{i=1}^{A} e_i r_i^{\ell} Y_{\ell m}^{*}(\theta_i, \phi_i) \tag{3.36}$$

where

$$e_i = \begin{cases} e & \text{for proton} \\ \\ 0 & \text{for neutron.} \end{cases}$$

The sum in Eqn (3.36) thus reduces to one taken over all the protons at position (r_i, θ_i, ϕ_i). For our model this amounts to a sum over the two total charges Z_1 and Z_2 of the core and cluster respectively as illustrated in Figure (3.5), thus

$$\begin{aligned} \hat{O}_{\ell m}(E\ell) = \sum_{i=1}^{Z} e_i r_i^{\ell} Y_{\ell m}^{*}(\theta_i, \phi_i) &= Z_1 r_1^{\ell} Y_{\ell m}^{*}(\theta_1, \phi_1) + Z_2 r_2^{\ell} Y_{\ell m}^{*}(\theta_2, \phi_2) \\ &= Z_1 r_1^{\ell} Y_{\ell m}^{*}(\pi - \theta, \pi + \phi) + Z_2 r_2^{\ell} Y_{\ell m}^{*}(\theta, \phi) \\ &= \left[(-1)^{\ell} Z_1 r_1^{\ell} + Z_2 r_2^{\ell}\right] Y_{\ell m}^{*}(\theta, \phi) \\ &= \left[Z_1 \left(\frac{-A_2 r}{A} \right)^{\ell} + Z_2 \left(\frac{A_1 r}{A} \right)^{\ell} \right] Y_{\ell m}^{*}(\theta, \phi) \\ &= \left[Z_1 \left(\frac{-A_2}{A} \right)^{\ell} + Z_2 \left(\frac{A_1}{A} \right)^{\ell} \right] r^{\ell} Y_{\ell m}^{*}(\theta, \phi). \end{aligned} \tag{3.37}$$

The wavefunction for the core-cluster relative motion is given by (see Eqns (3.4) and (3.5))

$$|LM\rangle = \frac{\psi_L(r)}{r} Y_{LM}(\theta, \phi) \tag{3.38}$$

so that the $B(E\ell)$ for the core-cluster system may be written as

$$B(E\ell; L_i \longrightarrow L_f) = \sum_{mM_f} |\langle L_f M_f | \hat{O}_{\ell m}(E\ell) | L_i M_i \rangle|^2. \tag{3.39}$$

For a single transition of order ℓ from an initial state $|L_i M_i\rangle$ to the ground state with $L_f = 0$ and $M_f = 0$, the selection rule requires that $L_i = \ell$ and $M_i = m$. Thus using Eqn (3.37) in Eqn (3.39) we have

$$B(E\ell; \ell \longrightarrow 0^+) = \left| \left\langle \frac{\psi_0(r)}{r} Y_{00}(\hat{r}) \right| \left[Z_1 \left(\frac{-A_2}{A} \right)^\ell + Z_2 \left(\frac{A_1}{A} \right)^\ell \right] r^\ell Y^*_{\ell m}(\hat{r}) \left| \frac{\psi_\ell(r)}{r} Y_{\ell m}(\hat{r}) \right\rangle \right|^2$$

which reduces to

$$B(E\ell; \ell \longrightarrow 0^+) = \frac{1}{4\pi} \left| \left[Z_1 \left(\frac{-A_2}{A} \right)^\ell + Z_2 \left(\frac{A_1}{A} \right)^\ell \right] \int_0^\infty \frac{\psi_0^*(r)}{r} r^\ell \frac{\psi_\ell(r)}{r} r^2 dr \right|^2. \tag{3.40}$$

We note that the transition strength decreases rapidly with increasing multipolarity [72]. The multipolarities of most interest are the dipole ($\ell = 1$) and the quadrupole ($\ell = 2$) transitions respectively.

Dipole Transitions

These involve transitions with $\ell = 1$ between states of opposite parities so that

$$B(E1; 1^- \longrightarrow 0^+) = \frac{1}{4\pi} \left| \left[Z_1 \left(\frac{-A_2}{A} \right) + Z_2 \left(\frac{A_1}{A} \right) \right] \int_0^\infty \psi_0^*(r) r \psi_1(r) dr \right|^2. \tag{3.41}$$

It is known that the $B(E1)$ between low-lying states are very small for heavy nuclei [73] and hence

$$Z_1 \left(\frac{-A_2}{A} \right) + Z_2 \left(\frac{A_1}{A} \right) \approx 0 \tag{3.42}$$

which gives the important no dipole condition [73]

$$\frac{Z_1}{A_1} = \frac{Z_2}{A_2} = \frac{Z}{A} \tag{3.43}$$

with $A = A_1 + A_2$ and $Z = Z_1 + Z_2$.

Quadrupole Transitions

These involve transitions with $\ell = 2$ between states of the same parity so that

$$B(E2; 2^+ \longrightarrow 0^+) = \frac{1}{4\pi}\left|\left[Z_1\left(\frac{-A_2}{A}\right)^2 + Z_2\left(\frac{A_1}{A}\right)^2\right]\int_0^\infty \psi_0^*(r) r^2 \psi_2(r) dr\right|^2 \tag{3.44}$$

which reduces to

$$B(E2; 2^+ \longrightarrow 0^+) \approx \frac{1}{4\pi}\left|\frac{Z_1 Z_2}{Z}\int_0^\infty \psi_0^*(r) r^2 \psi_2(r) dr\right|^2 \tag{3.45}$$

upon the application of the no dipole condition.

3.2.5 Reduced Probability For Arbitrary Transitions

For an electric transition of multipolarity ℓ from an initial binary cluster state of angular momentum L_i to a final state of angular momentum L_f, a generalised reduced transition probability is given by

$$\begin{aligned}
B(E\ell; L_i \longrightarrow L_f) &= \sum_{mM_f} \left|\langle L_f M_f | \hat{O}_{\ell m}(E\ell) | L_i M_i \rangle\right|^2 \\
&= \sum_{mM_f} \left|\langle L_f M_f | \beta_\ell r^\ell Y^*_{\ell m}(\theta, \phi) | L_i M_i \rangle\right|^2 \\
&= \sum_{mM_f} \left|(-1)^m \langle L_f M_f | \beta_\ell r^\ell Y_{\ell -m}(\theta, \phi) | L_i M_i \rangle\right|^2 \\
&= \sum_{mM_f} \left|\langle L_i M_i \ell -m | L_f M_f \rangle\right|^2 \left|\langle L_f || \beta_\ell r^\ell Y_\ell || L_i \rangle\right|^2 \\
&= \sum_{mM_f} \frac{2L_f + 1}{2L_i + 1} \left|\langle L_f M_f \ell m | L_i M_i \rangle\right|^2 \left|\langle L_f || \beta_\ell r^\ell Y_\ell || L_i \rangle\right|^2 \\
&= \frac{2L_f + 1}{2L_i + 1} \left|\langle L_f || \beta_\ell r^\ell Y_\ell || L_i \rangle\right|^2 \\
&= \left(\frac{\hat{L}_f}{\hat{L}_i}\right)^2 \left|\langle L_f || \beta_\ell r^\ell Y_\ell || L_i \rangle\right|^2
\end{aligned} \tag{3.46}$$

where we have made use of the integer nature of L_i, L_f, ℓ and m, the orthogonality relation of the Clebsch-Gordon coefficients(CG), and the Brink and Satchler [74] definition of the reduced matrix element.

Evaluating the reduced matrix element in Eqn (3.46) gives [74];

$$B(E\ell; L_i \longrightarrow L_f) = \frac{1}{4\pi}\left(\frac{\hat{L}_f}{\hat{L}_i}\right)^2\left(\frac{\hat{L}_i\hat{\ell}}{\hat{L}_f}\langle L_i 0\ell 0|L_f 0\rangle\right)^2\left|\langle\psi_{L_f}|\beta_\ell r^\ell|\psi_{L_i}\rangle\right|^2$$
$$= \beta_\ell^2\left(\frac{\hat{\ell}^2}{4\pi}\right)\left(\langle L_i 0\ell 0|L_f 0\rangle\right)^2\left|\langle\psi_{L_f}|r^\ell|\psi_{L_i}\rangle\right|^2. \quad (3.47)$$

In the above expression we define

$$\beta_\ell = \left[Z_1\left(\frac{-A_2}{A}\right)^\ell + Z_2\left(\frac{A_1}{A}\right)^\ell\right]$$

and

$$\hat{L} = \sqrt{2L+1}$$

for conciseness.

For a transition to the nuclear ground state with $L_f = 0^+$ we then have $L_i = \ell$ and Eqn (3.47) reduces to[7]

$$B(E\ell; \ell \longrightarrow 0^+) = \beta_\ell^2\left(\frac{1}{4\pi}\right)\left|\langle\psi_0|r^\ell|\psi_\ell\rangle\right|^2 \quad (3.48)$$

which is in agreement with the directly obtained result of Eqn (3.40).

We note here that the transition strength $B(E\ell)$ may be expressed in terms of the Weisskopf single particle estimate given by [9];

$$B(E\ell) = e^2\frac{1}{4\pi}\langle r^\ell\rangle^2$$
$$\approx \frac{1}{4\pi}\left[\left(\frac{3}{\ell+3}\right)r_o^\ell A^{\frac{\ell}{3}}\right]^2 e^2\mathrm{fm}^{2\ell} \quad (3.49)$$

with $r_o = 1.2$ fm. Thus, for example, the conversion between the Weisskopf unit (W.u.) and $e^2\mathrm{fm}^4$ for the quadrupole transition is given by

$$1 \text{ W.u.} = \frac{0.746}{4\pi}A^{\frac{4}{3}}\ e^2\mathrm{fm}^4 \quad (3.50)$$

where $A = A_1 + A_2$ is the mass number and e is the size of an electric charge.

[7] $\left(\langle \ell 0\ell 0|00\rangle\right)^2 = (-1)^{(2\ell)}\left(1/\hat{\ell}^2\right)$.

3.2.6 Electromagnetic Decay Width

Observations have shown that electromagnetic de-excitation may not involve gamma or photon emission in cases where the transition is forbidden or the energy is too small (∼keV) but large enough to emit orbital electrons from shells closest to the nucleus.

The ratio of the corresponding emission rate Λ_e for such a process measured with respect to the pure gamma emission Λ_γ given by Eqn (3.31) for a particular transition is referred to as the internal conversion coefficient α_T

$$\alpha_T = \frac{\Lambda_e}{\Lambda_\gamma}. \tag{3.51}$$

The total electromagnetic transition rate Λ_T is thus given by

$$\Lambda_T = \Lambda_e + \Lambda_\gamma = (1 + \alpha_T)\Lambda_\gamma \tag{3.52}$$

$$\Lambda_T(\ell; L_i \longrightarrow L_f) = \frac{8\pi(1+\alpha_T)(\ell+1)k^{2\ell+1}}{\ell\hbar\big[(2\ell+1)!!\big]^2} B(\ell; L_i \longrightarrow L_f) \tag{3.53}$$

and the corresponding electromagnetic decay width Γ_γ is

$$\begin{aligned}\Gamma_\gamma(\ell; L_i \longrightarrow L_f) &= \hbar\Lambda_T \\ &= \frac{8\pi(1+\alpha_T)(\ell+1)k^{2\ell+1}}{\ell\big[(2\ell+1)!!\big]^2} B(\ell; L_i \longrightarrow L_f).\end{aligned} \tag{3.54}$$

For the quadrupole transitions with known $B(E2)$ and $k = E_\gamma/\hbar c$, we have

$$\Gamma_\gamma(E2; L_i \longrightarrow L_f) = \frac{12\pi e^2(1+\alpha_T)}{225}\Big(\frac{E_\gamma}{\hbar c}\Big)^5 B(E2; L_i \longrightarrow L_f) \tag{3.55}$$

for the electromagnetic decay width.

3.2.7 Branching Ratio

This is defined as the ratio of a partial transition probability from a specific state to the total transition probability from that state [9]. It is a measure of the relative intensities of the competing decay modes of an unstable state.

Thus for a state involved in an alpha decay and an electromagnetic transition with corresponding decay widths Γ_α and Γ_γ, the total decay width Γ_T for the state is the sum of the partial decay widths given by

$$\Gamma_T = \Gamma_\alpha + \Gamma_\gamma, \tag{3.56}$$

and hence the branching ratios are given by

$$b_\alpha = \frac{\Gamma_\alpha}{\Gamma_\alpha + \Gamma_\gamma} \tag{3.57}$$

and

$$b_\gamma = \frac{\Gamma_\gamma}{\Gamma_\alpha + \Gamma_\gamma} \tag{3.58}$$

respectively.

Chapter 4

Model Calculations

4.1 Introduction

In the previous chapters the potential models and the observables of interest were described in detail. The goal of this chapter is to compare the results obtained for various observables using the microscopic M3Y and the phenomenological SW + SW^3 potentials. We pay particular attention to the positive parity ground state band of ^{212}Po with extension to other closed-core plus alpha cluster nuclei in order to emphasize certain observations.

4.1.1 Microscopic (M3Y) Potential Model

The microscopic M3Y effective interaction for ^{212}Po is obtained using a renormalized core-cluster interaction [32];

$$V_N(\boldsymbol{r}) = \lambda \iint \rho_c(\boldsymbol{r_1})\rho_\alpha(\boldsymbol{r_2'})g(E, |\boldsymbol{r}_{12}|)d\boldsymbol{r_1}d\boldsymbol{r_2'} \tag{4.1}$$

where λ is the renormalization factor and the density independent M3Y nucleon-nucleon interaction is given by Eqns (2.22) and (2.23)

$$g(E, |\boldsymbol{r}_{12}|) = v_{eff}(r_{12}) + v_{eff}^{ex}(r_{12}) \tag{4.2}$$

with

$$v_{eff}(r_{12}) = \Big[7999\frac{\exp(-4r_{12})}{4r_{12}} - 2134\frac{\exp(-2.5r_{12})}{2.5r_{12}}\Big] \tag{4.3}$$

and

$$v_{eff}^{ex}(r_{12}) = -276(1 - 0.005E/A_2)\delta(r_{12}). \tag{4.4}$$

The energy E corresponds to the alpha decay energy, and the cluster mass number $A_2 = 4$.

The density distributions of the ^{208}Pb core $\rho_c(\boldsymbol{r_1})$ and the alpha cluster $\rho_\alpha(\boldsymbol{r_2'})$ are respectively given by the two parameter Fermi form [32];

$$\rho_c(r_1) = \frac{\rho_o}{1 + \exp\left(\frac{r_1 - R_{Pb}}{a}\right)}, \tag{4.5}$$

and the gaussian form [53]

$$\rho_\alpha(r_2) = 0.4299 \exp(-0.7024 r'^2_2). \tag{4.6}$$

In Eqn (4.5) the core radius $R_{Pb} = 1.07 A_1^{1/3}$ fm, the diffuseness $a = 0.54$ fm, and the factor ρ_o is fixed by normalizing the density to the mass number of the core A_1 [32]. Numerical values of the M3Y nuclear potential are then generated using the computer code DFPOT [75].

The Coulomb potential takes the form of Eqn (3.7) with $Z_1 = 82$ for the lead core, $Z_2 = 2$ for the alpha cluster and the radius $R_C = 1.2 A_1^{1/3}$ [32].

Using the experimental Q-value ($E_0 = 8.985$ MeV) for the ground state decay together with the known potential the classical turning points are determined and the renormalization parameter λ optimized in an iteration procedure until Eqn (3.19) is satisfied (see Appendix B). We employ a value of $G = 18$ as suggested in the earlier works on alpha clustering in ^{212}Po [12, 67].

We obtained $\lambda = 0.53$ for the ground state decay of ^{212}Po to be compared with an acceptable range of $\lambda \sim 0.55 - 0.65$ [32]. The reduction from $\lambda = 1$ is indicative of medium effects not explicitly included in our treatment. Using Eqns (3.29) and (3.30) with a preformation factor $P = 1$ the ground state alpha decay half-life is placed at $T_{1/2} = 1.57 \times 10^{-7}$ s which compares favourably with the experimental half-life of 3×10^{-7} s [76].

The M3Y potential with $\lambda = 0.53$ is further used to determine the alpha decay energy of each member of the ground state band of ^{212}Po and the ground state Q-value is then subtracted to obtain the excitation energies. The level scheme is presented in Table (4.1).

The results show an inverted level structure in which the high spin states are more strongly bound than the lower states similar to the results obtained with a Cosh potential (Table (3.1)). This inversion is in clear disagreement with experiment. We note that the renormalization parameter λ decreases with increasing L-value in order to reproduce the level scheme correctly. Thus the M3Y potential which predicts the decay half-life to within a factor of ~ 2 fails to describe the observed spectrum of ^{212}Po.

J^π	E_{expt}(MeV)	E_{cal}(MeV)
0^+	0.000	-0.004
2^+	0.727	-0.067
4^+	1.132	-0.229
6^+	1.355	-0.508
8^+	1.476	-0.930
10^+	1.834	-1.538
12^+	2.702	-2.358
14^+	2.885	-3.437
16^+	-	-4.800
18^+	2.921	-6.477

Table 4.1: The experimental level scheme of ^{212}Po and the calculated spectrum obtained with renormalized M3Y potential ($\lambda = 0.53$) and $G = 18$.

4.1.2 Phenomenological (SW + SW^3) Potential Model

For the purpose of the present comparison with the M3Y potential we choose the following parameter set for the SW + SW^3 potential obtained in an earlier study of alpha clustering in ^{212}Po [67];

$$V_o = 214 \text{ MeV},\ a = 0.75 \text{ fm},\ x = 0.33 \text{ and } G = 18. \tag{4.7}$$

We note here that in the calculations involving the M3Y potential the geometry is fixed and the depth is treated as a parameter through λ, whereas in the SW + SW^3 calculations, the depth is fixed and the radius R is treated as a parameter. The nuclear radius R is fixed using a similar iterative procedure detailed in the preceding section with a starting value of $R = 1.2(A_1 + A_2)^{1/3}$. We obtained $R = 6.744$ fm with an alpha decay half-life 1.50×10^{-7} s for the ground state. The predicted level spectrum is presented in Table (4.2).

We observe that the SW + SW^3 potential reproduces the decay half-life of the ground state to within a factor of ~ 2, as is the case for the M3Y potential. In addition the level ordering of the band is reproduced with the observed characteristic compression of the high spin states contrary to the result obtained with the M3Y potential.

J^π	E_{expt}(MeV)	E_{cal}(MeV)
0^+	0.000	0.000
2^+	0.727	0.206
4^+	1.132	0.574
6^+	1.355	1.050
8^+	1.476	1.594
10^+	1.834	2.150
12^+	2.702	2.666
14^+	2.885	3.060
16^+	-	3.250
18^+	2.921	3.070

Table 4.2: The experimental level scheme of ^{212}Po and the calculated spectrum obtained with SW + SW^3 potential parameters of Eqn (4.7) and $R = 6.744$ fm.

4.1.3 Comparison of the Potential Models

Here we compare further the two potential models using the potentials generated in sections (4.1.1) and (4.1.2). The radial plots of both the M3Y and the SW + SW^3 potentials are presented in Figure (4.1) from which the following observations can be made.

The SW + SW^3 potentials mimics the M3Y potential in the external region of low density where the M3Y potential is likely to be most reliable, and it is this level of agreement in the Coulomb barrier region which explains why the alpha decay half-lives from the two potential models are in such a good agreement.

The difference in the two potential models is more pronounced at radial separations $r < 6$ fm. While the M3Y is more shallow and assumes a near constant value in the interior between 0 to ~ 4 fm, the phenomenological potential is deeper and more rounded. The effect of this on the spectrum can be understood by labelling the first turning points as $r_1(L)$ with $r_1(0) < r_1(2) < r_1(4) \cdots$. Thus, for example, only the 0^+ state feels the influence of the potential between $r_1(0)$ and $r_1(2)$, and the deeper the potential in this region the relatively more bound will be the 0^+ state. This is the case for the SW + SW^3 potential as opposed to the SW, Cosh and the M3Y potentials all of which show essentially the same flat shape in the internal region, and give rise to an inverted spectrum for ^{212}Po. This difference in the internal region is the critical feature as to why the SW + SW^3 reproduces the level ordering of the energy structure.

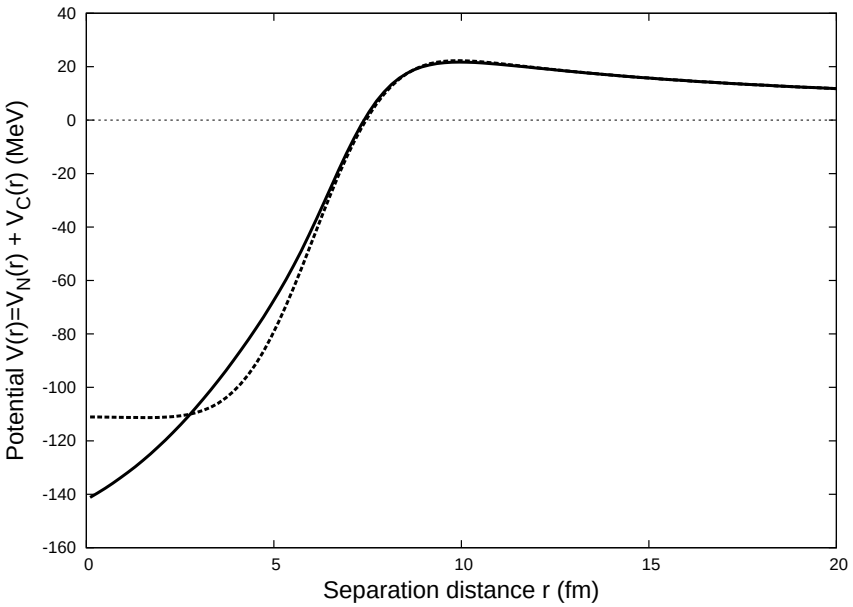

Figure 4.1: Radial plots of the Nuclear plus Coulomb potentials for the ^{208}Pb-^{4}He core-cluster system. The nuclear potentials are of the SW+SW^3 form (solid line) and the M3Y form (dashed line). See Tables (4.1) and (4.2) for details.

4.2 Optimization of the SW + SW^3 Parameter Values

Given the superior predictive power of the SW + SW^3 potential we next optimize its parameters by fitting the known spectrum of the ground state band of ^{212}Po including the most recent information on the positions of the 12^+ and 14^+ states [76].

For this purpose we elect to fit simultaneously the depth V_o, the diffuseness a, the mixing parameter x and the radius R. Rather than simply reproducing the ground state energy as done in previous calculations [12, 26, 67] (and in sections (4.1.1) and (4.1.2) of the present work), we take the more even-handed approach of including all the levels of the ground state band in the fit. We thus employ an iterative procedure with a goodness of fit parameter χ^2 determined by

$$\begin{aligned} S_{left} &= \int_{r_1}^{r_2} dr \sqrt{\frac{2\mu}{\hbar^2}[E_L - V(r)]} \\ S_{right} &= (G - L + 1)\frac{\pi}{2} \\ \chi^2 &= \sum_L (S_{left} - S_{right})^2 \end{aligned} \tag{4.8}$$

excluding the unknown 16^+ state.

We vary V_o, a, x and R in steps of 1 MeV, 0.01 fm, 0.01 and 0.001 fm respectively with the proviso that the resulting parameter set does not require a preformation factor greater than unity

J^π	E_{expt}(MeV)	E_{cal}(MeV)
0^+	0.000	(0.495)
2^+	0.727	0.659
4^+	1.132	0.948
6^+	1.355	1.318
8^+	1.476	1.730
10^+	1.834	2.145
12^+	2.702	2.519
14^+	2.885	2.805
16^+	-	2.941
18^+	2.921	2.841

Table 4.3: The experimental level scheme of ^{212}Po [76] and the calculated spectrum obtained with SW + SW^3 potential parameters of Eqn (4.10). The 0^+ ground state has been omitted from the fit.

to reproduce the alpha decay half-life of the ^{212}Po ground state. The best set of parameters is given by

$$V_o = 214 \text{ MeV},\ a = 0.66 \text{ fm},\ x = 0.30 \text{ and } R = 6.696 \text{ fm} \tag{4.9}$$

with $G = 18$ and $\chi^2 = 0.0226$. These parameter values however generate an underbound 0^+ ground state which contributes a large weight to the goodness of fit parameter χ^2. Excluding the 0^+ state from the fit gives

$$V_o = 208 \text{ MeV},\ a = 0.66 \text{ fm},\ x = 0.30 \tag{4.10}$$

with $R = 6.784$ fm and $\chi^2 = 0.0129$. The ^{212}Po spectrum obtained with our new parameter set in Eqn (4.10) is presented in Table (4.3).

The calculated spectrum is in fair agreement with experiment. It reproduces the level sequence and the compression of the high spin states. The appearance of the 16^+ state above the 18^+ provides an explanation for the isomeric character of the latter since the electromagnetic transition from the 18^+ state is strongly hindered with the decay of the state proceeding mainly through alpha emission, which is itself hindered by a large centrifugal barrier. The contribution of the centrifugal barrier (~ 36 MeV), for example, is comparable to the Coulomb barrier (~ 34 MeV)

Transition	$B(E2\downarrow)_{expt}$(W.u.)	$B(E2\downarrow)_{cal}$(W.u.)
$2^+ \longrightarrow 0^+$	-	4.2
$4^+ \longrightarrow 2^+$	-	5.7
$6^+ \longrightarrow 4^+$	3.9 ± 1.1	5.9
$8^+ \longrightarrow 6^+$	2.3 ± 0.1	5.5
$10^+ \longrightarrow 8^+$	2.2 ± 0.6	4.9
$12^+ \longrightarrow 10^+$	-	4.1
$14^+ \longrightarrow 12^+$	-	3.1

Table 4.4: The electromagnetic transition strengths of ^{212}Po in Weisskopf units (W.u.). The experimental values are taken from [67], and the calculated values are obtained with the SW + SW^3 potential parameters of Eqn (4.10).

at radial distance $r = 7$ fm. We note further that the 0^+ - 2^+ level splitting is in disagreement with the experimental result with the 0^+ ground state underbound by ~ 0.5 MeV.

The reduced transition strengths $B(E2\downarrow)$ obtained using Eqns (3.47) and (3.50) are listed in Table (4.4). The radial wave functions for each state were obtained from a numerical solution of the Schrödinger wave equation using the potential parameters of Eqn (4.10). Although our results deviate by a factor of ~ 2 from quoted values, the order (1.0 W.u.) and trend are reproduced. Table (4.5) contains the calculated electromagnetic and alpha decay widths obtained with the Eqns (3.55) and (3.29) for Γ_γ and Γ_α respectively.

The half-life $T_{1/2}$ for each state [23, 77] and the corresponding alpha branching ratios b_α can then be calculated from the results of Table (4.5) using

$$T_{1/2} = \frac{\hbar \ln 2}{\Gamma_\gamma + \Gamma_\alpha} \text{ and } b_\alpha = \frac{\Gamma_\alpha}{\Gamma_\gamma + \Gamma_\alpha}, \tag{4.11}$$

and the results are shown in Table (4.6).

The agreement between the calculated half-lives and the measured values is generally good but the branching ratios are poorly reproduced. We note however that the experimental values for the 4^+, 6^+ and 8^+ states are uncertain [77]. In particular the two quoted values for the 8^+ state differ markedly with one agreeing, within the quoted error, with the theoretical result. Hopefully further experimentation will reduce these uncertainties.

J^π	$E_{exc}(MeV)$	Total Internal Conversion (α_T)	Γ_γ(MeV)	Γ_α(MeV)
0^+	0.000	-	-	1.311×10^{-15}
2^+	0.727	0.014	5.179×10^{-11}	3.133×10^{-14}
4^+	1.132	0.055	4.026×10^{-12}	5.523×10^{-14}
6^+	1.355	0.340	2.619×10^{-13}	1.886×10^{-14}
8^+	1.476	3.400	3.645×10^{-14}	1.953×10^{-15}
10^+	1.834	0.076	1.863×10^{-12}	2.778×10^{-16}
12^+	2.702	0.0097*	1.221×10^{-10}	1.456×10^{-16}
14^+	2.885	0.650*	6.432×10^{-14}	2.319×10^{-18}
16^+	-	-	-	-
18^+	2.921	-	-	1.156×10^{-14}

Table 4.5: The gamma and alpha decay widths of ^{212}Po calculated with the SW + SW^3 potential parameter of Eqn (4.10). The total internal conversion factor (α_T) are taken from [23, 78]. The asterisks denote that theoretical estimates have been used for (α_T).

J^π	$T_{\frac{1}{2}}^{expt}$(ns)	$T_{\frac{1}{2}}^{cal}$(ns)	$b_\alpha^{expt}\%$	$b_\alpha^{cal}\%$
0^+	300	348	100	100
2^+	-	8.80×10^{-3}	0.033	0.06
4^+	-	1.11×10^{-1}	~ 27	1.34
6^+	0.76	1.63	~ 71	6.72
8^+	17.05	11.88	$\sim 42(6 \pm 1)$	5.00
10^+	0.55	0.25	-	1.50×10^{-2}
12^+	-	3.74×10^{-3}	-	1.19×10^{-4}
14^+	-	7.10	-	3.61×10^{-3}
16^+	-	-	-	-
18^+	4.5×10^{10}	4.0×10^{10}	~ 100	100

Table 4.6: Measured half-lives and branching ratios for α decay of ^{212}Po [76, 77]. The calculated values are obtained using Eqn (4.11). Note the widely differing measured values of b_α^{expt} for the 8^+ state.

J^π	E_{expt}(MeV)	E_{cal}(MeV)	$B(E2\downarrow)^{expt}$(e^{2}fm^4)	$B(E2\downarrow)^{cal}$(e^{2}fm^4)
0^+	0.000	(1.285)	-	-
2^+	1.634	2.424	65.5±3.2	44
4^+	4.248	4.679	70.9±6.5	57
6^+	8.776	7.859	64.4±9.7	47
8^+	11.951	11.691	29.1±4.2	25

Table 4.7: The energy level scheme and electromagnetic transition strengths of ^{20}Ne. The experimental values are taken from [78, 79] and the calculated values obtained as discussed in the sections (4.3) and (4.3.1). The 0^+ ground state has been omitted from the fit.

4.3 Application To Other Nuclei

We next calculate the properties of the ground state bands of light nuclei considered as good candidates of an alpha plus closed core nuclei to further test the potential of Eqn (4.10). Particularly we would like to confirm whether the underbinding of the 0^+ ground state obtained in the ^{212}Po calculation remains a feature of these calculations and whether it can be rectified using a common prescription.

We thus extend the calculation to ^{20}Ne and ^{44}Ti using the global quantum numbers $G = 8$ and $G = 12$ respectively. The potential parameters V_o, a and x are fixed at the values given in Eqn (4.10) while the corresponding nuclear radius R is separately fitted by minimizing the χ^2 in Eqn (4.8). In each case the 0^+ state is excluded.

4.3.1 Neon-20 ($^{20}\mathrm{Ne} = {}^{16}\mathrm{O} + \alpha$)

The properties of the ground state band of ^{20}Ne have been widely studied [6, 12, 13, 79] and an alpha cluster structure is generally accepted. We obtained a radius $R = 3.368$ fm with a goodness of fit parameter $\chi^2 = 0.071$. The calculated spectrum in Table (4.7) reproduces fairly well the approximately rotational structure of the observed values. As for ^{212}Po the 0^+ is strongly underbound. The relative values of the calculated electromagnetic strengths are in excellent agreement with experiment and the absolute values are a factor of ~ 1.3 too small indicating a need for a small effectice charge.

J^π	E_{expt}(MeV)	E_{cal}(MeV)	$B(E2\downarrow)^{expt}$(e^{2}fm^4)	$B(E2\downarrow)^{cal}$(e^{2}fm^4)
0^+	0.000	(1.056)	-	-
2^+	1.083	1.609	120±37	103
4^+	2.454	2.654	277±55	139
6^+	4.015	4.054	157±28	135
8^+	6.509	5.657	> 14	112
10^+	7.671	7.246	138±28	78
12^+	8.039	8.508	< 60	38

Table 4.8: The energy level scheme and electromagnetic transition strengths of ^{44}Ti. The experimental values are taken from [12, 78] and the calculated values obtained as discussed in the sections (4.3) and (4.3.2). The 0^+ ground state has been omitted from the fit.

4.3.2 Titanium-44 ($^{44}\mathrm{Ti} = {}^{40}\mathrm{Ca} + \alpha$)

For this nucleus we obtained a radius $R = 4.694$ fm with $\chi^2 = 0.054$. The trend of the experimental level spacings is well reproduced by our calculation for ^{44}Ti (see table (4.8)). The level schemes do not have the $L(L+1)$ rotational character and the characteristic compression of the excitation energies above the 6^+ state is fairly well reproduced. As for ^{212}Po and ^{20}Ne the 0^+ state is again underbound. The calculated $B(E2\downarrow)$ values shown in Table (4.8) are in good agreement with the observed results, although the measured values are characterised by large uncertainties.

We thus find that for ^{212}Po, ^{20}Ne, and ^{44}Ti we obtain reasonably good agreement between theoretical and observed energy spectra. A common feature of the three nuclei studied is the underbinding of the 0^+ ground state. This feature was also noted in [12] where it was associated with the nature of the SW + SW^3 potential close to the origin.

We find that $B(E2)$ values are quite well reproduced, particularly as we have had no recourse to an effective charge.

4.4 The Underbinding of the 0^+ State

Here we investigate the relatively poor results for the 0^+ ground state energy in ^{212}Po, ^{44}Ti, and ^{20}Ne, possibly indicating a shortcoming of the SW + SW^3 potential form near the origin. In this preliminary investigation we introduce an additional term

$$V_{corr}(r) = \begin{cases} -V_\delta & \text{for } r \leq r_0 \\ \\ 0 & \text{otherwise.} \end{cases} \tag{4.12}$$

Labelling the internal turning points $r_1(L)$ with $r_1(0) < r_1(2) < r_1(4) \cdots$, we observe that for small enough r_0 the additional interaction affects only the 0^+ state. Consequent to some parameter search in a two dimensional mesh we put

$$V_\delta = 20 \text{ MeV and } r_0 = 0.35 \text{ fm.} \tag{4.13}$$

Thus using a total interaction

$$V(r) = V_N(r) + V_C(r) + V_L(r) + V_{corr}(r), \tag{4.14}$$

a new search for the SW+SW^3 parameters excluding the 0^+ ground state, using Eqns (4.12) and (4.13), produces no new parameter sets for each nucleus. This indicates that only the 0^+ is affected by $V_{corr}(r)$. Tables (4.9), (4.10) and (4.11) contain the resulting spectra for ^{212}Po, ^{20}Ne and ^{44}Ti respectively.

In each of the nuclei the 0^+ state is lowered by about 0.5 MeV with a consequent improvement in the fits to the spectra. A similar improvement is found for ^{218}Rn (see Chapter 6). Although these preliminary results are not conclusive further studies employing a relatively more attractive potential near the origin than the SW + SW^3 form may prove worthwhile.

J^π	E_{expt}(MeV)	E_{cal}(MeV)
0^+	0.000	(0.010)
2^+	0.727	0.659
4^+	1.132	0.948
6^+	1.355	1.318
8^+	1.476	1.730
10^+	1.834	2.145
12^+	2.702	2.519
14^+	2.885	2.805
16^+	-	2.941
18^+	2.921	2.841

Table 4.9: The energy level scheme of ^{212}Po obtained as per Table (4.3) with additional short range interaction of Eqns (4.12) and (4.13).

J^π	E_{expt}(MeV)	E_{cal}(MeV)
0^+	0.000	(0.771)
2^+	1.634	2.424
4^+	4.248	4.679
6^+	8.776	7.859
8^+	11.951	11.691

Table 4.10: The energy level scheme of ^{20}Ne, obtained as per Table (4.7), including the additional short range interaction of Eqns (4.12) and (4.13).

J^π	E_{expt}(MeV)	E_{cal}(MeV)
0^+	0.000	(0.530)
2^+	1.083	1.609
4^+	2.454	2.654
6^+	4.015	4.054
8^+	6.509	5.657
10^+	7.671	7.246
12^+	8.039	8.508

Table 4.11: The energy level scheme of ^{44}Ti, obtained as per Table (4.8), including the additional short range interaction of Eqns (4.12) and (4.13).

Chapter 5

Negative Parity Bands in Po-212

5.1 Introduction

Low-lying negative parity bands with bandheads at excitation energies of $\sim$ 1 MeV occur in several nuclei in the actinide region and are usually associated with nuclear octupole deformation. In the collective model they have been described as octupole vibrational bands resulting from the coupling of an octupole phonon to the positive parity states of the ground state band [80]. Recently, stable octupole deformation of some nuclei has also been shown to arise as a result of strong octupole coupling between valence orbitals of opposite parities [81]. In this chapter we present a cluster model interpretation of these bands, and apply the formalism to ^{212}Po.

5.2 The Odd-G Formalism

In the cluster model the $L^\pi = 0^+, 2^+, 4^+ \cdots G^+$ positive parity ground state bands of even-even nuclei are generated using an even value of the global quantum number G. Increasing G by one then results in a negative parity band with $L^\pi = 1^-, 3^-, 5^- \cdots (G+1)^-$. This odd-$G$ model gives satisfactory results for the negative parity bands of ^{20}Ne and ^{44}Ti using the same core-cluster potential that described the positive parity ground state bands of these nuclei [12].

In heavy nuclei however it is found that the odd-G model described above generates a negative parity band at too high an excitation energy [82]. For example Table (5.1) compares the calculated excitation energies of the negative parity band of ^{212}Po with the available experimental information [76] using the potential parameter set of Eqn (4.10) and $G = 19$. It is possible to rectify the mismatch by using a parity dependent potential [37] but no other justification for such a potential and for its additional set of potential parameter values has so far been found. A further drawback of the odd-G model is that it produces a single $K^\pi = 0^-$ band, whereas

J^π	E_{expt}(MeV)	E_{cal}(MeV)
1^-	-	6.715
3^-	-	6.999
5^-	-	7.432
7^-	-	7.971
9^-	-	8.566
(11^-)	2.411	9.164
(13^-)	2.772	9.703

Table 5.1: The observed negative parity levels of ^{212}Po [76] compared with theoretical estimates for an odd-G ($G = 19$) band.

$K^\pi = 1^-, 2^-$ and possibly 3^- bands have been observed at similar energies as the $K^\pi = 0^-$ band in heavy nuclei [80, 83].

5.3 The Excited Core Formalism

An alternative approach is to assume that the core may be found in either its $I^\pi = 0^+$ ground state, or in an excited $I^\pi = 3^-$ state with excitation energy $E(3^-)$. Coupling these states to the even G core-cluster relative motion yields the positive parity ground state band $L^\pi = 0^+, 2^+, 4^+ \cdots G^+$ when $I^\pi = 0^+$, whereas a rich spectrum of negative parity states which has given a good representation of the experimental situation in a number of heavy nuclei results when $I^\pi = 3^-$ [44]. We present below the formalism for generating these negative parity states which involves a standard diagonalization of an effective Hamiltonian given by

$$\hat{H}(\mathbf{r}, \boldsymbol{\xi}) = \hat{H}_o(\mathbf{r}) + \hat{H}_{int}(\boldsymbol{\xi}) + V_T(\mathbf{r}, \boldsymbol{\xi}). \tag{5.1}$$

The Schrödinger wave equation (SWE) for the core-cluster system is thus of the form

$$\left[\hat{H}_o(\mathbf{r}) + \hat{H}_{int}(\boldsymbol{\xi}) + V_T(\mathbf{r}, \boldsymbol{\xi}) - E\right]\Psi_{JM}(\mathbf{r}, \boldsymbol{\xi}) = 0 \tag{5.2}$$

where $\hat{H}_o(\mathbf{r})$ is the relative motion Hamiltonian defined in section (3.2), $\hat{H}_{int}(\boldsymbol{\xi})$ is the core Hamiltonian with internal coordinate $\boldsymbol{\xi}$, and $V_T(\mathbf{r}, \boldsymbol{\xi})$ is an additional non-central interaction which couples the relative and internal motions. The core-cluster separation vector is given by $\mathbf{r}$. The total wavefunction $\Psi_{JM}(\mathbf{r}, \boldsymbol{\xi})$ may be expanded in terms of basis states of $\hat{H}_o(\mathbf{r}) + \hat{H}_{int}(\boldsymbol{\xi})$

as

$$\Psi_{JM}(\mathbf{r},\boldsymbol{\xi}) = \sum_{L'} \alpha^J_{L'} \frac{\psi_{L'}(r)}{r} \Phi^{JM}_{L'I}(\hat{\mathbf{r}},\boldsymbol{\xi}). \tag{5.3}$$

In Eqn (5.3) $\alpha^J_{L'}$ is an expansion coefficient, $\frac{\psi_{L'}(r)}{r}$ is the radial component of the wavefunction of the core and cluster relative motion, and $\Phi^{JM}_{L'I}(\hat{\mathbf{r}},\boldsymbol{\xi})$ is the wavefunction obtained from a coupling of the angular part of the relative motion wavefunction to the core eigenfunction $\phi_{I\lambda}(\boldsymbol{\xi})$ so that

$$\Phi^{JM}_{L'I}(\hat{\mathbf{r}},\boldsymbol{\xi}) = \sum_{\lambda,\mu} \big\langle L'\mu I\lambda \big| JM \big\rangle Y_{L'\mu}(\hat{\mathbf{r}}) \phi_{I\lambda}(\boldsymbol{\xi}). \tag{5.4}$$

In Eqn (5.4) L' is the relative angular momentum, $I = 3$ is the core angular momentum, and μ and λ are the projections of L' and I on the z-axis.

Using the expansion of Eqn (5.3) in Eqn (5.2) we have

$$\sum_{L'} \Big[E_{L'} + E(3^-) + V_T(\mathbf{r},\boldsymbol{\xi}) - E \Big] \alpha^J_{L'} \frac{\psi_{L'}(r)}{r} \Phi^{JM}_{L'I}(\hat{\mathbf{r}},\boldsymbol{\xi}) = 0 \tag{5.5}$$

where we have used

$$\hat{H}_o \bigg(\sum_{L'} \alpha^J_{L'} \frac{\psi_{L'}(r)}{r} \Phi^{JM}_{L'I}(\hat{\mathbf{r}},\boldsymbol{\xi}) \bigg) = \sum_{L'} E_{L'} \alpha^J_{L'} \frac{\psi_{L'}(r)}{r} \Phi^{JM}_{L'I}(\hat{\mathbf{r}},\boldsymbol{\xi}) \tag{5.6}$$

for the relative motion as in Eqn (3.5), and

$$\hat{H}_{int} \bigg(\sum_{L'} \alpha^J_{L'} \frac{\psi_{L'}(r)}{r} \Phi^{JM}_{L'I}(\hat{\mathbf{r}},\boldsymbol{\xi}) \bigg) = \sum_{L'} E(3^-) \alpha^J_{L'} \frac{\psi_{L'}(r)}{r} \Phi^{JM}_{L'I}(\hat{\mathbf{r}},\boldsymbol{\xi}) \tag{5.7}$$

for the internal Hamiltonian. We assume that $\hat{H}_o(\mathbf{r})$ remains the same irrespective of the core state I so that the $E_{L'}$ correspond to the energies of states in the positive parity ground state band and these energies may be taken from the experimental spectrum [44].

Premultiplying Eqn (5.5) by $\frac{\psi_L(r)}{r} \Phi^{JM}_{LI}(\hat{\mathbf{r}},\boldsymbol{\xi})$ and integrating over all the coordinates gives

$$\Big[E_L + E(3^-) - E \Big] \alpha^J_L + \sum_{L'} \bigg\langle \frac{\psi_L(r)}{r} \Phi^{JM}_{LI}(\hat{\mathbf{r}},\boldsymbol{\xi}) \bigg| V_T(\mathbf{r},\boldsymbol{\xi}) \bigg| \frac{\psi_{L'}(r)}{r} \Phi^{JM}_{L'I}(\hat{\mathbf{r}},\boldsymbol{\xi}) \bigg\rangle \alpha^J_{L'} = 0 \tag{5.8}$$

which may be rewritten as

$$\Big[E_L + E(3^-) - E \Big] \alpha^J_L + \sum_{L'} V^J_{LL'} \alpha^J_{L'} = 0 \tag{5.9}$$

with

$$V^J_{LL'} = \left\langle \frac{\psi_L(r)}{r}\Phi^{JM}_{LI}(\hat{\mathbf{r}},\boldsymbol{\xi})\middle| V_T(\mathbf{r},\boldsymbol{\xi})\middle|\frac{\psi_{L'}(r)}{r}\Phi^{JM}_{L'I}(\hat{\mathbf{r}},\boldsymbol{\xi})\right\rangle \tag{5.10}$$

which may be written in the condensed form

$$V^J_{LL'} = \big\langle LI;JM\big|V_T(\mathbf{r},\boldsymbol{\xi})\big|L'I;JM\big\rangle \tag{5.11}$$

where L and L' take on even values only and $I = 3$.
We assume a quadrupole-quadrupole form for the non-central interaction [44, 84] given by

$$V_T(\mathbf{r},\boldsymbol{\xi}) = \varepsilon g(r) Y_2(\hat{\mathbf{r}})\cdot Y_2(\hat{\boldsymbol{\xi}}) \tag{5.12}$$

where ε is the strength of the interaction and the function $g(r)$ is related to the first derivative of the nuclear potential $V_N(r)$ of Eqn (3.6) [84] by

$$g(r) = -r\frac{\partial V_N(r)}{\partial r}. \tag{5.13}$$

As in earlier work [44, 84] we also assume that a single orientation $\hat{\boldsymbol{\xi}}$ is all that is required to describe the internal motion of the core (we shall however see below that this assumption may be substantially relaxed).

Using Eqn (5.12) in the coupling matrix of Eqn (5.11) gives

$$\begin{aligned} V^J_{LL'} &= \big\langle LI;JM\big|V_T(\mathbf{r},\hat{\boldsymbol{\xi}})\big|L'I;JM\big\rangle \\ &= \big\langle LI;JM\big|\varepsilon g(r)Y_2(\hat{\mathbf{r}})\cdot Y_2(\hat{\boldsymbol{\xi}})\big|L'I;JM\big\rangle \\ &= \varepsilon g_{LL'}\big\langle \Phi^{JM}_{LI}(\hat{\mathbf{r}},\hat{\boldsymbol{\xi}})\big|Y_2(\hat{\mathbf{r}})\cdot Y_2(\hat{\boldsymbol{\xi}})\big|\Phi^{JM}_{L'I}(\hat{\mathbf{r}},\hat{\boldsymbol{\xi}})\big\rangle \end{aligned} \tag{5.14}$$

where

$$g_{LL'} = \int \frac{\psi_L(r)}{r} g(r) \frac{\psi_{L'}(r)}{r} r^2 dr \tag{5.15}$$

is the radial integral involving only the radial coordinate r of the relative motion.

The matrix element involving the angular components in Eqn (5.14) is a particular case of the general form $\langle Y_L I; JM | Y_k(\hat{\mathbf{r}}) \cdot Y_k(\hat{\boldsymbol{\xi}}) | Y_{L'} I'; J'M' \rangle$ which may be evaluated [74] as follows

$$\begin{aligned}\langle Y_L I; JM | Y_k(\hat{\mathbf{r}}) \cdot Y_k(\hat{\boldsymbol{\xi}}) | Y_{L'} I'; J'M' \rangle &= \langle Y_L I; J || Y_k(\hat{\mathbf{r}}) \cdot Y_k(\hat{\boldsymbol{\xi}}) || Y_{L'} I'; J' \rangle \delta_{JJ'} \delta_{MM'} \\ &= (-1)^{J-L-I'} \hat{L} \hat{I} W(LL'II'; kJ) \langle Y_L || Y_k(\hat{\mathbf{r}}) || Y_{L'} \rangle \\ &\quad \times \langle I || Y_k(\hat{\boldsymbol{\xi}}) || I' \rangle \delta_{JJ'} \delta_{MM'} \end{aligned} \tag{5.16}$$

where we have used $\hat{N} = \sqrt{2N+1}$. The first reduced matrix element involving the spherical harmonics may be evaluated to give [74];

$$\langle Y_L || Y_k(\hat{\mathbf{r}}) || Y_{L'} \rangle = \frac{(-1)^{L'}}{\sqrt{4\pi}} \hat{L}' \langle L0L'0 | k0 \rangle. \tag{5.17}$$

Given the assumptions about the nature of the internal state [44, 84], a similar evaluation of the second reduced matrix element in Eqn (5.16) yields

$$\langle I || Y_k(\hat{\boldsymbol{\xi}}) || I' \rangle = \frac{(-1)^{I'}}{\sqrt{4\pi}} \hat{I}' \langle I0I'0 | k0 \rangle. \tag{5.18}$$

Inserting Eqns (5.17) and (5.18) in Eqn (5.16) gives

$$\begin{aligned}\langle Y_L I; JM | Y_k(\hat{\mathbf{r}}) \cdot Y_k(\hat{\boldsymbol{\xi}}) | Y_{L'} I'; J'M' \rangle &= (-1)^{J-L+L'} \frac{1}{4\pi} \hat{L} \hat{I} \hat{L}' \hat{I}' W(LL'II'; kJ) \langle L0L'0 | k0 \rangle \\ &\quad \times \langle I0I'0 | k0 \rangle \delta_{JJ'} \delta_{MM'}. \end{aligned} \tag{5.19}$$

By identifying $k = 2, I = I' = 3$ we thus find for Eqn (5.14) that

$$\begin{aligned} V^J_{LL'} &= \varepsilon g_{LL'} \langle Y_L 3; JM | Y_2(\hat{\mathbf{r}}) \cdot Y_2(\hat{\boldsymbol{\xi}}) | Y_{L'} 3; JM \rangle \\ &= (-1)^{J-L+L'} \varepsilon g_{LL'} \frac{7}{4\pi} \hat{L} \hat{L}' W(LL'33; 2J) \langle L0L'0 | 20 \rangle \langle 3030 | 20 \rangle \end{aligned} \tag{5.20}$$

for the coupling matrix elements consistent with [84, 85].

We note that a more general form of a quadrupole-quadrupole interaction to that of Eqn (5.12) is given by

$$V_T(\mathbf{r}, \boldsymbol{\xi}) = \varepsilon g(r) Y_2(\hat{\mathbf{r}}) \cdot T_2(\boldsymbol{\xi}) \tag{5.21}$$

where $T_2(\boldsymbol{\xi})$ is a rank-2 tensor in the internal coordinates $\boldsymbol{\xi}$ required to describe the internal motion of the core. The matrix element in Eqn (5.18) would then take the form $\langle I || T_2(\boldsymbol{\xi}) || I' \rangle$ and

merely results in a different value of the (fitted) strength ε to that obtained when $T_k(\boldsymbol{\xi}) = Y_k(\hat{\boldsymbol{\xi}})$.

By rewriting Eqn (5.9) as

$$\sum_{L'} \Big[\big[E_{L'} + E(3^-)\big]\delta_{LL'} + V^J_{LL'} \Big] \alpha^J_{L'} = E\alpha^J_L \tag{5.22}$$

one can then construct a diagonalizable Hamiltonian matrix (H^J) with the matrix elements given by $H^J_{LL'} = \big[E_{L'} + E(3^-)\big]\delta_{LL'} + V^J_{LL'}$.

As an illustration the Hamiltonian matrix $H^{J=3}$ for a state $J^\pi = 3^-$ takes the form

$$H^{J=3} = \begin{bmatrix} E_0{+}E(3^-){+}V^3_{00} & V^3_{02} & V^3_{04} & V^3_{06} \\ V^3_{20} & E_2{+}E(3^-){+}V^3_{22} & V^3_{24} & V^3_{26} \\ V^3_{40} & V^3_{42} & E_4{+}E(3^-){+}V^3_{44} & V^3_{46} \\ V^3_{60} & V^3_{62} & V^3_{64} & E_6{+}E(3^-){+}V^3_{66} \end{bmatrix}$$

with L and L' given by $L = 0(2)6$ and $L' = 0(2)6$ respectively. The column matrix for the expansion coefficients

$$\begin{bmatrix} \alpha^3_0 & \alpha^3_2 & \alpha^3_4 & \alpha^3_6 \end{bmatrix}^T \tag{5.23}$$

gives the eigenvector corresponding to a particular eigenvalue. It therefore means that each of the resulting eigenvalues $E_i (i = 1, 2, 3, 4)$ with eigenstates $\Psi^i_{JM}(\mathbf{r}, \boldsymbol{\xi})$ corresponds to a different admixture of the basis states $\frac{\psi_{L'}(r)}{r}\Phi^{JM}_{L'I}(\hat{\mathbf{r}}, \boldsymbol{\xi})$. The different set of the expansion coefficients for each E_i may then be labelled as $(\alpha^3_0(i), \alpha^3_2(i), \alpha^3_4(i), \alpha^3_6(i))$.

Dropping the index i for clarity we may recast the state wavefunction in Eqn (5.3) into the more compact form

$$\big|JM\big\rangle = \sum_{L'=|J-I'|}^{J+I'} \alpha^J_{L'} \big|L'I'; JM\big\rangle \tag{5.24}$$

with $I' = 3$ and L' even.

5.3.1 Negative Parity Spectrum with a Constant $g_{LL'}$

Here we calculate the spectrum of ^{212}Po based on the assumption that the radial integral $g_{LL'}$ of Eqn (5.15) are very similar for all L, L' [44] and may be approximated by a constant value g such that

$$V^J_{LL'} = (-1)^{J+L-L'} 7\beta \hat{L}\hat{L}' W(LL'33; 2J)\langle L0L'0|20\rangle\langle 3030|20\rangle \tag{5.25}$$

where

$$\beta = \frac{\varepsilon g}{4\pi} \tag{5.26}$$

is treated as a constant parameter [44]. This assumption holds if the radial wavefunctions for the ground state band are all very similar (see Eqn (5.15)). Using values of the core energy $E(3^-)$ and the strength β given by [44, 85];

$$E(3^-) = 1.12 \text{ MeV and } \beta = -0.3512 \text{ MeV} \tag{5.27}$$

we then calculate the negative parity states of ^{212}Po. Here we have used the experimental excitation energies of the positive parity ground state band for the E_L given in Table (4.9) together with the theoretical estimate ($E_{16} = 2.941$ MeV) for the unknown excitation energy of the 16^+ state. We note that the value of $E(3^-)$ in Eqn (5.27) is infact an effective value when compared to the observed value of the 3^- states.

Table (5.2) lists the calculated excitation energies arranged in an increasing order for each state J^π, and grouped into different K^π bands using the rotational model notation. The classification into K-bands is arbitrary because ^{212}Po is not a good rotor. Nevertheless there is no ambiguity in, for example, classifying the lowest odd-J negative parity states of interest as a '$K^\pi = 0^-$' band. A physical reason for this terminology can also be found in the limit where the $J^\pi = 0^+, 2^+, 4^+ \cdots$ members of the positive parity ground state band are all degenerate [86] (see Appendix C1.1).

Thus identifying the '$K^\pi = 0^-$' band in Table (5.2) as the lowest odd-J negative parity states of ^{212}Po we find good agreement with the very limited experimental information in Table (5.3). In particular the whole band is considerably lowered in energy and more compressed in comparison with the result from the odd-G formalism in Table (5.1).

J^π	E(MeV) $K^\pi = 0^-$	E(MeV) $K^\pi = 1^-$	E(MeV) $K^\pi = 2^-$	E(MeV) $K^\pi = 3^-$
1^-	1.436	1.841	-	-
2^-	-	1.669	2.076 -	-
3^-	0.956	1.901	2.120	2.476
4^-	-	1.825	2.254	2.724
5^-	1.548	2.128	2.365	2.889
6^-	-	2.091	2.454	3.006
7^-	1.902	2.368	2.665	3.101
8^-	-	2.278	2.759	3.216
9^-	2.106	2.669	3.248	3.583
10^-	-	2.492	3.230	3.879
11^-	2.261	3.113	3.620	4.143
12^-	-	2.916	3.750	4.343
13^-	2.645	3.605	3.873	4.478

Table 5.2: The negative parity states of ^{212}Po obtained from the diagonalized Hamiltonian matrices using the experimental values E_{expt} from Table (4.1) and parameter values of Eqn (5.27).

J^π	E_{expt}(MeV)	E_{cal}(MeV)
1^-	-	1.436
3^-	-	0.956
5^-	-	1.548
7^-	-	1.903
9^-	-	2.107
(11^-)	2.411	2.261
(13^-)	2.772	2.645

Table 5.3: A comparison of the measured and calculated lowest odd-J negative parity states of ^{212}Po. The calculated results are obtained with the experimental values E_{expt} from Table (4.1) and the parameter values of Eqn (5.27).

The inversion of the $J^\pi = 1^-$ and $J^\pi = 3^-$ states may be explained by the fact that, in weak coupling, the lowest energy $J^\pi = 1^-$ state is formed by coupling the $I^\pi = 3^-$ core state to an orbital angular momentum $L^\pi = 2^+$ state, whereas the lowest $J^\pi = 3^-$ state is formed by coupling the $I^\pi = 3^-$ state to a lower energy $L^\pi = 0^+$ state.

In the following sections we give a detailed account of a recent derivation [87] of expressions for the electric quadrupole and electric dipole transition strengths involving the states of the '$K^\pi = 0^-$' band. We consider transition operators involving only the (collective) relative motion coordinates, as otherwise we would require an explicit model of the internal motion.

5.3.2 Quadrupole Transition Strength

The in-band quadrupole transition strength for the '$K^\pi = 0^-$' band described in section (5.3.1) may be obtained from a generalisation of Eqn (3.46) to one involving states J_i and J_f each of which has two components involving different sets of coordinates. In general we have

$$\begin{aligned} B(Ek; J_i \longrightarrow J_f) &= \left(\frac{\hat{J}_f}{\hat{J}_i}\right)^2 \left|\left\langle J_f \middle|\middle| \hat{O}_k \middle|\middle| J_i \right\rangle\right|^2 \\ &= \left|A(Ek; J_i \longrightarrow J_f)\right|^2 \end{aligned} \tag{5.28}$$

where J_i and J_f are the initial and final states, and $\hat{O}_k$ is an electric operator of order k. Supposing that J_i is formed from the coupling of two states of angular momenta (j_1, j_2), and J_f is similarly formed from (j_1', j_2') respectively, and if the operator $\hat{O}_k$ acts only on one set of

coordinates so that $\hat{O}_k = \hat{O}_k(1)$ then $A(Ek)$ may be simplified as

$$\begin{aligned} A(Ek; J_i \longrightarrow J_f) &= \left(\frac{\hat{J}_f}{\hat{J}_i}\right)\langle j_1', j_2'; J_f||\hat{O}_k(1)||j_1, j_2; J_i\rangle \\ &= \left(\frac{\hat{J}_f}{\hat{J}_i}\right)(-1)^{J_f+j_1-k-j_2'}\hat{J}_i\hat{j}_1'W(j_1'j_1J_fJ_i; kj_2')\langle j_1'||\hat{O}_k(1)||j_1\rangle\delta(j_2'j_2) \\ &= (-1)^{J_f+j_1-k-j_2'}\hat{J}_f\hat{j}_1'W(j_1'j_1J_fJ_i; kj_2')\langle j_1'||\hat{O}_k(1)||j_1\rangle\delta(j_2'j_2) \end{aligned} \tag{5.29}$$

where we have used standard results for the evaluation of the reduced matrix element [74].

Adapting Eqn (5.29) for quadrupole transitions between two single component negative parity states (see Eqn (5.3)) with $j_1' = L_f$, $j_2' = 3$; $j_1 = L_i$, $j_2 = 3$, and $k = 2$ gives

$$A(E2; J_i \longrightarrow J_f) = (-1)^{J_f+L_i-5}\hat{J}_f\hat{L}_fW(L_fL_iJ_fJ_i; 23)\langle L_f||\hat{O}_2(1)||L_i\rangle. \tag{5.30}$$

The reduced matrix element involving the orbital angular momenta L_i and L_f in Eqn (5.30) can be obtained from Eqns (3.46) and (3.47) so that

$$\begin{aligned} A(E2; J_i \longrightarrow J_f) &= (-1)^{J_f+L_i-5}\hat{J}_f\hat{L}_fW(L_fL_iJ_fJ_i; 23)\frac{\hat{L}_i}{\hat{L}_f}\beta_2\sqrt{\frac{5}{4\pi}} \\ &\quad\times\langle L_i020|L_f0\rangle\langle\psi_{L_f}|r^2|\psi_{L_i}\rangle \\ &= (-1)^{J_f+L_i-1}\sqrt{\frac{5}{4\pi}}\beta_2\hat{J}_f\hat{L}_iW(L_fL_iJ_fJ_i; 23) \\ &\quad\times\langle L_i020|L_f0\rangle\langle\psi_{L_f}|r^2|\psi_{L_i}\rangle. \end{aligned} \tag{5.31}$$

In the derivation of Eqn (5.31) we have used single component state vectors corresponding to single values of L_i and L_f, that is

$$|J_iM_i\rangle = |L_iI_i; J_iM_i\rangle \tag{5.32}$$

and

$$|J_fM_f\rangle = |L_fI_f; J_fM_f\rangle \tag{5.33}$$

for the initial and final states in Eqn (5.28).

Transition	$B(E2\downarrow)_{cal}$(W.u.)
$1^- \longrightarrow 3^-$	7.6
$5^- \longrightarrow 3^-$	5.3
$7^- \longrightarrow 5^-$	6.3
$9^- \longrightarrow 7^-$	5.9
$11^- \longrightarrow 9^-$	5.4
$13^- \longrightarrow 11^-$	4.8

Table 5.4: The electromagnetic transition strengths for the lowest odd-J negative parity states of ^{212}Po obtained with Eqns (5.34) and (5.35).

In general a negative parity state $\big|JM\big\rangle$ will be given by Eqn (5.24) so that Eqn (5.31) becomes

$$A(E2; J_i \longrightarrow J_f) = \sum_{L_i L_f \text{even}} (-1)^{J_f+L_i-1}\sqrt{\frac{5}{4\pi}}\beta_2 \hat{J}_f \hat{L}_i W(L_f L_i J_f J_i; 23) \times\big\langle L_i 020\big|L_f 0\big\rangle\big\langle\psi_{L_f}\big|r^2\big|\psi_{L_i}\big\rangle\alpha_{L_i}^{J_i}\alpha_{L_f}^{J_f} \tag{5.34}$$

with an electric quadrupole transition strength

$$B(E2; J_i \longrightarrow J_f) = \big|A(E2; J_i \longrightarrow J_f)\big|^2. \tag{5.35}$$

The results for $B(E2\downarrow)$ are presented in Table (5.4). The matrix elements of the squared radial separation are calculated with wavefunctions obtained from the numerical solutions of the SWE with potential parameters of Eqn (4.10). The expansion coefficients are those obtained with the parameter values of Eqn (5.27). The order of magnitude of the calculated $B(E2\downarrow)$ values is similar to those of the positive parity states.

5.3.3 Dipole Transition Strength

The dipole transition strength between a single component negative parity state (see Eqn (5.3)) and a member of the positive parity ground state band is given by

$$B(E1; J_i \longrightarrow J_f) = \left(\frac{\hat{J}_f}{\hat{J}_i}\right)^2 \big|\big\langle j_1', j_2'; J_f\big|\big|\hat{O}_1(1)\big|\big|j_1, j_2; J_i\big\rangle\big|^2 \tag{5.36}$$

with $j_1 = L_i$, $j_2 = 3$; $j_1' = L_f$, $j_2' = 0$. Thus using Eqn (5.29) we have

$$A(E1; J_i \longrightarrow J_f) = (-)^{J_f+L_i-1}\hat{J}_f\hat{L}_f W(L_f L_i J_f J_i; 10)\big\langle L_f\big|\big|\hat{O}_1(1)\big|\big|L_i\big\rangle\delta(j_2' j_2) \tag{5.37}$$

which vanishes since $\hat{O}_1(1)$ cannot connect the two positive parity orbital angular momenta L_i and L_f, and also $j_2' \neq j_2$.

On the other hand however, the $E1$ transitions from the odd-G negative parity states to the even-G positive parity states with both having the core in its $I^\pi = 0^+$ state are not negligible. For example we obtain a value of 0.241 e^2fm^2 (0.105 W.u.) for the dipole strength $B(E1 : 1^- \longrightarrow 0^+)$ using Eqn (3.41). Thus in order to explain the possible cross-band $E1$ transitions in ^{212}Po we consider the possibility of mixing the two negative parity bands earlier discussed in sections (5.2) and (5.3).

5.4 Coefficient of Admixture

Supposing an odd-G state obtained from the relative motion of the spinless core-cluster system is given by (see Eqn (3.4))

$$|L^- M^-\rangle = \frac{\psi_{L^-}(r)}{r} Y_{L^-,M^-}(\theta,\phi)\phi_{I=0,\lambda=0}(\boldsymbol{\xi}) \tag{5.38}$$

where $L^- = 1^-\ (2)\ (G+1)^-$ and $\phi_{I=0,\lambda=0}(\boldsymbol{\xi})$ is the normalised spinless internal wavefunction of the ground state of the core. The admixture of such a state into another state $|JM\rangle$ of the same angular momentum $J = L^-$, $M = M^-$ described by Eqn (5.24) can be approximated in first order perturbation theory by [88];

$$|\varphi\rangle = |JM\rangle + \frac{\langle L^- M^-|V|JM\rangle}{E_J - \epsilon_{L^-}}|L^- M^-\rangle \tag{5.39}$$

where $|\varphi\rangle$ represents the resultant state, E_J and ϵ_{L^-} are the unperturbed energies as shown in Figure (5.1), and V is the perturbation potential which mixes the state $|L^- M^-\rangle$ with energy ϵ_{L^-} into $|JM\rangle$ with energy E_J.

Assuming that V is a weak octupole-octupole interaction given, in analogy with Eqn (5.12), by

$$V(\boldsymbol{r},\boldsymbol{\xi}) = \gamma h(r) Y_3(\hat{\boldsymbol{r}}) \cdot Y_3(\hat{\boldsymbol{\xi}}) \tag{5.40}$$

the mixing coefficient is then given by

$$\begin{aligned} C_{L^-} &= \frac{\langle L^- M^-|V|JM\rangle}{E_J - \epsilon_{L^-}} \\ &= \frac{\langle L^- M^-|\gamma h(r) Y_3(\hat{\boldsymbol{r}}) \cdot Y_3(\hat{\boldsymbol{\xi}})|JM\rangle}{E_J - \epsilon_{L^-}} \end{aligned} \tag{5.41}$$

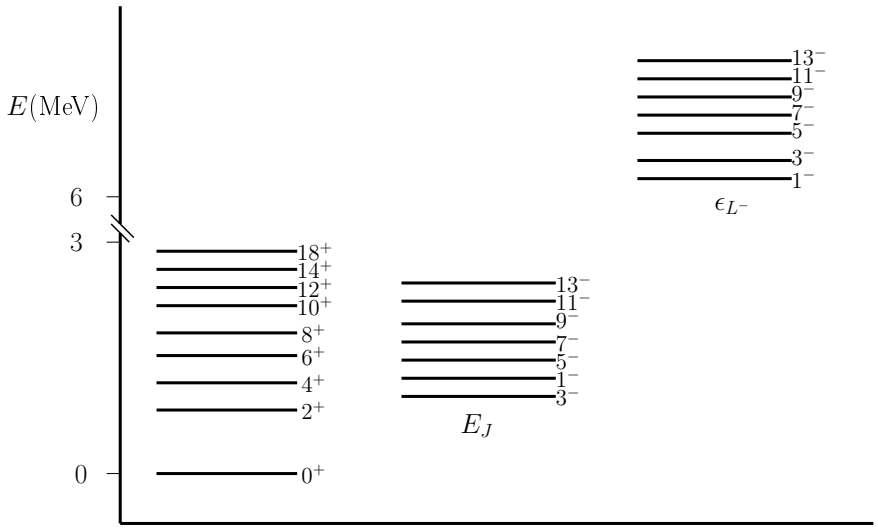

Figure 5.1: A schematic diagram of ^{212}Po showing the relative position of the negative parity bands with respect to the positive parity ground state band. The negative parity spectra correspond to the excited-core and the odd-G formalisms with excitation energies E_J and ϵ_{L^-} respectively.

$$
\begin{aligned}
C_{L^-} &= \frac{\langle L^- || \gamma h(r) Y_3(\hat{\boldsymbol{r}}) \cdot Y_3(\hat{\boldsymbol{\xi}}) || J \rangle \delta_{L^- J} \delta_{M^- M}}{E_J - \epsilon_{L^-}} \\
&= \sum_{L'=|J-I'|_{\text{even}}}^{J+I'} \alpha^J_{L'} \frac{\langle L^-, I=0; L^- || \gamma h(r) Y_3(\hat{\boldsymbol{r}}) \cdot Y_3(\hat{\boldsymbol{\xi}}) || L', I'=3; J \rangle \delta_{L^- J}}{E_J - \epsilon_{L^-}} \\
&= \frac{1}{\Delta E} \sum_{L'=|J-I'|_{\text{even}}}^{J+I'} \alpha^J_{L'} \langle L^-, I=0; L^- || \gamma h(r) Y_3(\hat{\boldsymbol{r}}) \cdot Y_3(\hat{\boldsymbol{\xi}}) | L', I'=3; J \rangle \delta_{L^- J} \qquad (5.42)
\end{aligned}
$$

where we have used Eqn (5.24) and $\Delta E = E_J - \epsilon_{L^-}$. A comparison of the calculated energies in Tables (5.1) and (5.3) shows that ΔE is roughly constant at 6 MeV.

Simplifying the matrix element of Eqn (5.42) using Eqn (5.19) with $L = L^-, I = 0$; $L' = L', I' = 3$ and $k = 3$ gives

$$
\begin{aligned}
C_{L^-} = \frac{1}{\Delta E} \sum_{L'=|J-3|_{\text{even}}}^{J+3} & \gamma h_{L^- L'} \alpha^J_{L'} (-)^{J-L^-+L'} \frac{1}{4\pi} \hat{L^-} \hat{L'} \hat{3} W(L^- L' 03; 3J) \\
& \times \langle L^- 0 L' 0 | 30 \rangle \langle 0030 | 30 \rangle \delta_{L^- J} \qquad (5.43)
\end{aligned}
$$

where the radial integral

$$
h_{L^- L'} = \int \psi_{L^-}(r) h(r) \psi_{L'}(r) dr. \qquad (5.44)
$$

Since the angular momenta of the states are equal ($J = L^-$) and L' is even we thus have

$$C_{L^-} = \frac{\gamma}{4\pi\Delta E} \sum_{L'=|J-3|_{\rm even}}^{J+3} \alpha^J_{L'} h_{L^-L'} \hat{L^-} \hat{L'} \hat{3} W(L^- L' 03; 3L^-) \langle L^- 0 L' 0 | 30 \rangle \langle 0030 | 30 \rangle$$

$$= \frac{\gamma h}{4\pi\Delta E} \sum_{L'=|J-3|_{\rm even}}^{J+3} \alpha^J_{L'} \hat{L'} \langle L^- 0 L' 0 | 30 \rangle \tag{5.45}$$

where we have taken all the radial integrals to be the same $h_{L^-L'} = h$ consistent with the assumption of section (5.3.1).

In summary the admixture of a $G+1$ state into a member of the '$K^\pi = 0^-$' band of angular momentum J can be rewritten as

$$C_J = \frac{\gamma h}{4\pi\Delta E} \sum_{L'=|J-3|_{\rm even}}^{J+3} \alpha^J_{L'} \hat{L'} \langle J 0 L' 0 | 30 \rangle \tag{5.46}$$

where $\dfrac{\gamma h}{4\pi\Delta E}$ can be considered as a parameter.

5.4.1 Dipole Transition Strength With Mixed State

In the previous section we have described the mixing of the negative parity states of angular momentum $1^-, 3^-, 5^- \cdots$ belonging to the $G+1$ band with the negative parity states of the '$K^\pi = 0^-$' band arising from the core excitation. An initial mixed negative parity state of angular momentum J_i can then decay through an electric dipole transition to a final positive parity state of angular momentum J_f belonging to the positive parity ground state band. The decay is essentially that from a pure $G+1$ state to a pure G state, moderated by the mixing coefficient $C^2_{J_i}$ of Eqn (5.46). The dipole transition strength for the decay can thus be obtained using Eqns (3.46) and (3.47) to give

$$B(E1; J_i \longrightarrow J_f) = \frac{3}{4\pi} C^2_{J_i} \beta^2_1 \left| \langle J_i 010 | J_f 0 \rangle \right|^2 \left| \langle \psi_{J_f} | r | \psi_{J_i} \rangle \right|^2 \tag{5.47}$$

A simple result, independent of the various parameter values introduced above, follows from considering the two dipole transitions from an initial mixed negative parity state of odd angular momentum $J^\pi_i = 1^-, 3^-, 5^- \cdots$ to the two possible final states in the positive parity ground state band of even angular momentum $J^\pi_f = J^\pi_i \pm 1$.

J^π	1^-	3^-	5^-	7^-	9^-	11^-	13^-
Ratio ($E1:E1$)	0.94	0.85	0.77	0.69	0.60	0.52	0.43

Table 5.5: Theoretical estimates of the $E1$ ratios for members of the negative parity band of ^{212}Po.

For $J_f = J_i + 1$

$$B(E1; J_i \longrightarrow J_i + 1) = \frac{3}{4\pi} C_{J_i}^2 \beta_1^2 \left|\langle J_i 010 | J_i + 1, 0\rangle\right|^2 \left|\langle \psi_{J_i+1} | r | \psi_{J_i}\rangle\right|^2 \tag{5.48}$$

and similarly for $J_f = J_i - 1$

$$B(E1; J_i \longrightarrow J_i - 1) = \frac{3}{4\pi} C_{J_i}^2 \beta_1^2 \left|\langle J_i 010 | J_i - 1, 0\rangle\right|^2 \left|\langle \psi_{J_i-1} | r | \psi_{J_i}\rangle\right|^2. \tag{5.49}$$

Thus the ratio of Eqns (5.48) and (5.49) may be cast into the form

$$\left[\frac{B(E1; J_i \longrightarrow J_i + 1)}{B(E1; J_i \longrightarrow J_i - 1)}\right]^{1/2} \left|\frac{\langle J_i 010 | J_i - 1, 0\rangle}{\langle J_i 010 | J_i + 1, 0\rangle}\right| = \frac{\langle \psi_{J_i+1} | r | \psi_{J_i}\rangle}{\langle \psi_{J_i-1} | r | \psi_{J_i}\rangle} \tag{5.50}$$

where we have used the fact that C_{J_i} is independent of the final state in the positive parity ground state band. Thus using the assumption that the radial wavefunctions $|\psi_{J_i+1}\rangle \approx |\psi_{J_i-1}\rangle$, we find

$$\left[\frac{B(E1; J_i \longrightarrow J_i + 1)}{B(E1; J_i \longrightarrow J_i - 1)}\right]^{1/2} \left|\frac{\langle J_i 010 | J_i - 1, 0\rangle}{\langle J_i 010 | J_i + 1, 0\rangle}\right| \approx 1. \tag{5.51}$$

Eqn (5.51) also follows from the standard rotational model [87, 89], and a comparison with experiment for ^{238}U [83] is illustrated in Figure (5.2). For the present application of the cluster model to ^{212}Po Table (5.5) shows the $E1$ ratios evaluated for each of the mixed negative parity states of ^{212}Po using the radial wavefunctions generated with the potential of Eqn (4.10).

Agreement with the estimate of Eqn (5.51) is reasonable for low spin states but becomes progressively poorer as the spin increases. It would be interesting to have experimental data with which to compare the estimates of Table (5.5).

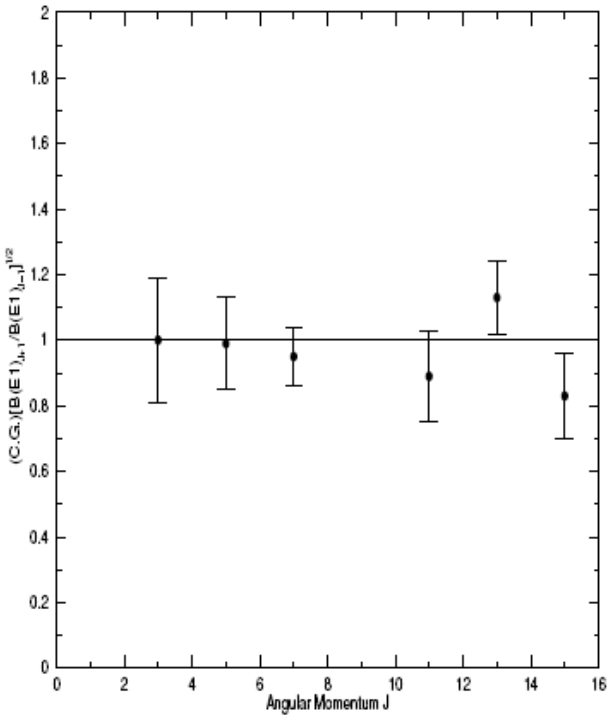

Figure 5.2: The experimental values of the $E1$ transition ratios in ^{238}U [83] compared with the value predicted by Eqn (5.51) [87].

.

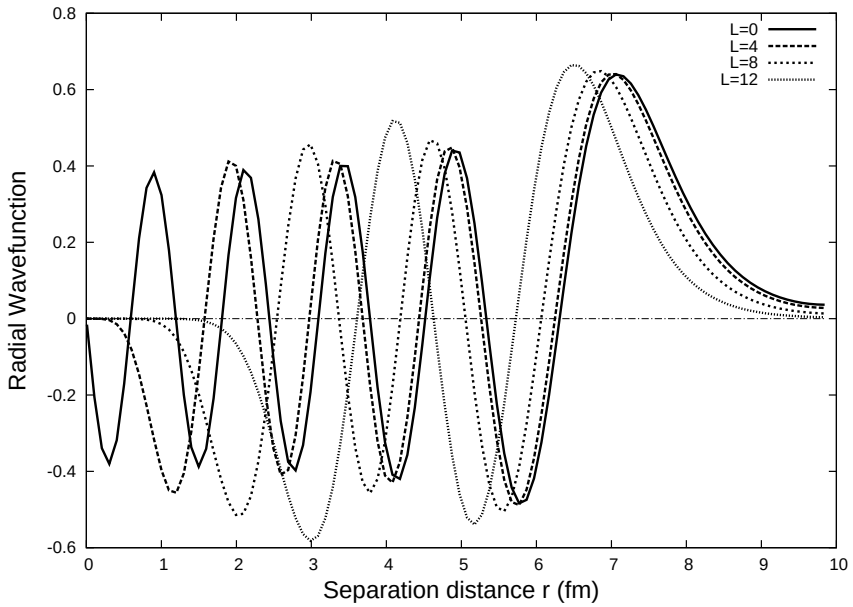

Figure 5.3: The radial wavefunctions of ^{208}Pb - ^{4}He relative motion corresponding to the positive parity states $L = 0(4)12$ of ^{212}Po.

.

5.5 Negative Parity Spectrum with Calculated $g_{LL'}$

The cornerstone for the calculations in section (5.3.1) is the assumed similarity of the radial wavefunctions within the ground state band. However, for the alpha cluster states in ^{212}Po, this assumption is questionable. For example the wavefunctions are most similar in the surface region for low angular momemtum states $L^{\pi} = 0^{+}, 2^{+}, 4^{+}, 6^{+}$ and 8^{+} (see Figure (5.3)) which implies that the results in Table (5.3) should be most reliable for the low spin negative parity states.

Figure (5.3) further illustrates the decrease in the similarity of the radial wavefunctions with increasing orbital angular momentum L. Thus the radial integrals $g_{LL'}$ are expected to be different for different combinations of L and L', and hence the need to calculate the radial integral explicitly for ^{208}Pb - ^{4}He model of ^{212}Po.

Using Eqn (5.13) for the function $g(r)$ and the nuclear potential parameters of Eqn (4.10) we calculated the radial integrals from Eqn (5.15). By starting with the values in Eqn (5.27), the core excitation energy $E(3^{-})$ and the effective strength ε of the non-central potential were then adjusted to reproduce the absolute experimental energy of the 11^{-} and 13^{-} states.
Table (5.6) lists the resulting level spectrum obtained with $E(3^{-}) = 1.03$ MeV, $\varepsilon = +0.0096$, and the calculated integrals $g_{LL'}$ given in Appendix C1.2.

J^π	E_{expt}(MeV)	E_{cal}(MeV)
1^-	-	1.628
3^-	-	1.009
5^-	-	1.684
7^-	-	2.070
9^-	-	2.282
(11^-)	2.411	2.411
(13^-)	2.772	2.772

Table 5.6: The negative parity states of ^{212}Po obtained with evaluated radial integrals, effective strength parameter $\varepsilon = +0.0096$ and excitation energy $E(3^-) = 1.03$ MeV.

Transition	$B(E2\downarrow)_{cal}$(W.u.)
$1^- \longrightarrow 3^-$	5.5
$5^- \longrightarrow 3^-$	4.7
$7^- \longrightarrow 5^-$	6.3
$9^- \longrightarrow 7^-$	6.0
$11^- \longrightarrow 9^-$	5.5
$13^- \longrightarrow 11^-$	4.9

Table 5.7: The electromagnetic transition strengths for the odd-J negative parity states of ^{212}Po obtained with Eqn (5.35) and the expansion coefficients correponding to evaluated $g_{LL'}$. The effective strength parameter $\varepsilon = +0.0096$ and excitation energy $E(3^-) = 1.03$ MeV.

Table (5.7) shows the quadrupole transition strengths obtained with $g_{LL'}$ explicitly determined. The good agreement with the results presented in Table (5.4) imply that these results are not strongly affected by the differences in the $g_{LL'}$ values presented in Table (C 3) of the Appendix C1.2.

Chapter 6

Cluster Model of Radon-218

6.1 Introduction

In chapter 4 a ^{208}Pb plus alpha cluster model successfully reproduced a number of properties of the positive parity yrast band of ^{212}Po. There is however little experimental data on the low-lying negative parity states of this nucleus. In this chapter we extend our calculations in a novel analysis of ^{218}Rn modelled as ^{208}Pb core plus a ^{10}Be cluster. The available experimental information on both low-lying positive and negative parity states of ^{218}Rn provides us with an opportunity to further test the binary cluster formalism described in the previous chapters.

6.2 Positive Parity Band

6.2.1 Phenomenological SW + SW^3 Potential Model

The level structure and the alpha decay half-lives of the $J^\pi = 0^+$ ground state and of the $J^\pi = 18^+$ isomeric state suggest $G = 18$ for the positive parity yrast band of ^{212}Po [67] as assumed in the previous chapters. For ^{218}Rn no equivalent arguments can be made and the only guidance for a value of G comes from the Wildermuth condition. In an oscillator model, protons and neutrons outside a ^{208}Pb core must have at least five and six quanta respectively. The ^{10}Be nucleus in its ground state has a configuration $(0s)^4$ $(0p)^6$ and thus requires 6 quanta for its construction (see section (3.2.2)). The least number of quanta corresponding to the relative motion of the ^{208}Pb - ^{10}Be system is then given by

$$G = (6 \times 6) + (4 \times 5) - 6 = 50 \tag{6.1}$$

J^π	E_{expt}(MeV)	E_{cal}(MeV)
0^+	0.000	(0.536)
2^+	0.324	0.630
4^+	0.653	0.794
6^+	1.014	1.024
8^+	1.393	1.309
10^+	1.775	1.643
12^+	2.169	2.018
14^+	2.577	2.431
16^+	3.002	2.873
18^+	3.438	3.339
20^+	3.859	3.823
22^+	4.287	4.316
24^+	4.725	4.813
26^+	5.168	5.305

Table 6.1: A comparison of the experimental and the calculated spectra of ^{218}Rn. The potential parameters are given in Eqn (6.2). The 0^+ state was not included in the potential optimization procedure.

which corresponds exactly with Buck *et al* scaling $G = 5A_2$ for nuclei in the actinide region [90]. We thus proceed with $G = 50$ for the ^{208}Pb - ^{10}Be relative motion in this study. We also employ the procedure described in section (4.2) for ^{212}Po to generate the SW + SW^3 potential strength V_o and the radius R. Using a diffuseness a and a mixing parameter x fixed at the values obtained for ^{212}Po in Eqn (4.10) we obtain a best fit potential given by

$$V_o = 536 \text{ MeV}, \ a = 0.66 \text{ fm}, \ x = 0.30 \tag{6.2}$$

with $R = 6.843$ fm and $\chi^2 = 0.0148$. We note from the corresponding potential parameter values of Eqn (4.10) for alpha clustering in ^{212}Po that the ratio of the potential strengths $V_o(^{10}\text{Be})/V_o(^4\text{He}) = 2.58$. This is close to the value 2.50 expected from the Buck *et al* prescription $V_o = v_o A_2$, where v_o is a constant ~ 55 and A_2 is the cluster mass number [37, 91].

Table (6.1) compares the calculated level scheme with experiment. The spacing of the calculated energy levels agrees fairly well with experiment. The main drawback is the underbinding

J^π	E_{expt}(MeV)	E_{cal}(MeV)
0^+	0.000	(0.063)
2^+	0.324	0.224
4^+	0.653	0.612
6^+	1.014	1.024
8^+	1.393	1.309
10^+	1.775	1.643
12^+	2.169	2.018
14^+	2.577	2.431
16^+	3.002	2.873
18^+	3.438	3.339
20^+	3.859	3.823
22^+	4.287	4.316
24^+	4.725	4.813
26^+	5.168	5.305

Table 6.2: A comparison of the measured and the calculated spectra of ^{218}Rn obtained using the potential parameter values of Eqn (6.2) and the short range interaction defined by Eqn (4.13).

of the $J^\pi = 0^+$ state indicative of a shortcoming of the SW + SW^3 potential for low spin states discussed in chapter 4. Further investigation using the additional short range interaction with the parameter values of Eqn (4.13) gives a considerable improvement as shown in Table (6.2). The results in Tables (6.1) and (6.2) thus reinforce the conclusion in section (4.4) regarding the potential depth near the origin.

Table (6.3) lists the quadrupole transition strengths B($E2; L_i^+ \longrightarrow L_f^+$) for the positive parity ground state band of ^{218}Rn obtained using Eqns (3.47) and (3.50). The values are approximately a factor of four larger than those obtained for the ^{212}Po ground band, as is expected from the doubling of the ^{10}Be cluster charge compared to that of ^{4}He.

The half-life for the exotic decay $^{218}\text{Rn} \rightarrow {}^{208}\text{Pb} + {}^{10}\text{Be}$ has also been calculated using the parameter set of Eqn (6.2) with radius $R = 6.851$ fm fitted to the ground state decay energy $Q = 14.36$ MeV.

Transition	$B(E2\downarrow)_{cal}$(W.u.)
$2^+ \longrightarrow 0^+$	17.8
$4^+ \longrightarrow 2^+$	25.2
$6^+ \longrightarrow 4^+$	27.5
$8^+ \longrightarrow 6^+$	28.4
$10^+ \longrightarrow 8^+$	28.5
$12^+ \longrightarrow 10^+$	28.3
$14^+ \longrightarrow 12^+$	27.8
$16^+ \longrightarrow 14^+$	27.0
$18^+ \longrightarrow 16^+$	26.1
$20^+ \longrightarrow 18^+$	25.0
$22^+ \longrightarrow 20^+$	23.8
$24^+ \longrightarrow 22^+$	22.5
$26^+ \longrightarrow 24^+$	21.1

Table 6.3: The electromagnetic transition strengths for the positive parity states of ^{218}Rn obtained using the potential parameter values of Eqn (6.2). The measured transition strength B($E2; 2^+ \longrightarrow 0^+) > 23$ W.u. [78].

For the purpose of comparison with earlier work on exotic decay [91] the calculations were repeated with a different potential parameter set given by

$$V_o = 55.7A_2 \text{ MeV},\ a = 0.75 \text{ fm},\ x = 0.36 \tag{6.3}$$

where the cluster mass $A_2 = 10$ and the radius $R = 6.672$ fm is obtained from a fit to the ground state ^{10}Be decay energy.

The theoretical estimates of the $^{218}\text{Rn} \rightarrow {}^{208}\text{Pb} + {}^{10}\text{Be}$ exotic decay half-life using Eqns (6.2) and (6.3) are $2.18 \times 10^{+22}$ s and $5.77 \times 10^{+21}$ s respectively. Since the potential of Eqn (6.3) generates good fits to all the known exotic decay half-lives [91], we conclude that this potential (and hence that of Eqn (6.2)) is likely to provide a reasonable estimate of the half-life for the ^{10}Be decay of ^{218}Rn.

6.2.2 Microscopic M3Y Potential Model

The M3Y interaction takes the general form

$$V_N(\boldsymbol{r}) = \lambda \iint \rho_c(\boldsymbol{r_1})\rho_{Be}(\boldsymbol{r_2'})g(E, |\boldsymbol{r}_{12}|)d\boldsymbol{r_1}d\boldsymbol{r_2'} \tag{6.4}$$

with $g(E, |\boldsymbol{r}_{12}|)$ given by Eqns (4.2), (4.3), and (4.4), the energy $E = 14.36$ MeV and the cluster mass number $A_2 = 10$. The ^{208}Pb core density $\rho_c(\boldsymbol{r_1})$ is evaluated as in Eqn (4.5) of the ^{212}Po calculations. The ^{10}Be density $\rho_{Be}(\boldsymbol{r_2'})$ is similarly calculated using the two-parameter Fermi function

$$\rho_{Be}(r_2') = \frac{\rho_o}{1 + \exp\left(\dfrac{r_2' - R_{Be}}{a}\right)} \tag{6.5}$$

with radius $R_{Be} = 1.07A^{1/3}$ fm and diffuseness $a = 0.52$ fm [92]. The Coulomb interaction parameters remain unchanged from those used for ^{212}Po calculations except that the cluster charge is replaced with $Z_2 = 4$.

For $G = 50$ the fitted M3Y renormalization parameter $\lambda = 0.57$ agrees with the expected range $\lambda \sim 0.55 - 0.65$ [32]. Table (6.4) compares the predicted level scheme of ^{218}Rn with experiment. The calculated level ordering using the M3Y interaction agrees with experiment contrary to the result obtained for the alpha cluster states of ^{212}Po in Table (4.1). In general however the calculated energy levels are too strongly compressed. This is especially obvious for the low spin states and shows the need for further improvement of the microscopic potential.

J^π	E_{expt}(MeV)	E_{cal}(MeV)
0^+	0.000	-0.014
2^+	0.324	0.025
4^+	0.653	0.102
6^+	1.014	0.221
8^+	1.393	0.381
10^+	1.775	0.584
12^+	2.169	0.829
14^+	2.577	1.117
16^+	3.002	1.446
18^+	3.438	1.816
20^+	3.859	2.229
22^+	4.287	2.683
24^+	4.725	3.179
26^+	5.168	3.717

Table 6.4: The experimental and the calculated positive parity energy levels of ^{218}Rn. The theoretical energy levels are obtained using M3Y potential with $\lambda = 0.57$.

The ground state exotic decay half-life $T_{1/2} = 2.71 \times 10^{+19}$ s obtained with this potential is three orders of magnitude smaller than the half-lives obtained with the phenomenological potentials. The difference can be traced to the smaller Coulomb barrier width found for the M3Y potential in comparison with that found for the SW + SW^3 potential form, as illustrated in Figure (6.1).

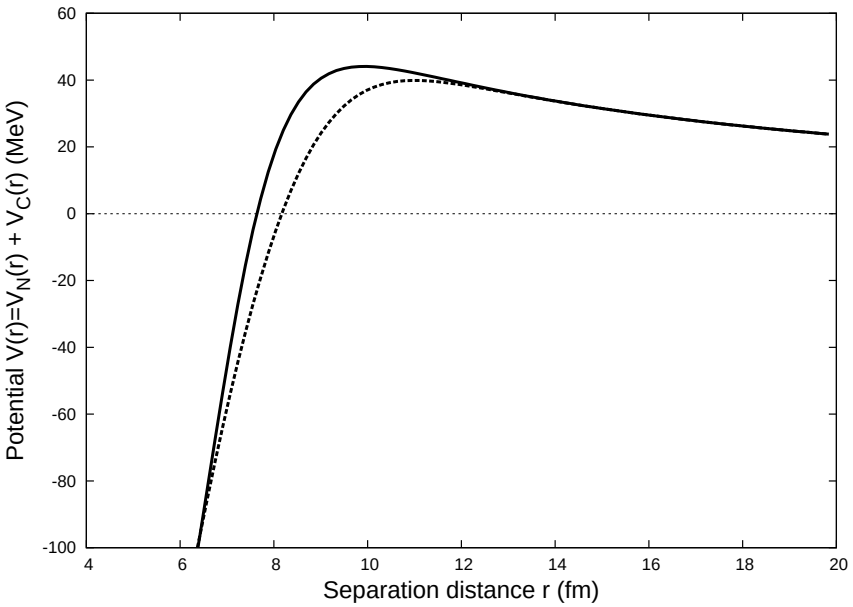

Figure 6.1: Radial plots of the potentials showing the Coulomb barrier region for the ^{208}Pb+^{10}Be core-cluster system. The nuclear potentials are of the SW+SW^3 form (solid line) and the M3Y form (dashed line).

6.3 Negative Parity Bands of ^{218}Rn

The experimental situation for the spin and parity of the lowest two negative parity states seen in ^{218}Rn is that both have been tentatively assigned $J^\pi = 3^-$ [93]. However the 0.797 MeV state decays to the $J^\pi = 2^+$ and $J^\pi = 4^+$ members of the positive parity ground state band, whereas the 0.840 MeV decays to the $J^\pi = 0^+$ and $J^\pi = 2^+$ members of the band. It is therefore possible that the observed states have $J^\pi = 3^-$ and $J^\pi = 1^-$ respectively, and have thus been labelled in Tables (6.5) and (6.6).

6.3.1 Odd-G Formalism

Table (6.5) gives the excitation energies of the negative parity states obtained with the odd-G formalism. We have used the parameter set of Eqn (6.2) with G increased by one unit to $G = 51$. The observed level spacing are fairly well reproduced but as in the case for ^{212}Po the calculated band is, again, shifted by ~ 6.0 MeV above the experimental data [80].

J^π	E_{expt}(MeV)	E_{cal}(MeV)
(3^-)	0.797	7.013
(1^-)	0.840	6.877
5^-	1.026	7.226
7^-	1.328	7.506
9^-	1.694	7.846
11^-	2.071	8.239
13^-	2.458	8.680
15^-	2.853	9.162
17^-	3.265	9.678
19^-	3.683	10.220

Table 6.5: A comparison of the measured and the calculated (odd-G) negative parity bands of ^{218}Rn. The calculated results are obtained with the potential parameter values of Eqn (6.2) and the experimental results are from [80].

6.3.2 Excited Core Formalism

As shown by a comparison of Figure (6.2) with Figure (5.3) the assumption of a common radial wavefunction for all states of the positive parity ground state band is better justified for the ^{208}Pb + ^{10}Be system than the ^{208}Pb + ^{4}He system. In calculating the negative parity states of ^{218}Rn we therefore use a constant radial integral $g_{LL'} = g$ and parameter values given by

$$E(3^-) = 1.12 \text{ MeV and } \beta = -0.3512 \text{ MeV} \tag{6.6}$$

for the core excitation energy $E(3^-)$ and the strength β as in section (5.3.1). Table (6.6) compares the calculated excitation energies of the '$K^\pi = 0^-$' band with measured values. The results are a clear improvement on those obtained with the odd-G formalism. This is further illustrated in Figure (6.3) where we have plotted the energy spacings as a function of the spin for the measured and the calculated negative parity bands. The inversion of the $J^\pi = 1^-$ and $J^\pi = 3^-$ states in Table (6.6) can be understood, as was done for ^{212}Po in section (5.3.1), by considering the lowest unperturbed configurations for these states. These are obtained by coupling the $I^\pi = 3^-$ excited core to the 2^+ state in the case of the $J^\pi = 1^-$ state, and to the lower energy 0^+ state for that of the $J^\pi = 3^-$ state.

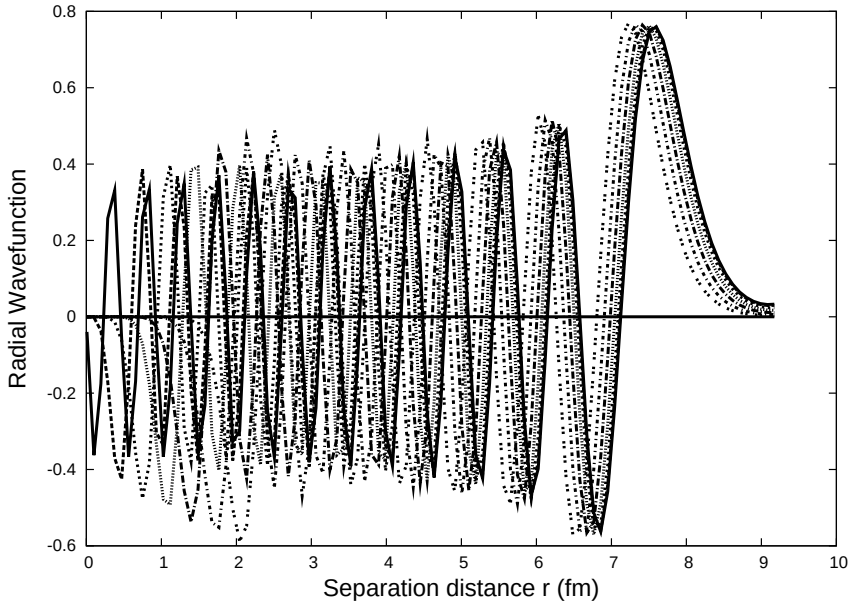

Figure 6.2: The radial wavefunctions of ^{208}Pb - ^{10}Be relative motion corresponding to the positive parity states $L = 0(4)24$ of ^{218}Rn.

J^π	E_{expt}(MeV)	E_{cal}(MeV)
(3^-)	0.797	0.872
(1^-)	0.840	1.031
5^-	1.026	1.135
7^-	1.328	1.450
9^-	1.694	1.804
11^-	2.071	2.178
13^-	2.458	2.557
15^-	2.853	2.950
17^-	3.265	3.357
19^-	3.683	3.782

Table 6.6: A comparison of the measured and the calculated '$K^\pi = 0^-$' negative parity states of ^{218}Rn. The calculated results are obtained with the experimental values E_{expt} from Table (6.1) and the parameter values of Eqn (6.6).

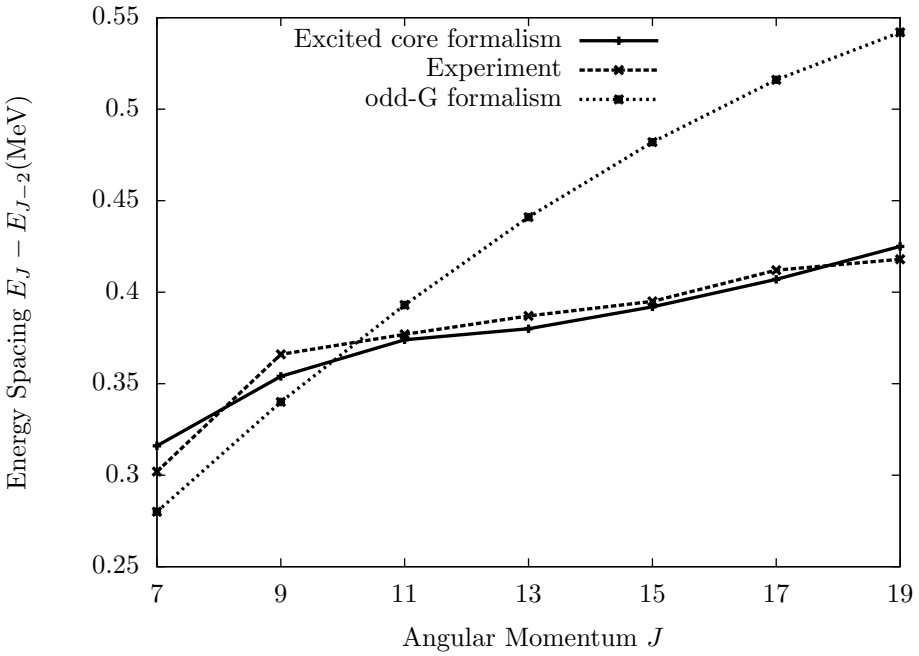

Figure 6.3: A comparison of the experimental negative parity energy spacing ($E_J - E_{J-2}$) (long dashed line) of ^{218}Rn with theoretical estimates of the odd-G (short dashed line) and the excited core formalisms (solid line). The 1^-, $3^-$and 5^- states are excluded because of the possible inversion (see Tables (6.5) and (6.6)).

Further investigation of the heavier actinide nuclei shows [85] that the splitting between the inverted $J^\pi = 1^-$and 3^- states decreases and eventually disappears with decreasing $0^+ - 2^+$ splitting. Table (6.7) contains the results for all the negative parity bands '$K^\pi = 0^-, 1^-, 2^-$ and 3^-'. These bands have been assigned in the same manner as in Table (5.2) for ^{212}Po (see Appendix C1.1).

Quadrupole Transition Strengths

Here we calculate the in-band quadrupole transition strengths $B(E2\downarrow)$ for the negative parity band '$K^\pi = 0^-$' in Table (6.6) using the formalism of section (5.3.2) where

$$B(E2; J_i \longrightarrow J_f) = \left|A(E2; J_i \longrightarrow J_f)\right|^2 \tag{6.7}$$

with $A(E2; J_i \longrightarrow J_f)$ given by

$$A(E2; J_i \longrightarrow J_f) = \sum_{L_i L_f \text{even}} (-)^{J_f + L_i - 1} \sqrt{\frac{5}{4\pi}} \beta_2 \hat{J}_f \hat{L}_i W(L_f L_i J_f J_i; 23) \times \left\langle L_i 020 \middle| L_f 0 \right\rangle \left\langle \psi_{L_f} \middle| r^2 \middle| \psi_{L_i} \right\rangle \alpha_{L_i}^{J_i} \alpha_{L_f}^{J_f}. \tag{6.8}$$

In Eqn (6.8) the positive parity ground state band radial wavefunctions were obtained from a solution of the radial Schrödinger wave equation (SWE) with potential parameters of Eqn (6.2), and the expansion coefficients α_L^J from the calculation of the negative parity states in Table (6.6). The magnitude and trend of the reduced transition strengths listed in Table (6.8) are almost the same as in the positive parity band.

Dipole Transition Ratio

We evaluate the ratio of the two electromagnetic $E1$ transitions from an odd-J negative parity mixed state to the positive parity ground state band using Eqn (5.50), that is

$$\left[\frac{B(E1; J_i \longrightarrow J_i + 1)}{B(E1; J_i \longrightarrow J_i - 1)}\right]^{1/2} \left|\frac{\langle J_i 010 | J_i - 1, 0\rangle}{\langle J_i 010 | J_i + 1, 0\rangle}\right| = \frac{\left\langle \psi_{J_i+1} \middle| r \middle| \psi_{J_i} \right\rangle}{\left\langle \psi_{J_i-1} \middle| r \middle| \psi_{J_i} \right\rangle}. \tag{6.9}$$

In Eqn (6.9) the radial wavefunctions have been calculated by solving the radial SWE with potential parameter values from Eqn (6.2). The results are listed in Table (6.9). No data exists with which to compare these results, but if available would prove a strong test of a number of exotic cluster ideas.

J^π	E(MeV) $K^\pi = 0^-$	E(MeV) $K^\pi = 1^-$	E(MeV) $K^\pi = 2^-$	E(MeV) $K^\pi = 3^-$
1^-	1.031	1.364	-	-
2^-	-	1.249	1.613 -	-
3^-	0.872	1.516	1.780	2.063
4^-	-	1.399	1.888	2.293
5^-	1.135	1.829	2.156	2.503
6^-	-	1.694	2.247	2.707
7^-	1.450	2.177	2.535	2.912
8^-	-	2.039	2.621	3.112
9^-	1.804	2.546	2.926	3.314
10^-	-	2.406	3.006	3.514
11^-	2.178	2.926	3.329	3.721
12^-	-	2.782	3.404	3.924
13^-	2.557	3.320	3.747	4.138
14^-	-	3.174	3.816	4.347
15^-	2.950	3.730	4.177	4.568
16^-	-	3.581	4.242	4.783
17^-	3.357	4.154	4.600	5.004
18^-	-	4.005	4.668	5.215
19^-	3.782	4.581	5.029	5.434

Table 6.7: The negative parity states of ^{218}Rn obtained with the experimental values E_{expt} from Table (6.1) and the parameter values of Eqn (6.6).

Transition	$B(E2\downarrow)_{cal}$(W.u.)
$1^- \longrightarrow 3^-$	38.5
$5^- \longrightarrow 3^-$	24.3
$7^- \longrightarrow 5^-$	27.3
$9^- \longrightarrow 7^-$	28.5
$11^- \longrightarrow 9^-$	28.9
$13^- \longrightarrow 11^-$	28.9
$15^- \longrightarrow 13^-$	28.5
$17^- \longrightarrow 15^-$	27.9
$19^- \longrightarrow 17^-$	27.1

Table 6.8: The in-band transition strengths for the '$K^\pi = 0^-$' negative parity states of ^{218}Rn.

J^π	1^-	3^-	5^-	7^-	9^-	11^-	13^-	15^-	17^-	19^-
Ratio ($E1:E1$)	0.98	0.95	0.91	0.88	0.85	0.82	0.79	0.76	0.73	0.69

Table 6.9: Theoretical estimates of the $E1$ ratios for members of the negative parity band of ^{218}Rn.

Chapter 7

Conclusion

The SW+SW^3 phenomenological potential model and the widely used microscopic M3Y potential have been used to study the structure of the heavy even-even nuclei ^{212}Po and ^{218}Rn treated as a doubly closed ^{208}Pb core plus a cluster formed by the strongly correlated motion of the valence nucleons. Preliminary results from the two potential models were compared with the phenomenological model giving a better reproduction of the available data. We thus concentrated on improving the SW +SW^3 potential parameters which were further used to investigate the properties of ^{212}Po and ^{218}Rn.

Using optimised potential parameter values we first investigated the ground state band of ^{212}Po by describing the nucleus as an alpha cluster plus a ^{208}Pb core in relative motion characterised by $G = 18$. The experimentally observed level ordering and their characteristic spacing, with the exception of the $0^+ - 2^+$ level splitting, were reproduced satisfactorily, with the inversion of the calculated 16^+ and 18^+ states explaining the isomeric character of the latter. Systematics of the in-band quadrupole transition strengths $B(E2 : J_i \longrightarrow J_f)$ for the ground state band were found to be in good agreement with experiment without any recourse to the use of an effective charge. The good agreement of our theoretical estimates of the ground and excited states half-lives with experiment is a further indication of the consistency of the binary cluster model in describing the properties of ^{212}Po. The branching ratios for the alpha and electromagnetic decays were however poorly reproduced, but it was pointed out that the quoted experimental values are uncertain. We found that for alpha clustering in ^{212}Po (and in ^{44}Ti and ^{20}Ne) the $0^+ - 2^+$ level splitting could be better reproduced by introducing an additional term to modify the short range behaviour of the SW + SW^3 potential.

We next presented calculations leading to two separate negative parity bands in ^{212}Po. The first corresponds to a situation where the core and cluster remain in their ground states with an

odd-G relative motion. The results obtained deviate markedly from the experimental observations. The second negative parity band is obtained by promoting the lead core to its lowest 3^- state which is then coupled to the core-cluster even-G relative motion. The result obtained with the second approach gives rise to a rich spectrum of low-lying negative parity states including a '$K^\pi = 0^-$' with in-band $E2$ transitions of the same order and trend as for the ground state band. We proposed a mixing of the two negative parity bands so as to allow the possibility of cross-band electric dipole transitions.

An important ingredient simplifying the calculations of the properties of the negative parity bands is the similarity of the radial wavefunctions of the core-cluster relative motion. The similarity however decreases with decreasing cluster mass complicating the cluster model analysis of the ^{212}Po negative parity states. The situation in this nucleus is further complicated by the lack of experimental information on these states.

We therefore extended our application of the cluster model in a novel analysis of the properties of ^{218}Rn, described as a ^{208}Pb plus ^{10}Be system. Using an optimised core-cluster potential we obtained a ground state band of the nucleus with properties in good agreement with observations. The underbinding of the 0^+ state and the subsequent correction using a short range interaction suggest the need to further investigate this additional interaction. The order of magnitude of the calculated $E2$ transitions for the ^{218}Rn ground state band lies between those for the positive parity band of ^{212}Po and of Radium isotopes [82]. The negative parity band and the corresponding $E2$ transitions are also well described within the excited core formalism. The inversion of our theoretically predicted $J^\pi = 1^-$ and $J^\pi = 3^-$ states is interesting and can be understood in the weak coupling limit. The splitting of these inverted states has been found to decrease and then reverts to the normal order with increasing cluster mass suggesting a transition from weak to strong coupling as the cluster mass increases.

We have shown that for ^{212}Po the M3Y potential model gives a good account of the ground state alpha decay half-life. It however fails to describe the energy levels of the nucleus giving rise to an inverted spectrum. These observations are consistent with an M3Y potential that is more reliable in the asymptotic region than in the internal region. Its failure to reproduce the experimental energy spectrum has been traced to the too flat a shape in the internal region. This conclusion is reinforced by the improvement brought about for ^{218}Rn by a more rounded M3Y potential. The intimate connection of the M3Y potential model with the core-cluster nuclear densities suggests a need to use density distributions that are more accurate in the nuclear interior. A more realistic treatment of the M3Y potential may also require an improved treatment of the exchange and the density dependent effects. Furthermore a closer examination

of Eqn (2.12) suggests an additional term from the complex, energy and angular momentum dependent non-local term as opposed to the popular restriction to the real M3Y component only.

Alternatively the good features of both potential models could be combined to generate a more reliable phenomenological potential model with an underlying microscopic basis. This could be done by fitting the SW+SW^3 potential to the M3Y potential in the surface region, and then extrapolating the fitted SW+SW^3 form into the internal region.

On a final note the binary cluster model with the SW+SW^3 potential has been found to give a unified description of the alpha decay properties and the energy structure (i.e. yrast states) of ^{212}Po as well as an excellent description of the quasi-harmonic structure of ^{218}Rn.

Appendix A

A1.1: Folding Potential

Supposing the single particle coordinates of the nuclei A and B are represented by $\boldsymbol{q_A} = \boldsymbol{r_1} \cdots \boldsymbol{r_A}$ and $\boldsymbol{q_B} = \boldsymbol{r'_1} \cdots \boldsymbol{r'_B}$ then

$$\begin{aligned}\langle \psi_{A0}\psi_{B0}|\hat{V}|\psi_{A0}\psi_{B0}\rangle &= \iint \langle \psi_{A0}\psi_{B0}|\boldsymbol{q_A q_B}\rangle\langle \boldsymbol{q_A q_B}|\hat{V}|\boldsymbol{q'_A q'_B}\rangle\langle \boldsymbol{q'_A q'_B}|\psi_{A0}\psi_{B0}\rangle d\boldsymbol{q_A} d\boldsymbol{q_B} d\boldsymbol{q'_A} d\boldsymbol{q'_B} \\ &= \iint \psi^*_{A0}(\boldsymbol{q_A})\psi^*_{B0}(\boldsymbol{q_B})\langle \boldsymbol{q_A q_B}|\hat{V}|\boldsymbol{q'_A q'_B}\rangle \\ &\quad \times \psi_{A0}(\boldsymbol{q'_A})\psi_{B0}(\boldsymbol{q'_B}) d\boldsymbol{q_A} d\boldsymbol{q_B} d\boldsymbol{q'_A} d\boldsymbol{q'_B} \end{aligned} \tag{A1}$$

where we have used the completeneness relation [51]

$$\int |\boldsymbol{q_A q_B}\rangle d\boldsymbol{q}_A d\boldsymbol{q}_B \langle \boldsymbol{q_A q_B}| = \mathbf{1}. \tag{A2}$$

The spatial representation of the potential operator $\hat{V}$ is given by

$$\langle \boldsymbol{q_A q_B}|\hat{V}|\boldsymbol{q'_A q'_B}\rangle = V(\boldsymbol{q_A q_B})\delta(\boldsymbol{q_A} - \boldsymbol{q'_A})\delta(\boldsymbol{q_B} - \boldsymbol{q'_B})$$

and hence Eqn (A1) becomes

$$\begin{aligned}\langle \psi_{A0}\psi_{B0}|\hat{V}|\psi_{A0}\psi_{B0}\rangle &= \int \psi^*_{A0}(\boldsymbol{q_A})\psi^*_{B0}(\boldsymbol{q_B})V(\boldsymbol{q_A q_B}) d\boldsymbol{q_A} d\boldsymbol{q_B} \\ &\quad \times \int \delta(\boldsymbol{q_A} - \boldsymbol{q'_A})\delta(\boldsymbol{q_B} - \boldsymbol{q'_B})\psi_{A0}(\boldsymbol{q'_A})\psi_{B0}(\boldsymbol{q'_B}) d\boldsymbol{q'_A} d\boldsymbol{q'_B} \\ &= \int \psi^*_{A0}(\boldsymbol{q_A})\psi^*_{B0}(\boldsymbol{q_B})V(\boldsymbol{q_A q_B})\psi_{A0}(\boldsymbol{q_A})\psi_{B0}(\boldsymbol{q_B}) d\boldsymbol{q_A} d\boldsymbol{q_B} \end{aligned} \tag{A3}$$

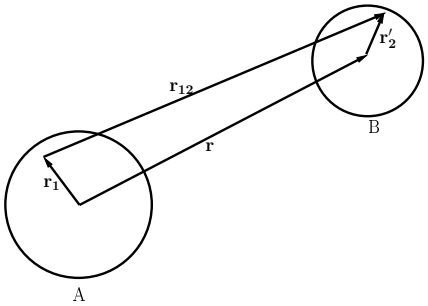

Figure A 1: The folding potential coordinates [53].

where the potential $V(\boldsymbol{q_A q_B}) = \sum_{ij} v(\boldsymbol{r}_{ij})$ may be expressed in terms of one of the possibilities $v(\boldsymbol{r}_{ij})$ as follows

$$\begin{aligned} V(\boldsymbol{q_A q_B}) &= \sum_{i\in A, j\in B} v(\boldsymbol{r}_{ij}) \\ &= ABv(\boldsymbol{r_{12}}). \end{aligned} \tag{A4}$$

The interaction $v(\boldsymbol{r_{12}})$ is then taken to act between the particles $\boldsymbol{r_1}$ in A and $\boldsymbol{r'_2}$ in B.
Define the A-particles wavefunction of the nucleus A by [51];

$$\psi_{A0}(\boldsymbol{q_A}) = \frac{1}{\sqrt{A!}} \begin{vmatrix} \phi_1(\boldsymbol{r_1}) & \phi_1(\boldsymbol{r_2}) & \dots & \phi_1(\boldsymbol{r_A}) \\ \phi_2(\boldsymbol{r_1}) & \phi_2(\boldsymbol{r_2}) & \dots & \phi_2(\boldsymbol{r_A}) \\ \vdots & \vdots & \ddots & \vdots \\ \phi_A(\boldsymbol{r_1}) & \phi_A(\boldsymbol{r_2}) & \dots & \phi_A(\boldsymbol{r_A}) \end{vmatrix} \tag{A5}$$

and for the nucleus B

$$\psi_{B0}(\boldsymbol{q_B}) = \frac{1}{\sqrt{B!}} \begin{vmatrix} \phi_1(\boldsymbol{r'_1}) & \phi_1(\boldsymbol{r'_2}) & \dots & \phi_1(\boldsymbol{r'_B}) \\ \phi_2(\boldsymbol{r'_1}) & \phi_2(\boldsymbol{r'_2}) & \dots & \phi_2(\boldsymbol{r'_B}) \\ \vdots & \vdots & \ddots & \vdots \\ \phi_B(\boldsymbol{r'_1}) & \phi_B(\boldsymbol{r'_2}) & \dots & \phi_B(\boldsymbol{r'_B}) \end{vmatrix} \tag{A6}$$

where $\phi_m(\boldsymbol{r_n})$ represent the single particle wavefunction.

Using Eqns (A4), (A5) and (A6) in Eqn (A3), and integrate over all coordinates except $\boldsymbol{r_1}$ and $\boldsymbol{r'_2}$ gives

$$\begin{aligned}
\langle\psi_{A0}\psi_{B0}|\hat{V}|\psi_{A0}\psi_{B0}\rangle &= \int \psi^*_{A0}(\boldsymbol{q_A})\psi^*_{B0}(\boldsymbol{q_B})V(\boldsymbol{q_A q_B})\psi_{A0}(\boldsymbol{q_A})\psi_{B0}(\boldsymbol{q_B})d\boldsymbol{q_A}d\boldsymbol{q_B} \\
&= \int \frac{(A-1)!}{A!}\sum_i^A |\phi_i(\boldsymbol{r_1})|^2 \frac{(B-1)!}{B!}\sum_j^B |\phi_j(\boldsymbol{r'_2})|^2 AB v(\boldsymbol{r_{12}})d\boldsymbol{r_1}d\boldsymbol{r'_2} \\
&= \int \sum_i^A |\phi_i(\boldsymbol{r_1})|^2 \sum_j^B |\phi_j(\boldsymbol{r'_2})|^2 v(\boldsymbol{r_{12}})d\boldsymbol{r_1}d\boldsymbol{r'_2} \\
&= \int \rho_A(\boldsymbol{r_1})\rho_B(\boldsymbol{r'_2})v(\boldsymbol{r_{12}})d\boldsymbol{r_1}d\boldsymbol{r'_2} \\
&= \int \rho_A(\boldsymbol{r_1})\rho_B(\boldsymbol{r'_2})v(\boldsymbol{r_{12}} = \boldsymbol{r} + \boldsymbol{r'_2} - \boldsymbol{r_1})d\boldsymbol{r_1}d\boldsymbol{r'_2} \qquad \text{(A7)}
\end{aligned}$$

In Eqn (A7) we have defined $\rho_K(\boldsymbol{r_1}) = \sum_i^K |\phi_i(\boldsymbol{r_1})|^2$ for the matter densities of the nuclei $[K = A, B]$, and use the orthonormality property of the single particle states $\phi_m(\boldsymbol{r_n})$ and $\phi_m(\boldsymbol{r'_n})$ with coordinates of Figure (A1).

In the above result the subscripts A and B in Eqn (A7) may be replaced with 1 and 2, and $\boldsymbol{r'_2}$ replaced with $\boldsymbol{r_2}$ without loss of generality. Thus

$$\langle\psi_{A0}\psi_{B0}|\hat{V}|\psi_{A0}\psi_{B0}\rangle = \int \rho_1(\boldsymbol{r_1})\rho_2(\boldsymbol{r_2})v(\boldsymbol{r_{12}} = \boldsymbol{r} + \boldsymbol{r_2} - \boldsymbol{r_1})d\boldsymbol{r_1}d\boldsymbol{r_2} \qquad \text{(A8)}$$

gives the widely used double folding potential.

A1.2: Effective NN Potential Operator

The local NN effective operator is usually taken to be of the form

$$v_{eff}(r) = v_c(r) + v_{LS}(r)\boldsymbol{L}\cdot\boldsymbol{S} + v_T(r)\hat{S}_{12} \qquad \text{(A9)}$$

with

$$\begin{aligned}
v_c(r) &= v_o(r) + v_\sigma(r)\boldsymbol{\sigma_1}\cdot\boldsymbol{\sigma_2} + v_\tau(r)\boldsymbol{\tau_1}\cdot\boldsymbol{\tau_2} + v_{\sigma\tau}(r)(\boldsymbol{\sigma_1}\cdot\boldsymbol{\sigma_2})(\boldsymbol{\tau_1}\cdot\boldsymbol{\tau_2}) \\
v_x(r) &= v_x(r) + v_{x\tau}(r)(\boldsymbol{\tau_1}\cdot\boldsymbol{\tau_2}) \qquad \text{(A10)}
\end{aligned}$$

where x represents either the spin-orbit component LS with orbital angular momentum L and spin angular momentum S, or the tensor component T.

The interaction of Eqn (A9) may also be represented in terms of the projection operators in each NN channel as

$$v_{eff}(r) = v_{SE}P^{SE} + v_{TE}P^{TE} + v_{SO}P^{SO} + v_{TO}P^{TO} \tag{A11}$$

where P^{SE}, P^{TE}, P^{SO} and P^{TO} are the projection operators for the Singlet-Even, Triplet-Even, Singlet-Odd and Triplet-Odd states respectively. The operators are constructed from products of spin (singlet and triplet) and isospin (singlet and triplet) projection operators such that the two-nucleon wavefunction is antisymmetric. The potential strengths of the NN interaction in Eqn (A9) in terms of those in Eqn (A11) are given by [58];

$$\begin{aligned}
v_o(r) &= \frac{1}{16}(3v_{SE} + 3v_{TE} + v_{SO} + 9v_{TO}) \\
v_\sigma(r) &= \frac{1}{16}(-3v_{SE} + v_{TE} - v_{SO} + 3v_{TO}) \\
v_\tau(r) &= \frac{1}{16}(v_{SE} - 3v_{TE} - v_{SO} + 3v_{TO}) \\
v_{\sigma\tau}(r) &= \frac{1}{16}(-v_{SE} - v_{TE} + v_{SO} + v_{TO}) \\
v_x(r) &= \frac{1}{4}(v^x_{TE} + 3v^x_{TO}) \\
v_{x\tau}(r) &= \frac{1}{4}(-v^x_{TE} + v^x_{TO}).
\end{aligned} \tag{A12}$$

We note here that only the term $v_o(r)$ gives the widely used M3Y potential of Eqn (2.22).

A1.3: Bethe-Goldstone Equation (BG)

The BG equation describing the motion of two interacting nucleons in the nuclear medium is simply given by

$$[T_1 + T_2 + Q_{\alpha\beta}(12)v(12)]\psi_{\alpha\beta}(12) = E_{\alpha\beta}\psi_{\alpha\beta} \tag{A13}$$

where

- T_i is the kinetic energy of particle i,
- $Q_{\alpha\beta}(i,j)$ is a nonlocal projection operator,
- $v(i,j)$ is the two particle interaction potential,
- $E_{\alpha\beta}$ is the energy eigenvalue of the occupied states α and β of the two particles.

A1.4: Momentum Space Representation of the Double Folding Potential

Given the M3Y potential

$$V_F(\boldsymbol{r}) = \int \rho_A(\boldsymbol{r_1})\rho_B(\boldsymbol{r'_2})v(\boldsymbol{r_{12}} = \boldsymbol{r} + \boldsymbol{r'_2} - \boldsymbol{r_1})d\boldsymbol{r_1}d\boldsymbol{r'_2} \tag{A14}$$

with corresponding momentum space representation

$$\overline{V_F}(\boldsymbol{q}) = \int d\boldsymbol{r} \exp(i\boldsymbol{q}.\boldsymbol{r})V_F(\boldsymbol{r}). \tag{A15}$$

Using Eqn (A14) in Eqn (A15) gives

$$\begin{aligned}
\overline{V_F}(\boldsymbol{q}) &= \iiint \exp(i\boldsymbol{q}.\boldsymbol{r})\rho_A(\boldsymbol{r_1})\rho_B(\boldsymbol{r'_2})v(\boldsymbol{r_{12}})d\boldsymbol{r}d\boldsymbol{r_1}d\boldsymbol{r'_2} \\
&= \iiint \exp(i\boldsymbol{q}.(\boldsymbol{r_{12}} + \boldsymbol{r_1} - \boldsymbol{r'_2})\rho_A(\boldsymbol{r_1})\rho_B(\boldsymbol{r'_2})v(\boldsymbol{r_{12}})d\boldsymbol{r_{12}}d\boldsymbol{r_1}d\boldsymbol{r'_2} \\
&= \int \exp(i\boldsymbol{q}.\boldsymbol{r_1})\rho_A(\boldsymbol{r_1})d\boldsymbol{r_1} \int \exp(i\boldsymbol{q}. - \boldsymbol{r'_2})\rho_B(\boldsymbol{r'_2})d\boldsymbol{r'_2} \int \exp(i\boldsymbol{q}.\boldsymbol{r_{12}})v(\boldsymbol{r_{12}})d\boldsymbol{r_{12}} \\
&= \overline{\rho_A}(\boldsymbol{q})\overline{\rho_B}(-\boldsymbol{q})\overline{v}(\boldsymbol{q})
\end{aligned} \tag{A16}$$

where $\overline{\rho_A}(\boldsymbol{q})$, $\overline{\rho_B}(-\boldsymbol{q})$ and $\overline{v}(\boldsymbol{q})$ are respectively the momentum space representation of the densities $\rho_A(\boldsymbol{r_1})$, $\rho_B(\boldsymbol{r'_2})$ and the NN interaction $v(\boldsymbol{r_{12}})$.

Taking the inverse transform of Eqn (A15) and using Eqn (A16) gives

$$\begin{aligned}
\overline{V_F}(\boldsymbol{r}) &= (2\pi)^{-3} \int d\boldsymbol{q} \exp(-i\boldsymbol{q}.\boldsymbol{r})\overline{V_F}(\boldsymbol{q}) \\
&= (2\pi)^{-3} \int d\boldsymbol{q} \exp(-i\boldsymbol{q}.\boldsymbol{r})\overline{\rho_A}(\boldsymbol{q})\overline{\rho_B}(-\boldsymbol{q})\overline{v}(\boldsymbol{q})
\end{aligned} \tag{A17}$$

which is numerically easier to compute compare to Eqn (A14).

Appendix B

B1.1: Classical Turning Points and Definite Integrals

The classical turning points r_1, r_2, and r_3 were determined using a combination of the incremental search and bisection methods [94] to obtain the roots of a function $F(r)$ given by

$$F(r) = E_L - V(r) \tag{B1}$$

where the decay energy E_L of a state is the sum of ground state decay energy E_0 and the excitation energy E_x i.e. $(E_L = E_0 + E_x)$.

These methods are based on the simple fact that a root either falls in a given interval (a, b) or equal to one of the boundary values a, b if

$$F(a)F(b) \leqslant 0. \tag{B2}$$

Guided by the nature of the function $F(r)$ we first define the initial region containing the turning points as $r_1 \in [0, 3]$, $r_2 \in [3, 9]$ and $r_3 \in [9, 30]$. The incremental search method is then used to determine the smallest interval containing the root of the function. The exact root within the smallest interval is then obtained with the bisection method to an accuracy of 10^{-5}.
The definite integrals of a function $F(r)$ were calculated with either the extended method

$$\int_a^b F(r)dr = h[F(a + h/2) + F(a + 3h/2) + F(a + 5h/2) + \cdots + F(b + h/2)] \tag{B3}$$

or the Trapezoidal rule

$$\int_a^b F(r)dr = \frac{h}{2}[F(a) + 2F(a + h) + 2F(a + 2h) + 2F(a + 3h) + \cdots + F(b)] \tag{B4}$$

where h is the step size of the order 10^{-3}.

B1.2: Half-life and Energy Spectra

Our computer codes first use the Bohr-sommerfeld (BS) integral to fit the unknown parameters to the experimental data. These parameters are subsequently used to calculate the alpha decay half-life and the energy levels.

Fitting a Single Parameter

The radius R of a phenomenological potential may be fitted to a state L with known decay energy E_L. Starting with an initial value $R = r_o A^{1/3}$ we search through an interval $R \in [c, d]$, depending on the size of the nucleus, to obtain the smallest interval for which the BS quantization integral

$$\int_{r_1}^{r_2} \sqrt{\frac{2\mu}{\hbar^2}\big[E_L - V(r)\big]}\,dr - (G - L + 1)\frac{\pi}{2} = 0 \tag{B5}$$

is satisfied. We next use the bisection method to obtain a final value of R to an accuracy of the order 10^{-3}.

The renormalization parameter λ of a microscopic potential is fitted in a similar manner. Starting with a value of $\lambda = 1$ with an interval of $\lambda \in [0.1, 1]$ in steps of 0.001, the actual λ which satisfies Eqn (B5) is obtained.

The calculation of the energy levels follows the same procedure. Once all the parameters are known, the decay energy E_L is varied until the BS integral is satisfied for each state L.

Multiple Parameter Fitting

The complete parameter search was achieved with nested loops. We construct a loop for each parameter over the intervals $x \in [0.2, 0.4]$, $a \in [0.55, 0.80]$, $V \in [190, 250]$ and $R \in [4, 9]$ respectively. We step through each parameter in this order and calculate the exact difference of both sides of the BS integral in the internal loop over R. For each of the radius R we repeated the internal loop over all the states L using the experimental excitation energy E_x to determine the corresponding energy E_L. The combinations of parameters which gives the least value for the goodness of fit parameter χ^2 (see Eqn 4.8) are taken as the best fit parameter.

B1.3: Schrödinger Wave Equation (SWE)

We use the Bound state diagonalization technique [84] to construct the potential $V(r)$. For a given energy E the second turning point was determined. The SWE was then integrated from the origin to the turning point and from infinity to the same point in steps of h using the Numerov algorithm

$$(1 - F(r+h))\psi(r+h) = (2 + 10F(r))\psi(r) - (1 - F(r-h))\psi(r-h) \tag{B6}$$

where

$$F(r) = \frac{h^2}{12}\frac{2\mu}{\hbar^2}(V(r) - E). \tag{B7}$$

The outward integration from the origin was matched with the inward integration from infinity at the second turning point by varying the energy eigenvalue E until the continuity in both the wavefunction and its first derivative is achieved. The true eigenvalue is signalled when the logarithmic derivatives of both wavefunctions at the turning point are equal and the total number of nodes N is given by

$$N = \frac{G - L^{\pm}}{2} \tag{B8}$$

with $L^{+} = L$ for positive parity state with even L, and $L^{-} = L + 1$ for the odd negative parity state.

Schrödinger Wave Equation (SWE) Vs Bohr-Sommerfeld Quantization Integral (BS)

Tables (B1) and (B2) compare the calculated excitation energies relative to the 0^+ ground state for ^{212}Po and ^{218}Rn using both the numerical solution of the SWE and the approximate BS integral of Eqn (B5). The agreement between the two methods provides a good reason for the parameter search using the BS integral which is computationally more practical.

J^π	E_{SWE}(MeV)	E_{BS}(MeV)
0^+	(0.000)	(0.000)
2^+	0.165	0.164
4^+	0.457	0.453
6^+	0.829	0.823
8^+	1.247	1.235
10^+	1.669	1.650
12^+	2.055	2.024
14^+	2.357	2.310
16^+	2.521	2.446
18^+	2.481	2.346

Table B 1: The energy levels of ^{212}Po calculated with both the SWE and the BS integral using the potential parameters of Eqn (4.10). The energies are given relative to the 0^+ ground states with $E_{SWE}(0) = 0.330$ MeV and $E_{BS}(0) = 0.495$ MeV respectively.

J^π	E_{SWE}(MeV)	E_{BS}(MeV)
0^+	(0.000)	(0.000)
2^+	0.084	0.094
4^+	0.248	0.258
6^+	0.477	0.488
8^+	0.761	0.773
10^+	1.095	1.107
12^+	1.471	1.482
14^+	1.883	1.895
16^+	2.325	2.337
18^+	2.791	2.803
20^+	3.274	3.287
22^+	3.767	3.780
24^+	4.263	4.277
26^+	4.755	4.769

Table B 2: The energy levels of ^{218}Rn calculated with both the SWE and the BS integral using the potential parameters of Eqn (6.2). The energies are given relative to the 0^+ ground states with $E_{SWE}(0) = 0.484$ MeV and $E_{BS}(0) = 0.536$ MeV respectively.

Appendix C

C1.1: Negative Parity K-bands

In an extension of a previous analysis [86] it has been shown [95] that the K-bands arise whenever a particle or an internal excitation, of angular momentum I^π is coupled to a degenerate set of $L^\pi = 0^+, 2^+, 4^+ \cdots$ of core-cluster states having a common radial wavefunction. Figure (C 2) shows the results of a calculation for ^{212}Po obeying these conditions i.e. with the excitation energies $E_L = 0$ and the radial integral $g_{LL'} = g$. For $I^\pi = 3^-$ four bands with $K^\pi = 0^-, 1^-, 2^-$ and 3^- arise each of which consists of degenerate states $J^\pi = 1^-, 3^-, 5^-, 7^-, 9^- \cdots$, $J^\pi = 1^-, 2^-, 3^-, 4^-, 5^-, \cdots$, $J^\pi = 2^-, 3^-, 4^-, 5^-, 6^- \cdots$, $J^\pi = 3^-, 4^-, 5^-, 6^-, 7^-, \cdots$ respectively. Figure (C 3) shows the results when the degeneracy of the core-cluster set of states is lifted for ^{212}Po. A similar characteristic results is found for the ^{218}Rn nucleus as shown in Figure (C 4). The K-band notation is thus only approximate but still useful.

C1.2: The Radial Integral $g_{LL'}$

Listed in Table (C 3) are the explicit values of the radial integral $g_{LL'}$ given by

$$g_{LL'} = \int \psi_L(r) g(r) \psi_{L'}(r) dr \tag{C1}$$

with

$$g(r) = -r \frac{\partial V_N(r)}{\partial r}. \tag{C2}$$

The radial wavefunctions $\psi_L(r)$ and $\psi_{L'}(r)$ of the positive parity ground state band with even angular momenta L and L' have been obtained from numerical solution of the radial Schrödinger Wave Equation using a SW + SW^3 nuclear potential V_N with parameter values of Eqn (4.10) (see section (5.3) for details).

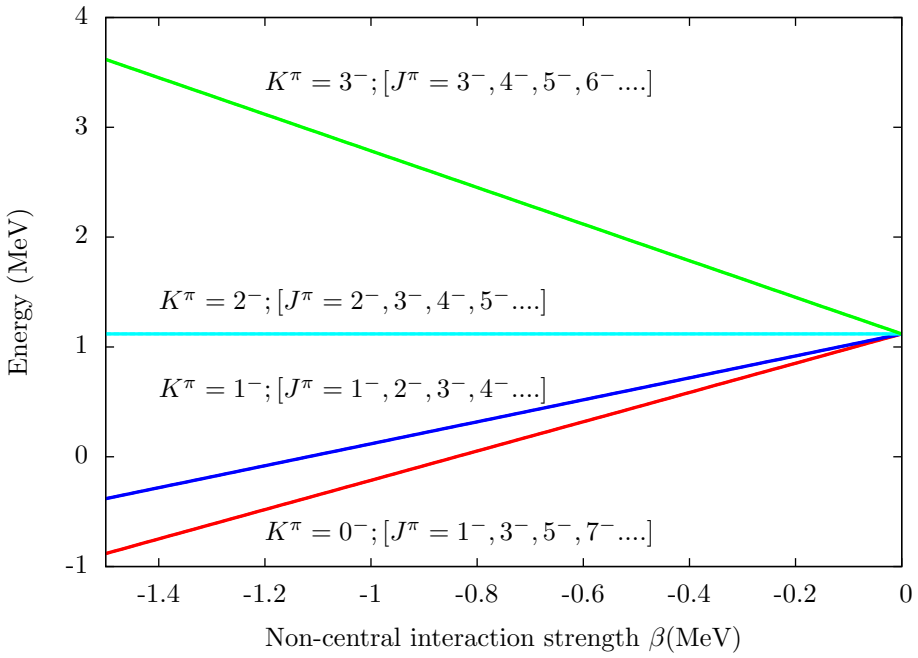

Figure C 2: Results of a core-excitation calculation of the energies of the negative parity states of ^{212}Po assuming degenerate states ($E_L = 0$) for the ^{212}Po ground state band. The excitation energies of the first four J^π states in each of the $K^\pi = 0^-, 1^-, 2^-, 3^-$ bands are plotted as a function of the interaction strength β. The core excitation energy $E(3^-) = 1.12$ MeV. The $K^\pi = 0^-, 1^-, 2^-$ and 3^- bands have further been labelled with colour codes red, blue, cyan and green with increasing excitation energy.

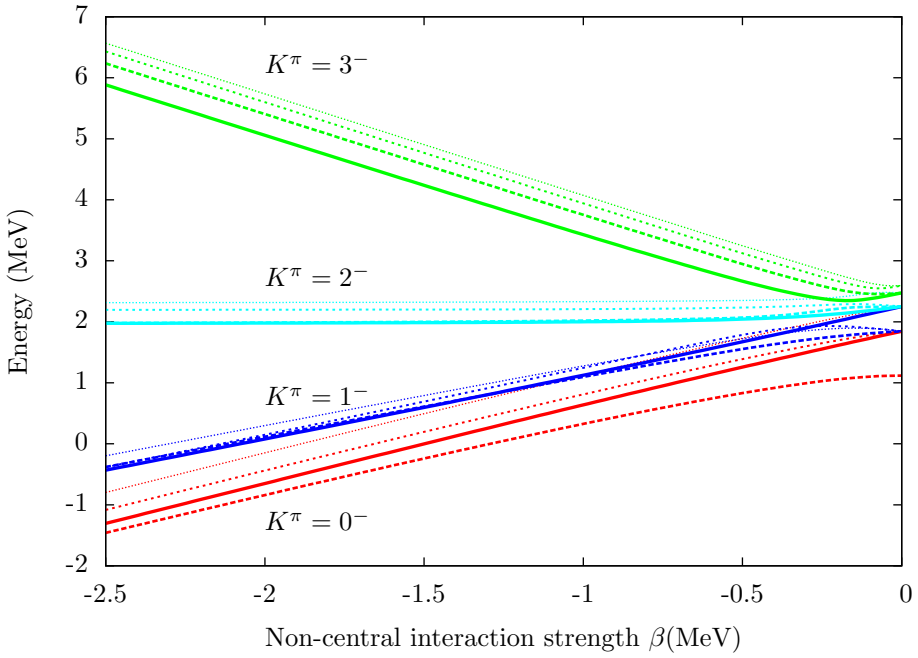

Figure C 3: Results of a core-excitation calculation of the energies of the negative parity states of ^{212}Po using the experimental spectrum for the ^{212}Po ground state band E_L. The excitation energies of the first four J^π states in each of the $K^\pi = 0^-, 1^-, 2^-, 3^-$ bands are plotted as a function of the interaction strength β. The core excitation energy $E(3^-) = 1.12$ MeV. The splitting in each band is denoted with lines (solid, long and short dashes, and dots of different thichness) according to their increasing excitation energies.

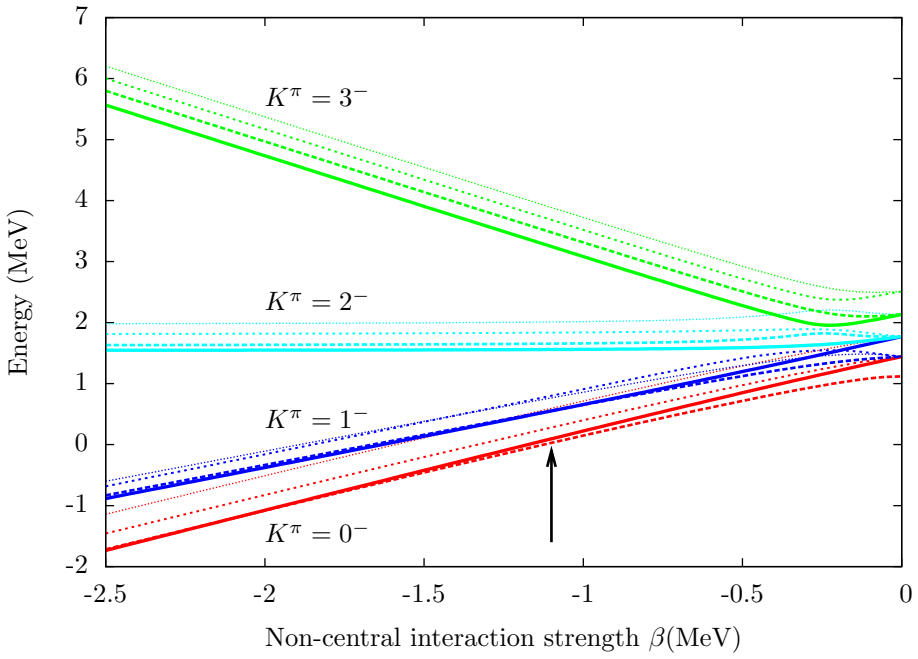

Figure C 4: Results of a core-excitation calculation of the energies of the negative parity states of ^{218}Rn using the experimental spectrum for the ^{218}Rn ground state band E_L. The excitation energies of the first four J^π states in each of the $K^\pi = 0^-, 1^-, 2^-, 3^-$ bands are plotted as a function of the interaction strength β. The core excitation energy $E(3^-) = 1.12$ MeV. The splitting in each band is denoted with lines (solid, long and short dashes, and dots of different thichness) according to their increasing excitation energies. Note the crossing of the lowest $J^\pi = 1^-$ and 3^- states as indicated by the arrow.

L	L'	$g_{LL'}$(MeV)
0	0	-146.1818
0	2	-145.9987
0	4	-142.5427
0	6	-131.0799
2	2	-146.8714
2	4	-144.8921
2	6	-134.7349
2	8	-113.2751
4	4	-148.5098
4	6	-142.8462
4	8	-123.7787
4	10	-92.9551
6	6	-150.9766
6	8	-139.5392
6	10	-110.3121
6	12	-72.3624

L	L'	$g_{LL'}$(MeV)
8	8	-154.0411
8	10	-134.4424
8	12	-94.7964
8	14	-52.9437
10	10	-157.3789
10	12	-126.7939
10	14	-77.4783
10	16	-35.3465
12	12	-160.5877
12	14	-115.4889
12	16	-58.2791
14	14	-163.1963
14	16	-98.7463
16	16	-164.6691

Table C 3: The radial integrals involving the ground state band wavefunctions of ^{212}Po. The functional form $g(r)$ has been calculated using the SW+SW^3 potential parameter of Eqn (4.10).

Bibliography

[1] B. A. Brown and B. H. Wildenthal, At. Data Nucl. Data Tables **33**, 347 (1985).

[2] M. A. Preston and R. K. Bhaduri, *Structure of the Nucleus*, (Addison-Wesley, 1975).

[3] A. Arima, H. Horiuchi, K. Kubodera and N. Takigawa, *Advances in Nuclear Physics*, Eds. M. Baranger and E. Vogt, Vol. **5**, (Plenum, New York 1972), pg. 345.

[4] B. Buck, A. C. Merchant and S. M. Perez, J. Phys. G: Nucl. Part. Phys. **17**, 1223 (1991).

[5] R. K. Sheline and K. Wildermuth, Nucl. Phys. **21**, 196 (1960).

[6] B. Buck, C. B. Dover and J. P. Vary, Phys. Rev. **C11**, (5), 1803 (1975).

[7] M. Freer and A. C. Merchant, J. Phys. G: Nucl. Part. Phys. **23**, 261 (1997).

[8] A. de Shalit and H. Feshbach, *Theoretical Nuclear Physics Volume 1: Nuclear structure*, (John Wiley and Sons, 1990).

[9] S. M. Wong, Introductory Nuclear Physics, (Prentice Hall International, 1990).

[10] R. D. Lawson, *Theory of the Nuclear Shell Model*, (Oxford Univ. Press, N. Y. 1980), pg 5-6.

[11] P. V. Isacker, C. R. Physique **(**4), 529 (2003).

[12] B. Buck, A. C. Merchant and S. M. Perez, Phys. Rev. **C51**, (2), 559 (1995).

[13] K. Wildermuth and Y. C. Tang, *A Unified Theory of the Nucleus*, (New York: Acad. 1977).

[14] H. Horiuchi and K. Ikeda, *Cluster Model of the Nucleus*, Int. Rev of Nucl. Phys. Eds. T. T. S. Kuo and E. Osnes, Vol. **4**, (World Scientific, Singapore, 1986) pg 1-258.

[15] B. Buck, A. C. Merchant and S. M. Perez, J. Phys. G: Nucl. Part. Phys. **18**, 143 (1992).

[16] Y. C. Tang, K. Wildermuth and L. D. Pearlstein, Phys. Rev. **123**, (2), 548 (1961).

[17] H. J. Mang, Ann. Rev. Nucl. Sci. **14**, 1 (1964).

[18] R. G. Thomas, Prog. Theor. Phys. **12**, 253 (1954).

[19] F. A. Janouch and R. J. Liotta, Phys. Rev. **C27**, (2) 896 (1983).

[20] O. G. Ogunbade, MSc Thesis, University of South Africa, (Unpublished) (2005).

[21] K. Varga, R. G. Lovas and R. J. Liotta, Phys. Rev. Lett. **69**, (1) 37 (1992).

[22] R. G. Lovas, R. J. Liotta, A. Insolia, K. Varga and D. S. Delion, Phys. Rep. **294**, 265 (1998).

[23] F. Hoyler, P. Mohr and G. Staudt, Phys. Rev. **C50**, (5) 2631 (1994).

[24] H. P. Zhang and G. Royer, Phys. Rev. **C77**, 054318 (2008).

[25] D. S. Delion, A. Insolia and R. J. Liotta, Nucl. Phys. **A654** 673c (1999).

[26] B. Buck, A. C. Merchant and S. M. Perez, Phys. Rev. **C45**, (5) 2247 (1992).

[27] R. Blendowske and H. Walliser, Phys. Rev. Lett. **61**, (17) 1930 (1988).

[28] K. Wildermuth and Th. Kanellopoulos, Nucl. Phys. **7**, 150 (1958).

[29] B. Buck, A. C. Merchant and S. M. Perez, Phys. Rev. Lett. **65**, (24) 2975 (1990).

[30] B. Buck, A. C. Merchant, Phys. Rev. **C39**, (5) 2097 (1989).

[31] B. Buck, A. C. Merchant, S. M. Perez, Phy. Rev. **C49**, (6) 3357 (1994).

[32] C. Xu and Z. Ren, Nucl. Phys. ***A*753**, 174 (2005); Nucl. Phys. **A760**, 303 (2005).

[33] D. N. Basu, J. Phys. G: Nucl. Part. Phys. **29**, 2079 (2003); Phys. Lett. **B566** 90 (2003).

[34] S. Ohkubo, Phys. Rev. Lett. **74**, (12) 2176 (1995).

[35] P. E. Hodgson and E. Běták, Phys. Rep. **374**, 1 (2003).

[36] H. J. Rose and G. A. Jones, Nature **307**, 245 (1985).

[37] B. Buck, A. C. Merchant, S. M. Perez, Phys. Rev. **C58**, (4) 2049 (1998); Phys. Rev. Lett. **76**, (3) 380 (1996); Nucl. Phys. **A512**, 483 (1990).

[38] W. Greiner, M. Ivascu, D. N. Poenaru and A. Sandulescu, Z. Physik ***A*320**, 347 (1985).

[39] B. Buck, P. D. B. Hopkins and A. C. Merchant, Nucl. Phys. **A513**, 75 (1990).

[40] B. Buck, A. C. Merchant and S. M. Perez, J. Phys. G: Nucl. Part. Phys. **30**, 65 (2004); Phys. Rev. **C68**, 024313 (2003).

[41] B. Buck, A. C. Merchant, M. J. Horner and S. M. Perez, Nucl. Phys. **A673** 157 (2000).

[42] H. Horiuchi, Eur. Phys. J. **A13**, 39 (2002).

[43] B. Buck, A. C. Merchant, S. M. Perez, Phys. Rev. **C77**, 017301 (2008); Phys. Rev. Lett. **94**, 202501 (2005).

[44] B. Buck, A. C. Merchant and S. M. Perez, J. Phys. G: Nucl. Part. Phys. **34**, 1985 (2007).

[45] A. Silisteanu, W. Scheid, A. Sandulescu, Nucl. Phys. **A679**, 317 (2001).

[46] M. Tomaselli, T. kuhl, D. Ursescu, Prog. Part. and Nucl. Phys. **59**, 455 (2007).

[47] Y. Kanada-En'yo, Phys. Rev. **C66**, 011303(R) (2002).

[48] P. Descouvemont, Nucl. Phys. **A709**, 275 (2002).

[49] B. Buck, J. C. Johnston, A. C. Merchant and S. M. Perez, Phys. Rev. **C52**, (4) 1840 (1995).

[50] J. P. Vary and C. B. Dover, Phys. Rev. Lett. **31**, (25) 1510 (1973).

[51] R. H. Landau, *Qantum Mechanics II: A Second Course in Quantum Theory*, (John Wiley and Sons, 1990).

[52] T. T. S. Kuo, G. E. Brown, Nucl. Phys. **85**, 40 (1966).

[53] G. R. Satchler and W. G. Love, Phys. Rep. **55**, (3) 183 (1979).

[54] N. K. Glendenning, *Direct nuclear reactions*, (World Scientific Pub. Co. Pte. Ltd. 2004).

[55] P. E. Hodgson, *Lecture Notes in Physics* **55***: Nuclear Optical Model Potential*, Eds. S. Boffi and G. Passatore (Springer Verlag, 1976).

[56] H. de Vries, C. W. de Jager and C. de Vries, At. data and Nucl. data tables **36**, 495 (1987).

[57] S. Karataglidis, K. Amos, B. A. Brown and P. K. Deb, Phys. Rev. **C65**, 044306 (2002).

[58] W. G. Love, Conf. Proc. *The (p,n) reaction and the Nucleon-Nucleon force*, Telluride, Colorado (Plenum Press, N. Y. 1980).

[59] G. L. Thomas, B. C. Sinha, F. Duggan, Nucl. Phys. **A203**, 305 (1973).

[60] G. Bertsch, J. Borysowicz, H. McManus and W. G. Love, Nucl. Phys. **A284**, 399 (1977).

[61] B. Buck and A. A. Pilt, Nucl. Phys. **A280**, 133 (1977).

[62] H. E. Seal. MSc Thesis, University of Cape Town, (Unpublished) (2006).

[63] A. S. B. Tariq et al, Phys. Rev. **C59**, (5) 2558 (1999).

[64] F. Michel, G. Reidemeister and Y. Kondo, Phys. Rev. **C51**, (6) 3290 (1995).

[65] A. C. Merchant, Phys. Rev. **C36** (2) 778 (1987).

[66] B. Buck, A. C. Merchant and S. M. Perez, At. data and Nucl. data tables **54**, (1) 54 (1993).

[67] B. Buck, J. C. Johnston, A. C. Merchant and S. M. Perez, Phys. Rev. **C53**, (6) 2841 (1996).

[68] N. Zettili, *Quantum Mechanics: Concepts and Applications* (John Wiley and Sons, 2001).

[69] K. Gottfried and T. Yan, *Quantum Mechanics: Fundamentals* (Springer, New York, 2004).

[70] S. A. Gurvitz and G. Kalbermann. Phys. Rev. Lett. **59**, 262 (1987).

[71] K. N. Mukhin, *Experimental Nuclear Physics:Volume 1*, (Mir Publisher, Moscow 1987).

[72] J. M. Blatt and V. F. Weisskopf, *Theoretical Nuclear Physics*, (John Wiley and Sons, 1952).

[73] B. Buck, A. C. Merchant, M. J. Horner and S. M. Perez, Phys. Rev. **C61**, 024314 (2000).

[74] D. M. Brink and G. R. Satchler, *Angular Momentum*, (Oxford Univ. Press, N. Y. 1993).

[75] J. Cook, Computer Physics Communications **25**, 125 (1982).

[76] A. B. Garnsworthy et al, J. Phys. G: Nucl. Part. Phys. **31**, S1851 (2005).

[77] B. Buck, A. C. Merchant and S. M. Perez, Phys. Rev. Lett. **72**, (9) 1326 (1994).

[78] Nuclear Structure Data [online],http://www.nndc.bnl.gov/nudat2/; T. Kibédi et al. Nucl. Inst. and Method, **A589**, 202 (2008); http://www.rsphysse.anu.edu.au/nuclear/bricc.

[79] H. Abele and G. Staudt, Phys. Rev. **C47**, (2) 742 (1993).

[80] J. F. C. Cocks et al., Nucl. Phys. **A645**, 61 (1999).

[81] P. A. Butler and W. Nazarewicz, Rev. of Mod. Phys. **68**, (2) 1996.

[82] B. Buck, A. C. Merchant and S. M. Perez, Nucl. Phys. **A617**, 195 (1997).

[83] D. Ward et al., Nucl. Phys. **A600**, 88 (1996).

[84] R. A. Baldock, B. Buck and J. A. Rubio, Nucl. Phys. **A426**, 222 (1984).

[85] B. Buck, A. C. Merchant and S. M. Perez, J. Phys. G: Nucl. Part. Phys. **35**, 085101 (2008); J. Phys: Conference. Series **111**, 012041 (2008).

[86] D. M. Brink, B. Buck, R. Huby, M. A. Nagarajan and N. Rowley, J. Phys. G: Nucl. Phys. **13**, 629 (1987).

[87] B. Buck, A. C. Merchant, S. M. Perez, T. T. Ibrahim, S. M. Wyngaardt, J. Phys. G: Nucl. Part. Phys. **36**, 085101 (2009).

[88] J. J. Sakurai, *Modern Quantum Mechanics*, (Addison-Wesley, 1985).

[89] G. A. Leander, W. Nazarewicz, G. F. Bertsch and J. Dudek, Nucl. Phys. **A453**, 58 (1986).

[90] B. Buck, A. C. Merchant and S. M. Perez, Nucl. Phys. **A625**, 554 (1997).

[91] B. Buck, A. C. Merchant, S. M. Perez and H. E. Seals, J. Phys. G: Nucl. Part. Phys. **31**, 1499 (2005).

[92] G. Fricke et al., At. data and Nucl. data tables **60**, 177 (1995).

[93] Nuclear Structure Data [online], http://www.nndc.bnl.gov/nudat2.

[94] D. M. Etter, *Structured Fortran 77 for Engineers and Scientists*, (Addison-Wesley, 1997).

[95] B. Buck, A. C. Merchant and S. M. Perez (in preparation).